
Charge Storage Behavior of β -FeSi₂ Nanoparticles

Von der Fakultät für Ingenieurwissenschaften,

Abteilung Maschinenbau und Verfahrenstechnik

der

Universität Duisburg-Essen

zur Erlangung des akademischen Grades

einer

Doktorin der Ingenieurwissenschaften

Dr.-Ing.

genehmigte Dissertation

von

Fangfei Li

aus

Liaoning, V. R. China

Tag der mündlichen Prüfung: 13.07.2021

Gutachter: apl. Prof. Dr. rer. nat. Hartmut Wiggers

Prof. Dr. rer. nat. Axel Lorke



Conference Contribution:

Year	Conference	Poster
2017	DPG (Deutsche Physikalische Gesellschaft)	Charge storage in β -FeSi ₂ nanoparticles
2017	MiFuN (Microstructural Functionality at the Nanoscale)	Charge storage in β -FeSi ₂ nanoparticles
2018	DPG (Deutsche Physikalische Gesellschaft)	Charge storage in β -FeSi ₂ nanoparticles
2018	MCIC (The second Materials Chain International Conference)	Clean Energy Storage in Microcapacitor with β -FeSi ₂ Nanoparticles.

The International Max Planck Research School for Interface Controlled Materials for Energy Conversion (IMPRS-SurMat) Course:

T1 course	Basic concepts in materials science
T2 course	Physical chemistry of surfaces and interfaces
T3 course	Multiscale modelling
T4 course	Structure of solids



CONTENT

ABBREVIATIONS	VII
SYMBOLS.....	VIII
ZUSAMMENFASSUNG	XI
ABSTRACT	XII
1 Background and Motivation	1
2 Introduction	3
3 Fundamentals and Techniques	5
3.1 Introduction of the capacitors	5
3.1.1 Faradaic process and non-Faradaic process	9
3.1.2 The configurations of electrochemical capacitors	9
3.1.3 Popular research directions.....	10
3.2 Techniques of assembling the interdigitated capacitor	11
3.2.1 Photolithography	11
3.2.2 Evaporating.....	14
3.2.3 Bonding	14
3.3 Materials characterization techniques	15
3.3.1 Scanning electron microscopy	15
3.3.2 Focused ion beam	16
3.3.3 X-ray diffraction	17
3.3.4 X-ray photoelectron spectroscopy	17
3.3.5 Brunauer–Emmett–Teller	18
3.4 Electric measurement.....	19
3.4.1 Potentiostatic and galvanostatic test.....	19
3.4.2 Cyclic voltammetry	21
3.4.3 Linear sweep voltammetry.....	22
3.5 Charge transfer mechanism.....	22
4 β-FeSi₂ Synthesis	25
4.1 Basic information of β -FeSi ₂	25
4.2 Synthesis setup and mechanism.....	25
5 Capacitor Assembly and Electrical Measurement Equipment.....	29
5.1 Interdigitated structure capacitor.....	29
5.2 Double-plate capacitor	31
5.3 The equipment of electrical measurement	32
6 Result and Discussion	35

6.1	Characterization of β -FeSi ₂	35
6.1.1	Scanning electron microscope.....	35
6.1.2	X-ray diffraction	37
6.1.3	X-ray photoelectron spectroscopy	38
6.1.4	Brunauer-Emmett-Teller test.....	40
6.2	Preliminary analysis of the electrical performance on the interdigitated capacitor	41
6.2.1	Mass control of the β -FeSi ₂	41
6.2.2	Cyclic voltammetry	44
6.2.3	Potentiostatic measurement	44
6.2.4	Galvanostatic measurement.....	48
6.3	Mechanism discussion.....	50
6.3.1	Charge transfer behavior	50
6.3.2	The establishment of a working model	54
6.3.3	Oxygen sensing measurement	58
6.4	Parallel plate capacitor with different materials.....	61
6.4.1	Parallel plate capacitor with β -FeSi ₂ nanoparticles	62
6.4.2	Parallel plate capacitor with SiO ₂ nanoparticles.....	64
6.4.3	Parallel plate capacitor with B-doped silicon	65
6.5	Mass-dependent stored charge.....	67
6.6	Additive polyacrylic acid	68
7	Summary.....	71
8	Further work and outlook.....	73
9	Reference.....	75
10	List of graphs.....	85
11	Appendix	91
11.1	Oxygen evolution and hydrogen evolution test.....	91
11.2	X-ray photoelectron spectroscopy (XPS)	93
11.3	Oxygen sensing measurement of B-Si nanoparticles.....	95
12	Acknowledgment	97

ABBREVIATIONS

XRD	X-ray diffraction
BET	Brunauer-Emmett-Teller
XPS	X-ray photoelectron spectroscopy
FIB	Focused ion beam
SEM	Scanning electron microscopy
CV	Cyclic voltammetry
HER	Hydrogen evolution reaction
OER	Oxygen evolution reaction
LSV	Linear sweep voltammetry
RDE	Rotating disk electrode
MS	Mass spectrometry
NAP-XPS	Near ambient pressure X-ray photoelectron spectroscopy

SYMBOLS

ϵ_0	Vacuum permittivity
ϵ_r	Relative static permittivity
C	Capacitance
A	Area of the electrode
d	Distance between two plate electrodes
C_H	Helmholtz layer's capacitance
C_d	Diffusion layer's capacitance
E_q	Electrochemical equivalent
I	Current
t	Time
Q	Charge
m	mass
F	Faraday constant
M	Molar mass of the reacted chemicals
n	The number of ions
λ	The wavelength of the incident waves
θ	The angle formed by the incident waves and the crystal plane
d	The distance of the two parallel crystal planes
$E_{binding}$	Binding energy
E_{photon}	The energy of X-ray photon
ϕ	XPS instrument's work function
p	Partial pressure of the inert gas
p_0	The saturated pressure of the inert gas at the liquid nitrogen temperature
C	BET constant describing the interaction condition between the adsorbent and the adsorbate
N_A	Avogadro number
S	Specific surface area
V_{mol}	The molar volume of the adsorbate gas
V_m	The monolayer adsorption volume

R	Resistance
C	Capacitance
τ	Time constant
J	Current density
V	Voltage
N	Total number of calculated nanoparticles
x_i	the size for a single particle
σ_g	The geometric standard deviation
CMD	The count median diameter.
β	The full-width, half-maximum of the intensity(FWHM)
θ	The Bragg angle
κ	The shape factor
λ	The wavelength of X-ray



ZUSAMMENFASSUNG

Energieknappheit ist seit Jahrzehnten ein viel diskutiertes Thema. Die Entwicklung neuer Industrien und die zunehmende Sorge um Umweltverschmutzungen erfordern nicht nur eine hohe Energiedichte, sondern auch saubere Energiequellen. Unter allen Energiequellen haben sich erneuerbare, saubere Energien in den letzten Jahren dramatisch entwickelt aber sie erfordern Energiespeicher wie Batterien und Superkondensatoren. Ihre Nutzung im schnell wachsenden Markt tragbarer elektronischer Geräte und elektrischer Fahrzeuge bietet eine vielversprechende Lösung für die Nutzung erneuerbarer Energie.

Normalerweise arbeiten elektrochemische Energiespeicher wie Batterien und Superkondensatoren mit einem flüssigen Elektrolyten, entweder organisch oder anorganisch, der normalerweise giftig und umweltschädlich ist. Wir präsentieren jedoch einen ungiftigen, umweltfreundlichen und kostengünstigen Kondensator auf Basis von β -FeSi₂ Nanopartikeln, der in gesättigtem Wasserdampf arbeitet. Im Gegensatz zu herkömmlichen parallelen Doppelplattenkondensatoren wird eine innovative interdigitalisierte Kondensatorstruktur verwendet. Das Gerät ist elektrisch robust und kann auch nach Anlegen einer Hochspannung mehrfach wiederverwendet werden. Die β -FeSi₂ Nanopartikel des aktiven Materials werden auf die goldinterdigitalisierte Struktur aufgeschleudert, die mittels Lithographie auf ein SiO₂ Substrat (4 × 4 mm²) gedruckt wird. Die Interdigital-Struktur wird verwendet, um – verglichen mit herkömmlichen Doppelplattenkondensatoren – Wasserdampf einen leichteren Zugang zu den β -FeSi₂ Nanopartikeln zu ermöglichen. Das Aktivmaterial β -FeSi₂ Nanopartikel wird durch direkte Gasphasensynthese hergestellt und ermöglicht eine Massenproduktion zu einem niedrigen Preis.

Der mit β -FeSi₂ Nanopartikeln beschichtete interdigitalisierte Kondensator, der unter gesättigtem Wasserdampf getestet wurde, zeigt eine spezifische Kapazität, die drei Größenordnungen höher ist als die Kapazität des unter trockener Luft getesteten interdigitalen β -FeSi₂ Kondensators. Auch der Interdigital-Kondensator ohne β -FeSi₂ Dünnschicht weist im Vergleich zum mit Nanopartikeln beschichteten Kondensator vernachlässigbare Kapazität auf. In dieser Arbeit wird die Wirkung von Wasserdampf und β -FeSi₂ Nanopartikeln während des Lade- und Entladevorgangs untersucht sowie der Lade- und Entlademechanismus einschließlich des Ladungsübertragungsverhaltens von halbleitenden Materialien unter Wasserdampfatmosphäre. Ein Arbeitsmodell des interdigitalen β -FeSi₂ Kondensators wird erstellt. Darüber hinaus wird die Speicherkapazität des Interdigital-Kondensators unter unterschiedlichen Arbeitsatmosphären und mit weiteren Aktivmaterialien untersucht, getestet und verglichen.

ABSTRACT

Energy shortage has always been a hot topic for decades. New industries' development and more significant concern over environmental pollutions require high energy density and clean energy resources. Among all the energy sources, renewable clean energies have developed dramatically in recent years, however, they require storage systems such as batteries and supercapacitors. Their utilization along with the fast-growing market of portable electronic devices and electric vehicles provide a promising solution for the utilization of renewable energies.

Usually, electrochemical energy storage devices such as batteries and supercapacitors work with liquid electrolyte, either organic or inorganic, which is usually toxic and harmful to the environment. However, we present a non-toxic, environmentally friendly, and cost-effective capacitor based on β -FeSi₂ nanoparticles that works in air saturated water vapor. Unlike traditional parallel double plate capacitors, an innovative interdigitated capacitor structure is employed. The device is electrically robust, can be reused many times, even after applying high voltage. The active material β -FeSi₂ nanoparticles are spin-coated onto the gold interdigitated structure printed on the SiO₂ substrate (4×4 mm²) using lithography. The interdigitated structure enables easier access for water molecules to the β -FeSi₂ nanoparticles, compared to conventional double plate capacitors. The active material β -FeSi₂ nanoparticles are produced via direct gas-phase synthesis and enable mass production at a low price.

The β -FeSi₂ nanoparticles-coated interdigitated capacitor tested in the air saturated water vapor shows a specific capacitance, which is three orders of magnitude higher than the capacitance of the β -FeSi₂ interdigitated capacitor tested under dry air. The interdigitated capacitor without β -FeSi₂ thin film exhibits a negligible capacitance, compared to the interdigitated capacitor with nanoparticles. In this work, the effect of water vapor and β -FeSi₂ nanoparticles during the charging and discharging process is studied as well as the charging and discharging mechanism, including the charge transfer behavior of semiconducting materials in the air saturated with water vapor. A working model of the β -FeSi₂ interdigitated capacitor is established. Besides, the storage capacity of interdigitated capacitors under different working atmospheres and with additional active materials, are also investigated, tested and compared.

1 Background and Motivation

Traditional energy resources, petroleum, and coal produce numerous carbon dioxide, nitrogen oxides, and sulfur oxides[1]. Such atmospheric pollutants trigger serious issues such as acid rain and extreme weather, leading to frequent heat waves, storms, and droughts. It causes a large number of deaths and property losses every year, due to the reasons above. Hence, a clean energy resource with low atmospheric pollutant emission is investigated to replace the traditional energy source in the past years.

Electrochemical energy storage (supercapacitors and batteries) has become a promising option under such a situation. The mechanism of electrochemical energy storage is to convert electrochemical energy to electric energy through electrochemical reactions. Usually, there is no polluting gas produced during the reaction, making electrochemical energy storage more environmentally friendly than coal and petroleum. Lithium-ion batteries[2], sodium-ion batteries[3], and flexible asymmetric supercapacitor[4] are hot research topics in recent years.

It must be noticed that the explosive development of electrochemical energy storage is driven by the prosperity of the electric vehicle (EV) market. Electric vehicles have no gas emissions (no air pollutions), higher energy efficiency, simpler construction (no internal combustion engine, transmission, fuel tank, and exhaust system), and lower noise than conventional cars. The electric luxury car Tesla Model S appeared first time in the market in 2009 and set off a wave of automobile development worldwide. The worldwide electric car sales reached 2.3 million in 2020, with an explosive growth speed (Figure 1.1). The Y-axis on the left represents the sales on a million scale.

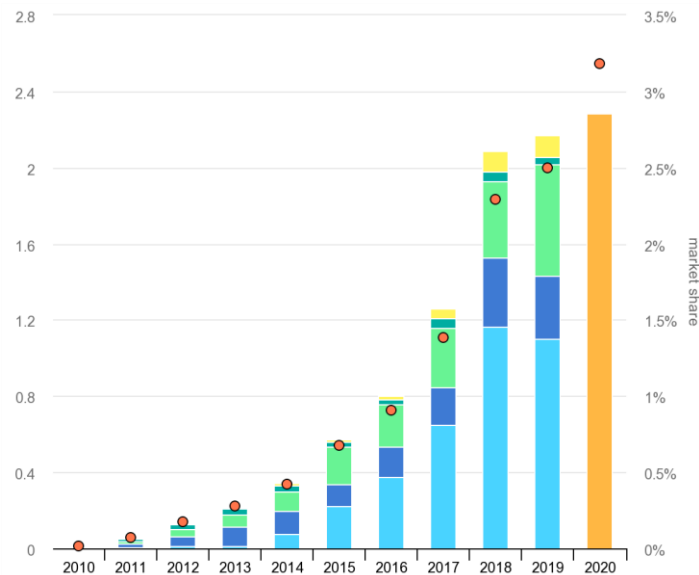


Figure 1.1 Global electric car sales by key markets, 2010-2020. (IEA analysis based on IEA data and EV-Volumes (2020)). The light blue color represents the sales in China, and purple represents the USA, green represents Europe, yellow represents Japan, and the orange color represents the worldwide sales[5]

Another noticeable trend is the popularity of portable electronic products, e.g., smartphones, laptops, and other electronic devices. With the variety of electrical and electronic products, the demand for various electrochemical energy storage methods is greater. In another sentence, energy storage methods with high energy density (large capacity, Wh/kg, Wh/m³) and high power density (high charging and discharging rate, W/kg, W/m³) are both required.

Electrochemical energy storage, i.e., battery and electrochemical capacitor, can fulfill the demands mentioned above and developed rapidly in recent years. A battery is composed of two electrodes (cathode and anode), a separator, and a liquid/solid electrolyte in between. It is a device that converts the chemical reaction energy via chemical reactions taking place in electrolyte/cathode interface and electrolyte/anode interface to electrical energy during the discharging process, and vice versa for the charging process[6]. Batteries usually have high energy density (Wh/kg or Wh/m³), i.e., high energy storage capacity.

Capacitors, particularly supercapacitors, can provide instantaneous power due to their high power density (W/kg, W/m³), i.e., high energy storage speed. Supercapacitors can work as a good supplement in engines or any nonstop power systems. The supercapacitor can store charge via either a redox reaction (oxidation reaction and a reduction reaction) or the polarization of positive ions and negative ions, which will be introduced in detail in section 3.1.

An environmentally friendly capacitor with a β -FeSi₂ thin film on an unconventional interdigitated microstructure is fabricated and studied in this work. The nanomaterial β -FeSi₂ is a semiconducting material that is used in solar cells[7, 8], optoelectronic and photonic[9, 10], and thermoelectric devices[11-13], but seldom used as active material in the energy storage system. The previous study[14] by Theis et al. indicates that β -FeSi₂ can be used in the storage charging system, displaying a potential of charge storage. This work is a continuation of Theis's previous work, and an environmentally friendly, micro-sized, open-type, interdigitated capacitor with β -FeSi₂ thin-film working in the air saturated with water vapor is measured, and the mechanism behind the charging and discharging process is studied.

The employment of water vapor as an electrolyte is another innovative point of this work, which differs from other conventional electrochemical capacitors that work with either liquid/solid electrolyte or organic/inorganic electrolyte. The open-type structure enables the water vapor in the air to reach the β -FeSi₂ capacitor, broadens its applications under different occasions, such as in an island or the outdoor environment in the highly humid tropical areas, or even in the pipeline where the clean water vapor is discharged from the cooling tower of a thermal power station.

2 Introduction

An environmentally friendly capacitor on an unconventional interdigitated microstructure is fabricated in this work, with a β -FeSi₂ as the active material. And its charging and discharging mechanism is studied.

In Chapter 3, the equipment needed for nanoparticle synthesis, nanoparticles characterization (Scanning Electron Microscope, X-ray diffraction, Brunauer-Emmett-Teller test, X-ray photoelectron spectroscopy, etc.), capacitor assembly (lithography mechanism and the needed equipment), and the types of electrical measurement are introduced.

The detailed introduction of the β -FeSi₂ nanoparticles, the mechanism of synthesizing β -FeSi₂ nanoparticles with the gas-phase synthesis method, and the synthesis set-up (hot-wall reactor) is introduced in Chapter 4. The parameters during the synthesis, i.e., the tube temperature, the pressure inside the reaction tube, the precursors' mass flow, is set to produce pure phase β -FeSi₂ nanoparticles.

The fabrication method of the interdigitated capacitor with lithography and the double-plate capacitor is introduced in Chapter 5 to compare the pros and cons of these two different capacitor configurations in the latter experiments. Besides, the self-assembly electrical measurement setup is presented.

Also, to understand the charge storage mechanism, the detailed physical and chemical properties of β -FeSi₂ are highly demanded. The characterization result of the as-synthesized materials β -FeSi₂ is shown in Section 6.1. Preliminary Analysis of the interdigitated capacitor's electrical measurement with β -FeSi₂, including potentiostatic measurement, galvanostatic measurement, and cyclic voltammetry measurement, are introduced in Section 6.2. The contribution of water and β -FeSi₂ nanoparticles to the stored charge is preliminarily figured out.

The mechanism of charge storage is studied in Section 6.3, based on the result of Section 6.2. The charge transfer behavior of the interdigitated capacitor with semiconducting β -FeSi₂ NPs is studied. By comparing the charge transfer behavior under dry/humid atmosphere separately, water molecules' influence on the charge transfer behavior is figuring out. A simplified schematic model with two adjacent nanoparticles is presented to understand the charging/discharging mechanism. The role water molecules play in the charging/discharging process is figured out. Besides, an equivalent circuit model has been developed.

Section 6.4 is about the electrical measurement with parallel plate capacitor with β -FeSi₂ nanoparticles. The influence of different capacitor configurations on electrical performance is compared and discussed. Also, the electrical performance of other materials, such as SiO₂ nanoparticles, is tested, eliminating the charge contribution of the SiO₂ shell on the surface of β -FeSi₂ nanoparticles.



3 Fundamentals and Techniques

3.1 Introduction of the capacitors

There are three types of capacitors, including the electrostatic capacitor, the electrolytic capacitor, and the electrochemical capacitor in Figure 3.1[15, 16]. The electrostatic capacitor is symmetric, employing metals as electrodes. The common dielectric materials are ceramics[17], polymer[18], and even papers[19].

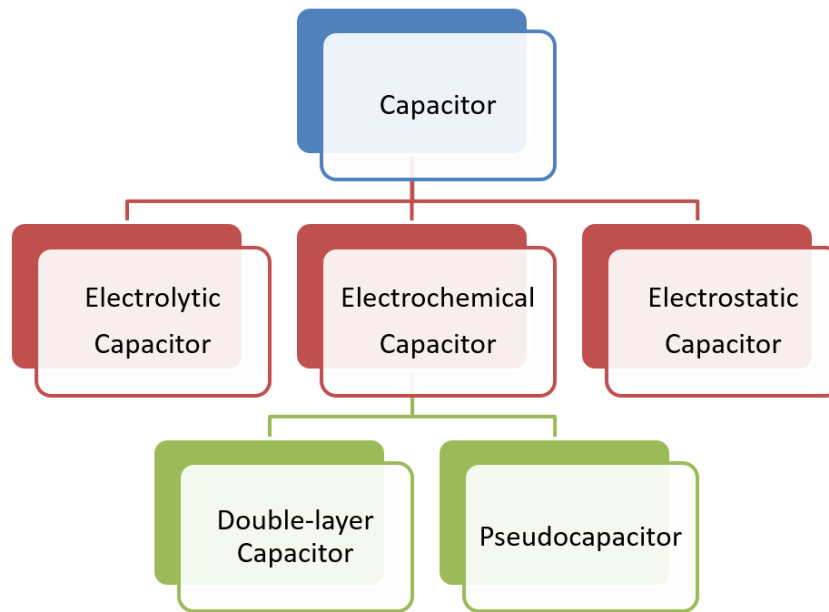


Figure 3.1 There are three types of capacitors, including the electrolytic, electrochemical, and electrostatic capacitors. The electrochemical capacitors have two categories, double-layer capacitor and pseudocapacitor, and the combination of these two types is called the hybrid capacitor.

The electrostatic capacitor's capacitance consists of two conductive electrodes, a positively charged electrode and a negatively charged electrode. And between the two electrodes is a non-conductive dielectric in Figure 3.2. The dielectric keeps the charges separated, forming an electrical field that stores electrical energy. The electrostatic capacitance can be calculated with the following Equation 3.1,

$$C = \epsilon_0 \epsilon_r A / d \quad (3.1)$$

In this equation, A is the electrode area, d is the distance between two electrodes, ϵ_0 is the permittivity of vacuum, and ϵ_r is the dielectric medium constant, also known as relative static permittivity[20]. According to Equation 3.1, the bigger A is, or the smaller d is, the bigger the electrostatic capacitance will be. Using different dielectric mediums (different ϵ_r -value) is also a usual way to change the electrostatic capacitance, based on Equation 3.1. It needs to be noticed that, Equation 3.1 is universal for all the parallel-plate capacitors, including the following electrolytic capacitor.

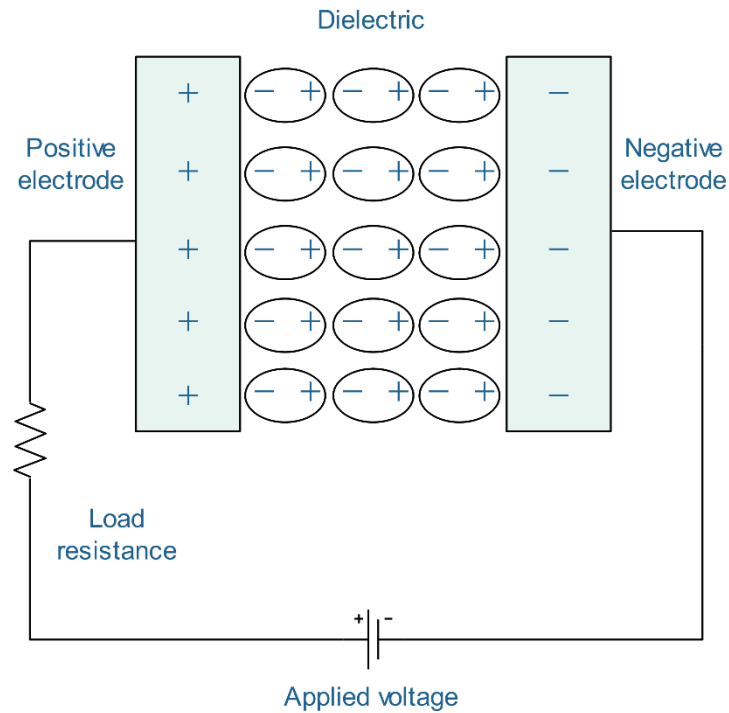


Figure 3.2 The electrostatic capacitor's configuration, which includes a positively charged conductive electrode and a negative charged conductive electrode with a non-conducting dielectric.

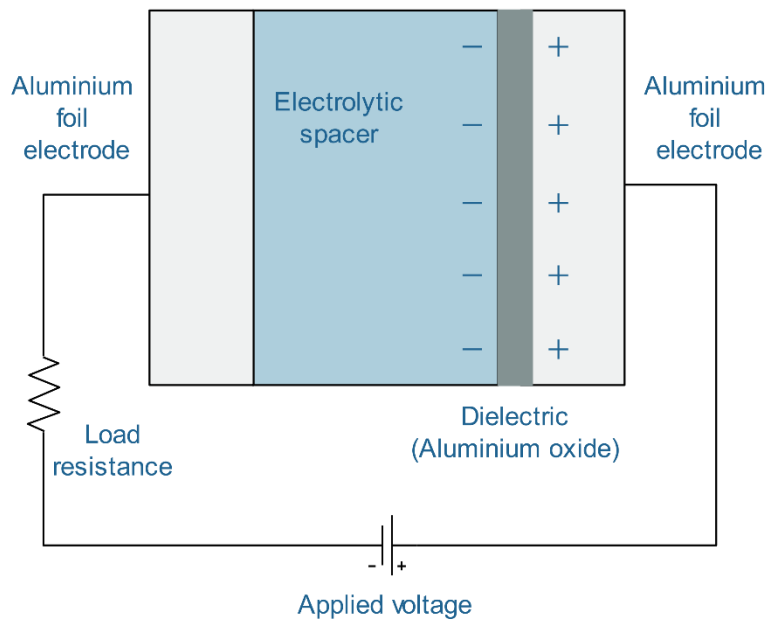


Figure 3.3 The electrolytic capacitor's configuration with the aluminum foil as the anode and its aluminum oxide layer as the dielectric. Unlike other capacitors, the liquid or solid electrolyte works as the cathode electrode in the electrolytic capacitor.

An electrolytic capacitor (Figure 3.3) is an asymmetric capacitor that consists of the metal foil (usually in Al[21], Ta[22], and Nb[23]) as the anode electrode and the electrolyte (either liquid or

solid) as the cathode electrode. The oxidation film on the surface of the metal foil (anode electrode) acts as the dielectric. Usually, the oxidation layer is relatively thin, which means the value of d is quite small. According to Equation 3.1, capacitors with small d can provide much higher capacitance than the electrostatic capacitor mentioned above. The metal foil is usually etched to increase the surface area A to increase the capacitance, according to Equation 3.1. Also, the etching process creates millions of micro-scaled structures on the surface of the metal foils, forming a rough surface that enables the electrodes a good contact with the electrolyte, hence decreasing the series resistance of the electrolytic capacitors and increasing the electric performance of the electrolytic capacitor.

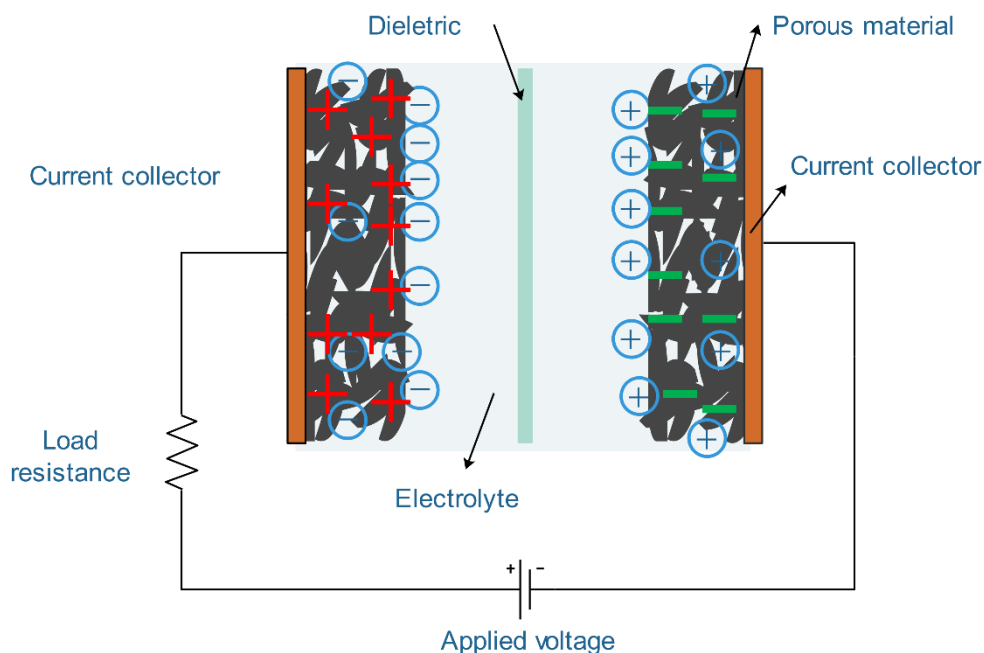


Figure 3.4 The configuration of the electric double-layer capacitor. The black-shaped material covering the current collectors is the materials with large specific surface area, such as graphene[24], activated carbon[25], and carbon nanotube[26].

The electrochemical capacitor also noted as the supercapacitor, or the ultracapacitor, is a high-capacity capacitor. It stores charge in the electric double layer at the electrode-electrolyte interface and by electrochemical reactions[20]. It consists of two electrodes and a liquid/solid electrolyte. The charges are stored at the interfaces of the electrode/electrolyte or via Faradaic reactions, which will be later explained in Section 3.1.1. An electrochemical capacitor is categorized into electric double layer capacitor [27-29], pseudocapacitor[30-33], and hybrid capacitor[34-36], combining the electric double layer capacitor and pseudocapacitor[37-39]. The electrochemical capacitor achieves several orders of magnitude higher capacitance than that of electrolytic[40-42] and electrostatic capacitors[43-45]. Electric double-layer capacitor (EDLCs) (Figure 3.4) is an electrochemical capacitor that stores electrostatic charge via reversible adsorption of ions in the electrolyte onto the surface of electrode materials (Non-Faradaic process). Usually, the electrode materials should be highly conductive, electrochemically stable, and have a large specific surface area (SSA)[46], such as porous carbon materials[47, 48] or 2D materials[49, 50] with large SSA, to achieve good performance. Besides, the shape of the porous will also influence the electrochemical performance.

Models of the electric double-layer are built and introduced, to understand more about the electric double-layer. The Helmholtz model is put forward by von Helmholtz[51]. The model in Figure 3.5 shows, on the solution side, the same amount of opposite charge (opposite to the electrode side) accumulated near the electrode-electrolyte interface, thus forming an electric double layer. i.e., the Helmholtz model. Later, the Gouy-Chapman model is proposed, a diffusion layer is introduced to the original Helmholtz model due to the thermal fluctuations[52]. A diffusion electric double layer is involved in the model, rather than rigid distribution like the Helmholtz model. The concentration of the distribution of counterions follows the Boltzmann distribution[53]. The Gouy-Chapman model fits reality better than the Helmholtz model. However, it is based on an assumption, i.e., the ions are point-like, which means the ions' size is ignored. So the Stern modification of the Gouy-Chapman model is put forward to consider the size of ions.

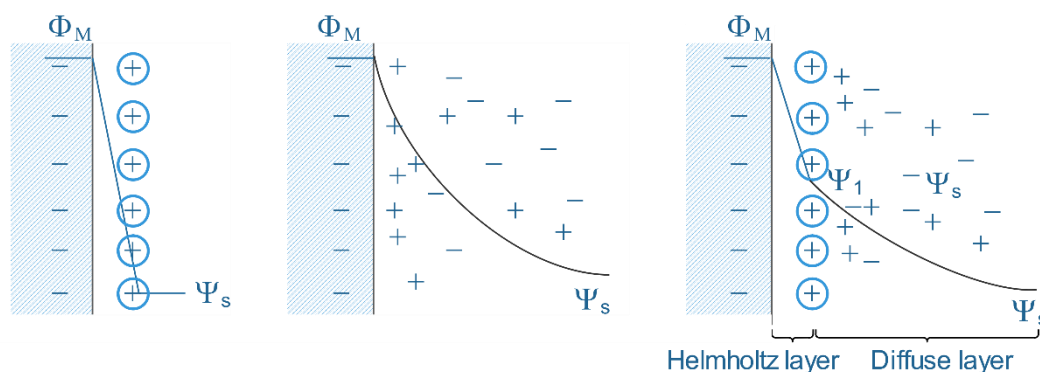


Figure 3.5 Helmholtz model (left), Gouy-Chapman model (middle) and Gouy-Chapman- Stern model (right)[54]

According to the model, the rigid inner layer close to the interface is called the Helmholtz layer. The capacitance C_H of the Helmholtz layer is a constant, independent from the applied voltage. The capacitance of diffusion layer C_D is in series connection with C_H . So, the total capacitance C of the Gouy-Chapman-Stern layer is

$$1/C = 1/C_H + 1/C_D \quad (3.2)$$

When the low voltage is applied, and C_D is smaller than C_H , C_D contributes mainly to capacitance C . While at high voltage, the value of C_D is large, the value of C approaches more to the value of C_H .

As the complement of the double-layer electrochemical capacitors, the pseudocapacitors store charge in the electrosorption processes, redox reactions, or intercalations processes on the electrode surfaces. The pseudocapacitance exists on the electrode's surface and inside the electrode, providing much higher capacitance and energy density than a regular double-layer capacitor. Metal oxides[55] and conductive polymers[56] are often used as the active materials in the pseudocapacitor, such as MnO_2 [57], RuO_2 [58], Co_3O_4 [59], Polypyrroles[60], Polyaniline[61], and Polyvinylferrocene[62], etc. The theoretical specific capacitance of the electrode materials, the conductivity of the electrodes, the morphology of the electrode materials, and the employment of various electrolytes will all have a huge influence on the electrochemical performance of the pseudocapacitors. The theoretical specific capacitance and the pseudocapacitors' energy density are usually

higher than the electric double-layer capacitor. In reverse, the electric double-layer capacitor has higher power density, superior rate performance, and cyclic performance (excellent electrochemical stability).

A hybrid capacitor[63] combines an electric double-layer capacitor electrode, storing charges in a non-Faradaic way, with a pseudocapacitor electrode storing charge in a Faradaic way. Hybrid capacitor combines the advantage of batteries and electric double-layer capacitors, achieving a higher energy density and longer cycle life.

3.1.1 Faradaic process and non-Faradaic process

On the electrode-electrolyte interface, both non-Faradaic processes and Faradaic processes can take place. Non-Faradaic processes usually take place in the electric double-layer capacitor. Theoretically, there are no electron transfers across the electrode-electrolyte interface during the non-Faradaic process. The charges are stored electrostatically. The positive charges and negative charges reside by the side of two interfaces, separated by dielectrics, such as air or oxidized film. In cyclic voltammetry curve, the non-Faradaic process exhibits a flat profile.

For the Faradaic process, the electrons transfer through the interfaces, and a redox reaction takes place. The whole process follows Faraday's law, i.e., the react chemicals' mass is a function of the current passing the electrode, as shown in Equation 3.3.

$$m = E_q / t = E_q Q \quad (3.3)$$

In Equation 3.3, m is the mass of the reacted chemicals, I is the current flowing through the electrode, t is the time, Q is the consumed charge over time, and E_q is a constant. E_q is named as the electrochemical equivalent. Its value can be achieved via Equation 3.4.

$$E_q = M / nF \quad (3.4)$$

F is Faraday constant, $F = 96485 \text{ C/mol}$, M is the molar mass of the reacted chemicals (g/mol), while n is the charge number of ions of chemicals. The Faraday law fits with all the redox reactions on the electrode. The Faradaic process is the dominant process in the pseudocapacitors and batteries. Usually, the Faradaic process's existence can be determined by checking the reduction and oxidation peaks in cyclic voltammetry, as shown in the later Section 3.4.2.

3.1.2 The configurations of electrochemical capacitors

The conventional configuration of the electrochemical capacitor includes two electrodes, the separator and the electrolyte. The widely used configuration of capacitors is the cylinder capacitor or the button capacitor impregnated with an electrolyte.

The proper electrode materials should be highly conductive to achieve superior electric performance. For electric double-layer electrode material, a high specific surface area is also required. Highly porous carbon[64], carbon nanotube[65], graphene[66] with a large specific surface area

(maximum 3000 m²/g) are commonly employed as electrode materials.

The electrolyte can be either solid or liquid, organic or inorganic. The aqueous electrolyte, such as KOH or H₂SO₄, the working voltage is usually under 1.23 V because the electrolysis of water in the electrolyte requires a minimum potential difference of 1.23 V. The organic electrolyte usually dissociates at a voltage above 2.5 V, providing a much higher working voltage.

The membrane is usually used as the separator, which is highly ionic conductive instead of being electronic conductive. Polymer[67] or paper[68] separators are generally used in the electrochemical capacitor with organic (nonaqueous) electrolyte. For the aqueous electrolyte, glass fibers[69] or ceramic[70] separators are widely employed.

In addition to the conventional parallel-plate capacitors, cylindrical capacitors[71], button cell capacitors[72], and parallel-plate capacitors[73], the interdigitated capacitors (also called comb structure)[74] is also an option for “unsealed capacitors” (Figure 3.6). The interdigitated capacitor is a new type of micro capacitor that features flexibility, transparency. Microcapacitors are mainly used in portable, flexible, and smart electric devices, such as foldable cellphones, google glasses, and microsensors. Compared to the conventional supercapacitor, its smaller size makes microstructure a promising candidate for the integration with other microelectronic devices[75]. In addition, the interdigitated microcapacitors can be used as sensor systems or photoelectronic devices (e.g., solar cells), because the open structure provides a path for gas/ light to get access to the system easily. The detailed information will be introduced in the following Section 5.1.

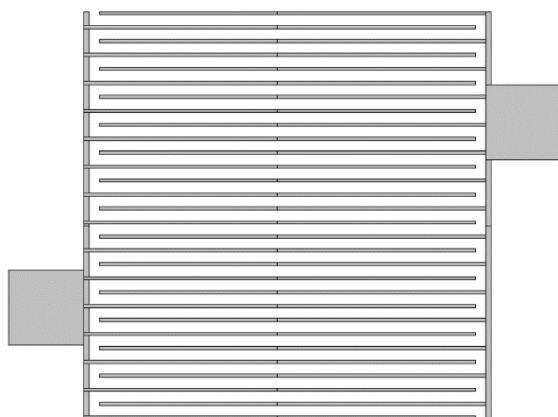


Figure 3.6 The schematic diagram of the interdigitated pattern, produced via lithography. The size of the overall interdigitated pattern is on a scale of several millimeters. The width of each finger of the interdigitated electrode can be several micrometers.

3.1.3 Popular research directions

The choice of electrode materials (0D, 1D, 2D, and 3D nanomaterials) is always the hottest topic in the field of supercapacitors. The 0D materials, such as nanoparticles and quantum dots[80] are widely used in the industry as the primary active materials of the electrodes. Nanotubes and nanowires[76, 77] are the commonly used 1D material. The 2D materials, especially graphene[78] and the transition metal carbide MXene[79], have arisen considerable attention in recent years. Moreover, 0D can be employed with other 0D, 1D, and 2D materials to form 3D nanostructure[81-

83]. The small size of the 0D material makes it easily accessible to the electrolyte and appropriate for any configuration of energy storage devices. However, the 0D material has lower electrical conductivity due to its point-to-point contact[84]. It usually requires an additional binder to bond the nanoparticles, leading to decreased power density. The 1D material has better electrical conductivity and doesn't need a binder. However, the packing density of the 1D material is low, resulting in lower power density[85]. The 2D material has a fast charging and discharging speed, because of its high specific area which has a sufficient contact with electrolyte. The 2D material's in-plane conductivity is high, but the electronic conductivity between two layers is quite low[86]. Restacking of the layers is a huge problem[87]. Therefore, the 0D and 2D materials are mixed to construct the 3D materials[88-90], which can resolve the restacking issues and increase the conductivity efficiency between planes.

Also, the configurations of supercapacitors are one of the famous research directions. The emergence of portable and foldable electric devices brings the development and prosperity of flexible supercapacitors. The electrodes, the separator, and the encapsulated shell are adjustable that they can be fitted into different shapes. There are roughly three categories of flexible supercapacitors: fiber-like 1D flexible supercapacitors[91], which can be used in flexible microelectronic devices, paper-like 2D flexible supercapacitors[92], which can be employed in foldable mobile phones, such as Huawei Mate Xs, and 3D porous flexible supercapacitors[93] which is suitable for large scale power supplier.

3.2 Techniques of assembling the interdigitated capacitor

The interdigitated capacitor assembly process includes the "printing" of the interdigitated structure on the substrate via photolithography and the bonding of the electrodes onto the chip carriers. The theoretical mechanism and the overall process of lithography are introduced in this chapter and the experimental instruments employed during the capacitor assembly, i.e., the mask aligner, the evaporator, and the bonder.

3.2.1 Photolithography

Photolithography, also known as optical lithography, or UV lithography, is commonly used in the semiconductor industry as a microfabrication method. It transfers the geometric pattern from a mask to a photosensitive photoresist coated on the substrate. The photolithography process includes the photoresist coating, exposure, and developing in Figure 3.7.

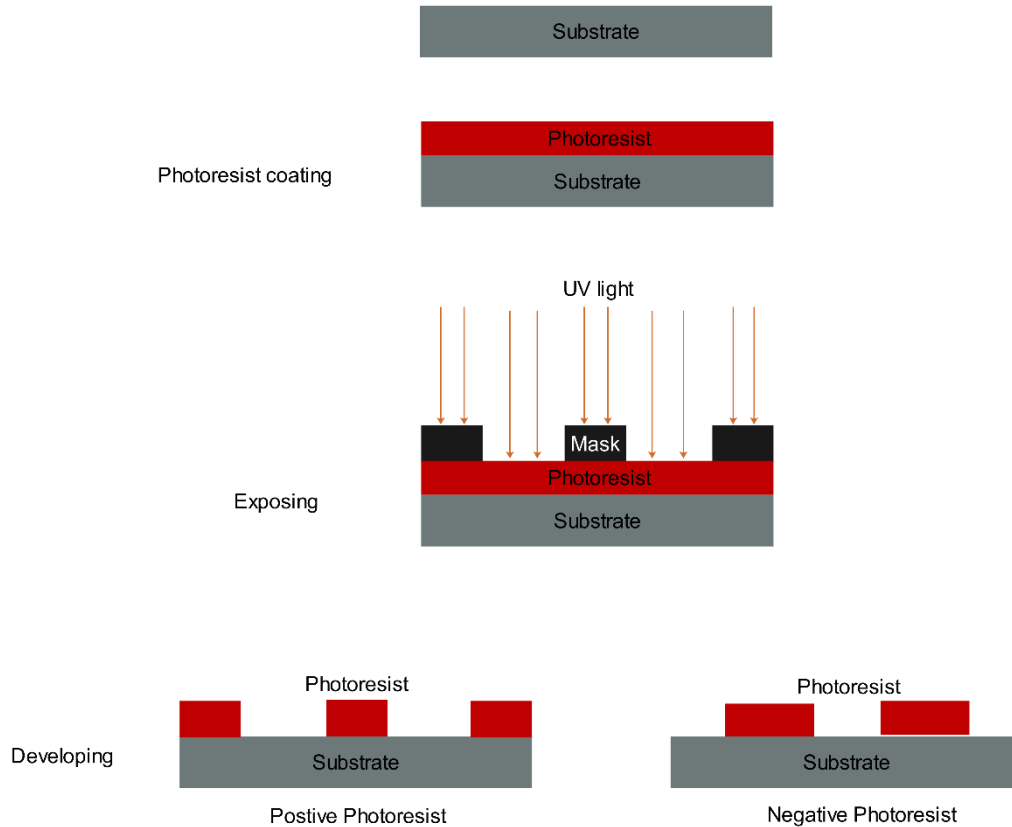


Figure 3.7 The flow chart of the lithography process, including photoresist coating, exposing and developing. It briefly explains how the positive photoresist and the negative photoresist work differently.

The first step of photolithography is the photoresist coating. A photoresist is a resist that can be chemically changed because of the exposure to specific wavelengths applied. There are two kinds of photoresists, positive photoresist and negative photoresist. Their different working function will be illustrated in the third step (Figure 3.7). The photoresist (introduced later in this session) is spin-coated on the substrate, forming a photoresist film. The substrate coated with photoresist film is subsequently baked on the hot plate (soft bake) at a specific temperature for a short time (usually at 100 °C for 1 min) to remove the residual solvent, e.g., water inside the photoresist coating film. The other purpose of the soft bake is to enhance the resist adhesion to the substrate and to prevent the formation of diazonaphthoquinone (DNQ) -based resists during the exposure. DNQ is a side-product of the photoreaction. This procedure also minimizes the dark erosion of positive resists during development[94] (Cited from published book Photolithography Basics of Micro structuring).

The second step of lithography is exposure. A mask aligner (Karl Süss) is employed in the exposure process. The machine employs ultraviolet light, transferring a template or a pattern from a photomask to a micro Si substrate. The type of mask aligner is shown in Figure 3.8.



Figure 3.8 The mask Aligner (Karl Süss) is used to transfer the pattern from the mask to the substrate.

The photomask is prepared with Cr coated quartz substrate via electron beam lithography. The photomask is usually a quartz plate covered by a Cr layer, with some transparent areas that allow light to pass through it. The transparent areas (non Cr coated area) and the non-transparency areas (Cr thin-film coated area) form the pattern/template on the substrate in Figure 3.9[94].

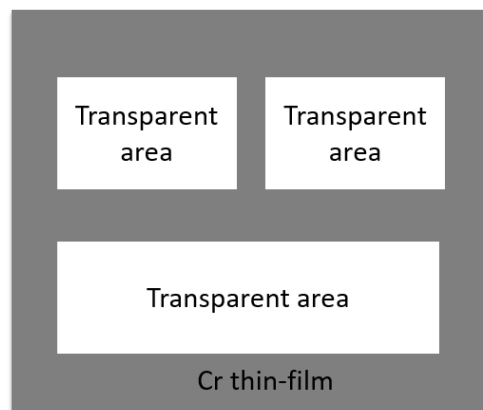


Figure 3.9 The schematic graph of a photomask with a simple pattern, formed by three transparent areas and Cr thin-film area.

The photomask is placed onto the Si substrate coated with photoresist (close contact) to complete the exposure. The ultraviolet light irradiates onto the mask, and further reaches the photoresist-coated Si substrate surface through the transparent areas. The whole exposure process lasts for a specific time (on the scale of a minute or second).

The third step after the exposure is the developing process. The substrate is placed in the developer solution for a particular time. The developer can dissolve photoresist selectively. The photoresist that needs to be developed has a much higher dissolution rate than the photoresist area's dissolution speed that should remain on the substrate.

As mentioned before, photoresists are categorized into positive photoresists and negative photoresists. The dissolution rate of the exposed area and the unexposed area of the coated photoresist is different, leading to the realization of a structured photoresist mask[94]. For the positive

photoresist, the area exposed to UV light will be dissolved in a developer, and the UV light unexposed photoresist will stay on the substrate. While for the negative photoresist, the area exposed to UV light will remain, and the unexposed area will be soluble in the developer (Figure 3.7).

After development, the pattern of the photomask is successfully displayed on the substrate. Later, the substrate is dipped into the stopper solution (i.e., deionized water) to stop overreacting between the developer and the photoresist, preventing the damage of the as-prepared pattern on the substrate.

3.2.2 Evaporating

Evaporator (Figure 3.10) is usually used for thin-film deposition. Metal is evaporated under vacuum conditions (10^{-5} mbar to 10^{-6} mbar) by either electron beam or thermal heating. The metal is evaporated and ejected onto the target sample during evaporation, cooling down and forming a thin metal film on the sample surface. The electron beam is usually employed to evaporate titanium, nickel, and platinum, etc., while thermal heating is for evaporating gold, silver, and gold germanium. The evaporator used here is BOC-Edwards Auto 500.



Figure 3.10 The evaporator BOC-Edwards Auto 500.

The liftoff procedure is carried after evaporation. The substrate covered with metal thin-film is soaked into the hot acetone ($60\text{ }^{\circ}\text{C} - 70\text{ }^{\circ}\text{C}$), so the residual photoresist will dissolve in it. Hence the above metal thin-film will exfoliate from the substrate. In contrast, the metal thin-film that contacts directly with the substrate will still stick on the surface. Until this step, an interdigitated gold structure is lithographically printed on the substrate.

3.2.3 Bonding

The bonder (Kulicke & Soffa 4123 Wedge Bonder, Figure 3.11 (left)) is a machine using thin Al wire ($\text{Al}_{0.99}\text{Si}$, diameter $25\text{ }\mu\text{m}$) to connect the gold interdigitated structure to the chip carrier. The schematic graph in Figure 3.11 (right) shows how the interdigitated pattern is electrically attached to the chip carrier.

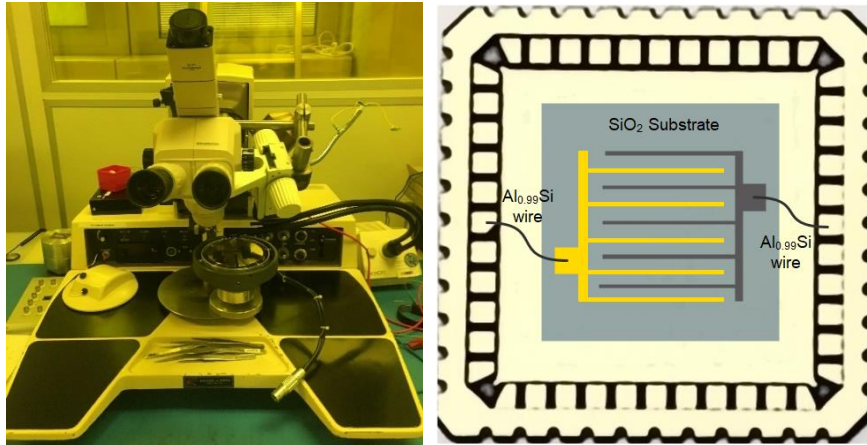


Figure 3.11 Left: Kulicke & Soffa 4123 Wedge Bonder. Right: The schematic graph showing how the gold interdigitated pattern is connected to the chip carrier.

3.3 Materials characterization techniques

To characterize the morphology, composition, and surface information of as-prepared β -FeSi₂ nanoparticles, traditional techniques such as X-ray diffraction, Brunauer–Emmett–Teller method, scanning electron microscopy, and X-ray photoelectron spectroscopy are employed. A brief introduction of the above experimental apparatuses is introduced in this chapter.

3.3.1 Scanning electron microscopy

Scanning electron microscopy (SEM)[95] [96] (Figure 3.12) is a typical laboratory apparatus, which is widely used in the field of material science and engineering. SEM's mechanism is based on the principle of scanning materials with a highly focused high-energy electron beam to excite the atoms, emit secondary electrons, and backscattered electrons out of the specimen. The secondary electrons and backscattered electrons are collected by a detector locating above the sample and converted into optical signals by a scintillator. They again are converted into the electrical signals by a photomultiplier tube and an amplifier, thus displaying a scanned image synchronized with the electron beam. When an electron beam hits a point on the sample surface, a corresponding bright spot shows on the computer screen, and the brightness of the spot is proportional to the excited electron energy. SEM can be used to perform the three-dimension topography of nanoparticles, metals, and alloys, etc., and to analyze the composition of materials (i.e., the elemental mapping) of a particular area. Besides, biological sample observations can also be conducted with SEM.

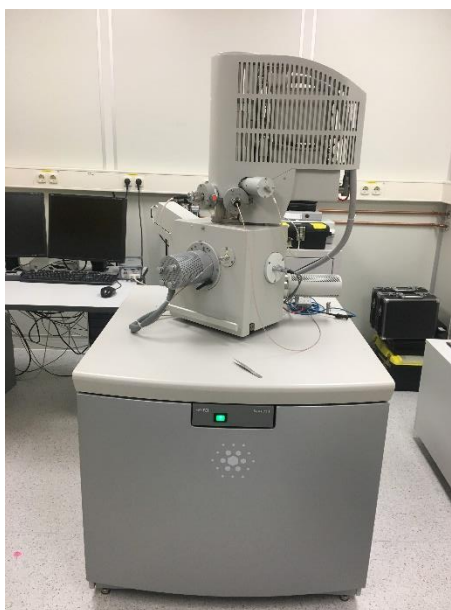


Figure 3.12 The photo of Scanning Electron Microscope (Inspect F, FEI).

3.3.2 Focused ion beam

The equipment of the Focused ion beam is shown in Figure 3.13[97]. When the focused ion beam is shot onto the tested surface, the secondary ions and secondary electrons are emitted from the surface, forming an image, similar to SEM. Except for SEM, the focused ion beam can also cut samples by bombarding and etching the atoms away from the sample. The focused ion beam instrument used in this work is produced by FEI (Helios NANO LAB), including a scanning electron microscopic component.



Figure 3.13 The photo of the focused ion beam machine (Helios NANO LAB).

3.3.3 X-ray diffraction

X-ray diffraction (XRD) is a non-destructive analysis technique widely used in material science[98]. During X-ray diffraction measurement, when a beam of focused monochromatic X-rays is shot onto the sample crystal, the electrons around the atoms in the crystal vibrate and produce electromagnetic radiations. The Bragg equation (Equation 3.5) is the foundation of XRD theory. In Equation 3.5, n is an integer ($n > 0$), λ is the wavelength of the incident waves, θ is the angle formed by the incident waves and the crystal plane, and d is the distance of the two parallel crystal planes.

$$n\lambda = 2d \sin \theta \quad (3.5)$$

All the atomic diffraction waves in the direction satisfying the Bragg Equation will add up (constructive interference). In contrast, all the atomic diffraction waves in the direction which don't meet the Bragg Equation will diminish to zero (destructive interference). Due to the periodicity of crystal structure, the emitted waves will superimpose. The diffraction pattern with diffraction peaks is achieved as a result of the interference of numerous atomic scattered waves.

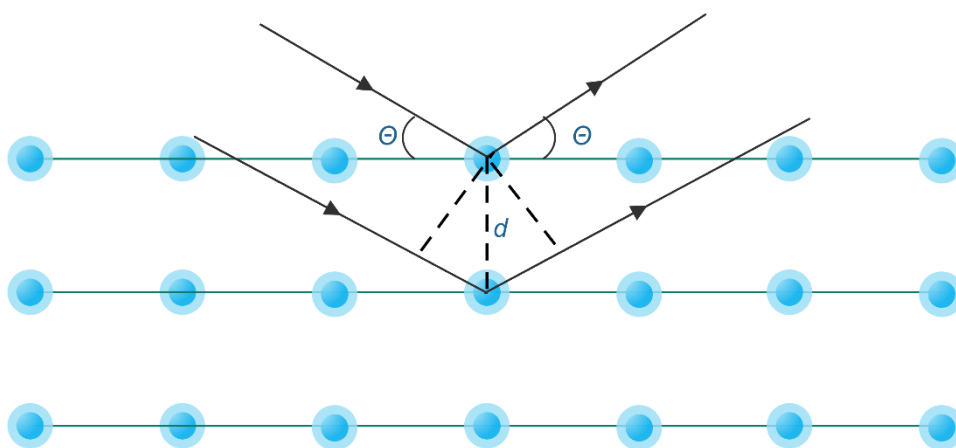


Figure 3.14 The schematic diagram of the incident waves and their corresponding atomic diffraction waves on the crystal planes.

In the material research, X-ray diffraction is employed to figure out the crystalline structure, crystallite size, and compositions of nanoparticles. Different crystals have different diffraction patterns based on the size, shape, species of atoms, and their position in the unit cell. Other anode targets, such as copper target or cobalt target, are employed in the X-ray diffraction. However, using different targets mainly affects the diffraction peak positions, and the relative strength of the diffractions is slightly different.

3.3.4 X-ray photoelectron spectroscopy

X-ray photoelectron spectroscopy (XPS) is widely used as a surface chemical analysis technique[99]. It is a quantitative energy spectrum technology employed to figure out the elemental composition of the materials, the chemical state and the electronic state of any element, etc. The

materials that need to be measured are exposed under X-ray. The XPS machine measured the kinetic energy and the number of the escaped electrons, hence achieving the X-ray photoelectron spectroscopy.

More precisely speaking, during the measuring process, the electrons in the atoms or the molecules are irradiated by a beam of monochromatic X-rays (Figure 3.15), and the kinetic energy $E_{kinetic}$ of the emitted electrons is measured simultaneously to analyze the elemental composition, the chemical state of the tested sample surface. Usually, the XPS test needs to be conducted under a high vacuum condition ($10^{-9} - 10^{-8}$ mbar). But in recent years, there is a new XPS instrument named the near-ambient-pressure X-ray photoelectron spectroscopy (NAP-XPS) that allows the testing process to run at a higher pressure, making it possible to test the biology samples, liquids, or gases[100, 101]. The testing depth ranges from 1 nm and 10 nm underneath the material surface.

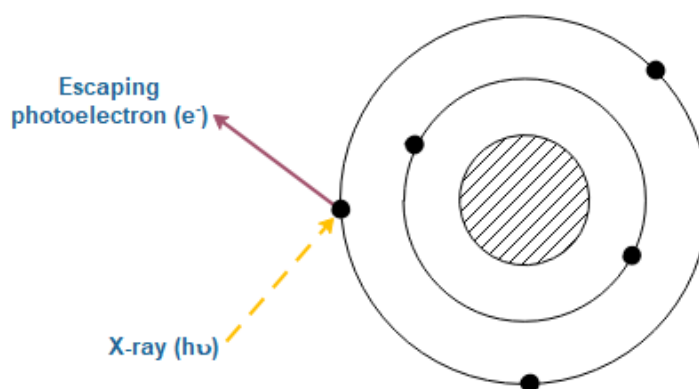


Figure 3.15 Schematic graph of photoelectron emission irradiated by X-ray.

According to the Ernest Rutherford Equation:

$$E_{binding} = E_{photon} - E_{kinetic} - \varphi = h \cdot \nu - E_{kinetic} - \varphi \quad (3.6)$$

$E_{binding}$ is the binding energy, while $E_{photon} = h\nu$ is the energy of X-ray photon. The monochromatic X-rays employed in the XPS equipment nowadays are either the Al $K\alpha$ X-ray with the E_{photon} of 1486.7 eV or the Mg $K\alpha$ X-ray with the E_{photon} of 1253.6 eV. The kinetic energy $E_{kinetic}$ and the number of electrons emitted can be measured by an electron energy analyzer and an electron detector. φ is the XPS instrument's work function, rather than the testing samples, which is caused by the photoelectron absorption of the XPS detector. The value of φ is only a few eV and usually can be negligible[102].

3.3.5 Brunauer–Emmett–Teller

Brunauer–Emmett–Teller method (BET) is a theoretical module that is commonly used to explain gas molecules' physical adsorption onto a solid surface[103]. The BET module is widely used in particle surface adsorption research to characterize nanoparticles' specific surface area.

A certain amount of the produced nanoparticles is placed in a testing chamber cooled by liquid nitrogen. The gas nitrogen is used as the adsorbate, with the hydrogen/helium works as the carrier gas. The nitrogen and hydrogen/helium are mixed in a certain ratio, and go through the

tested nanoparticles under a certain relative pressure. The physical adsorption of nitrogen takes place on the surface and reaches the equilibrium state. When the temperature of the testing chamber reaches room temperature, the desorption of nitrogen happens. By measuring the relative pressure and the area of the desorption peaks, the nitrogen adsorption volume V_m of the monolayer is calculated.

This theory builds the BET equation, connecting the monolayer adsorption volume V_m with the multi-layer adsorption volume V . And the specific surface area S is calculated by Equation 3.7 and 3.8 below.

$$\frac{p}{V(p_0 - p)} = \frac{1}{V_m \cdot C} + \frac{C - 1}{V_m \times C} \times \frac{p}{p_0} \quad (3.7)$$

In Equation 3.7, p is the partial pressure of the inert gas, p_0 is the saturated pressure of the inert gas at the liquid nitrogen temperature. C is noted as a BET constant describing the interaction condition between the adsorbent and the adsorbate. So the specific surface area S is achieved in Equation 3.8. N_A represents the Avogadro number, m is the mass of the tested materials. s and V_{mol} represent the adsorption cross-section and the molar volume of the adsorbate gas, respectively.

$$S = \frac{V_m N_A s}{m V_{mol}} \quad (3.8)$$

For the adsorbate gas nitrogen,

$$\frac{N_A s}{V_{mol}} = 4.36 \quad (\text{m}^{-1}) \quad (3.9)$$

3.4 Electric measurement

In this chapter, the configuration of measurement setup and the detailed information of measuring condition is introduced. To figure out the electric performance of micro capacitors with β -FeSi₂, potentiostatic and galvanostatic test is carried out, with source meter Keithley 2400. To understand the mechanism of the charging and discharging process of micro capacitors with β -FeSi₂, cyclic voltammetry, and linear sweep voltammetry are employed. The principle and needed types of equipment are introduced in the following text.

3.4.1 Potentiostatic and galvanostatic test

Potentiostatic tests and galvanostatic tests are pretty frequently employed measuring methods in the electrochemistry field. The galvanostatic test (Figure 3.16) is to impose a constant current on the tested device, measuring the time-dependent voltage plot (V-t curve)[54].

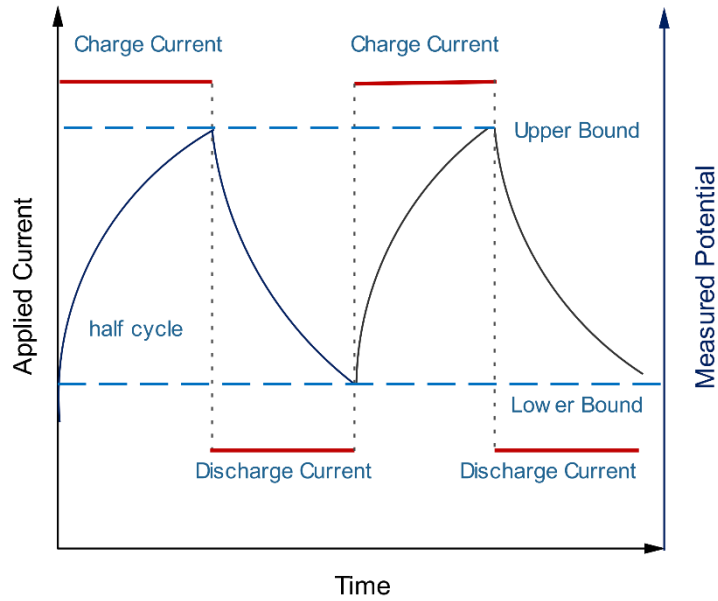


Figure 3.16 Galvanostatic test of thin-film batteries as an example[104]. The red horizontal line represents the applied current (left), and the blue curved line is the measured potential (right).

Potentiostatic test applies a specific constant voltage to the electrical device, e.g., capacitor, and measures the time-dependent transient current ($I-t$ curve) or time-dependent current density ($j-t$ curve) (Figure 3.17)[105]. And the stored charge Q is achieved by integrating the discharge current transient over the discharge time. Usually, in the measurement, different voltages are applied onto the capacitor to study the voltage-dependent current ($V-I$ curve) or charge behavior ($V-Q$ curve)[54].

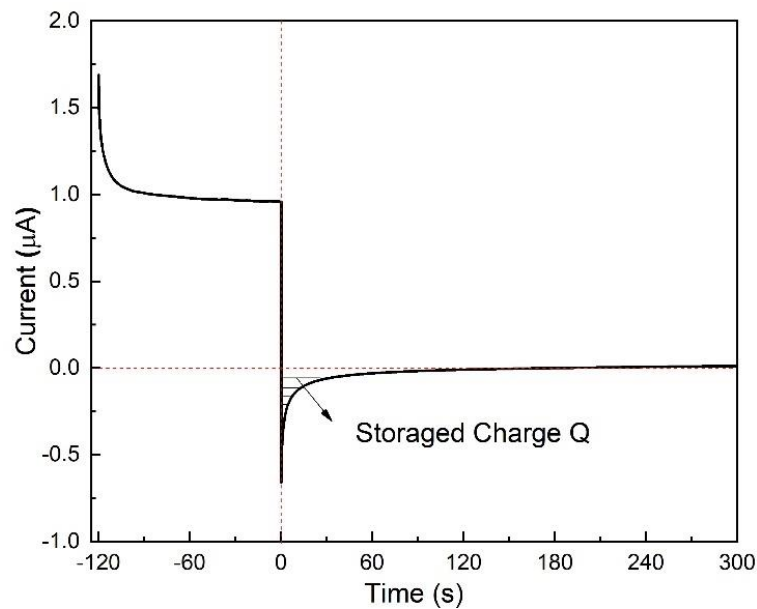


Figure 3.17 The current transient over time $I(t)$ of a capacitor's potentiostat measurement (at a particular applied potential). The current transient behaves exponentially, and the area filled with the horizontal bars represents the stored charge Q .

3.4.2 Cyclic voltammetry

Cyclic voltammetry (CV) is a commonly used electrochemical analysis technique, researching electron transfer and probing subsequent chemical reactions[106]. CV measurement can be conducted in either the two-electrode system (composed of the working electrode and the counter electrode) or the three-electrode system (composed of the working electrode, the reference electrode, and the counter electrode). The potential of the working electrode increases at a certain speed (V/s or mV/s), from a starting voltage to an ending voltage. Then, the working electrode potential decreases back to the starting voltage with the same speed. Thus one cycle is completed (Figure 3.18 (a)). Such a procedure can be repeated as many times as needed. The measured current is plotted versus working electrode potential (Figure 3.18 (b)). In the CV curve, information about oxidation and reduction reaction can be achieved and the reversibility condition of a redox reaction, the absorption and desorption process of gas molecules. Cyclic voltammetry can also be conducted in the two-electrode system in the batteries and supercapacitors research.

The background current (blue dashed line) in Figure 3.18 (right) usually means the non-Faradaic process, i.e., the electric double-layer capacitance. In contrast, the peaks of the red line represent the Faradaic process, i.e., oxidation and reduction process. Such characteristics will help figure out the Faradaic/ non-Faradaic process in a CV diagram.

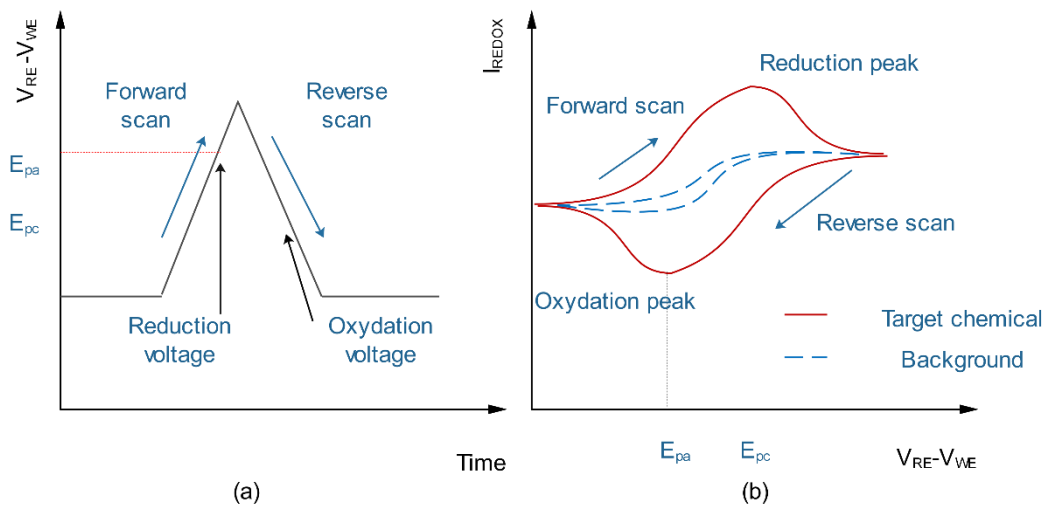


Figure 3.18 Single-cycle of cyclic voltammetry scan shows how the applied voltage varies with time (left). The cyclic voltammetry curve of the applied voltage-dependent current (right). The blue arrows indicate the direction of the scanning voltage[107].

A simple capacitor can be viewed as an equivalent R-C circuit, composed of resistors (R) and capacitors (C)[54]. The transient current of potentiostatic measurement is an exponential function of time. Take the simplest R-C (Figure 3.19 (a)) series circuit, for example, the transient current

$$I = I_0 \exp(-t / RC) \quad (3.10)$$

Parameter RC , also named as τ , is the time constant of the circuit, means the time it takes to charge to 63.2% ($1-1/e$) of capacity. The practical current transient can be fitted with varied forms

of exponential formula, based on Equation 3.10. For example, a bi-exponential equation consists of two mono-exponential equations with different time constants, two resistances, and two capacitors. The tri-exponential equation consists of three-time constants, three resistances, and three capacitors.

Another basic form of the R-C circuit is a parallel circuit (Figure 3.19 (b)). Complicated circuits are composed of these two basic circuits, sometimes with the introductory of inductors (L). For example, the electrochemical capacitor's circuit model is usually more complicated, and more elements such as Faradaic resistance are introduced.

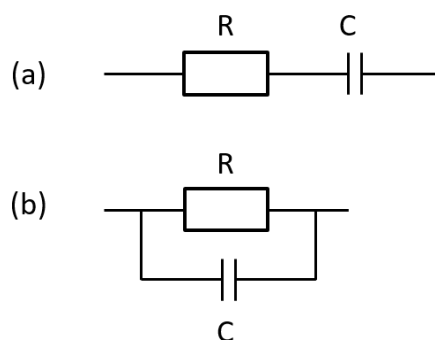


Figure 3.19 The two basic R-C circuits: series circuit (a) and parallel circuit (b).

3.4.3 Linear sweep voltammetry

Linear sweep voltammetry (LSV) applies a specific voltage (lower voltage V_1) on the working electrode. The applied voltage is increased stepwise (increasing unit: mV/s) until reaching the final voltage (higher voltage V_2)[108]. Rotating disk electrode (RDE) is employed in linear sweep voltammetry in the electrocatalyst field, such as the study of oxygen evolution reaction (OER), oxygen reduction reaction (ORR), hydrogen evolution reaction (HER), and hydrogen reduction reaction (HRR). RDE, also known as a hydrodynamic electrode, is a high-speed rotating electrode in a three-electrode system. The characteristics of RDE are that the mass transference and current density are dependent on electrochemically active materials[109].

3.5 Charge transfer mechanism

There are roughly three mechanisms describing the charge transfer behavior of semiconductors, i.e., space-charge-limited current (SCLC)[110, 111], Fowler-Nordheim tunneling[112], and Poole-Frenkel transport mechanism[113].

Fowler-Nordheim tunneling usually happens in metal-semiconductor junctions, indicating electrons tunneling through barriers in a high electric field. And its current-voltage can be fitted with the following equation[114].

$$I \propto V^2 \exp(-a/V) \quad (3.11)$$

Poole-Frenkel transport mechanism happens when electrons move through insulators in a relatively high electric field. And it follows the equation[115, 116].

$$I \propto V \exp(aV^{0.5}) \quad (3.12)$$

According to R. N. Pereira's study on silicon nanocrystals, the silicon nanocrystals have similar electric behavior with the β -FeSi₂ NPs[122], and its charge transfer behavior can be fitted with Equation 3.13. In the equation, the steady-state current is used to avoid the time influence on the current at different applied voltage. The steady-state current is the current that reaches a plateau and keeps stable afterward. When m equals one, and the current is linearly correlated with voltage, it means the current-voltage follows the Ohmic behavior. When m equals 2, it indicates that the space-charge-limited current dominates.

$$I = aV + bV^m \quad (3.13)$$

The charge transfer behavior of semiconducting polymers, conducting polymers[117], metal oxides[118], and Si nanocrystals[119, 120] can be interpreted by the space-charge-limited current model. The space-charge-limited current appears when the uncompensated current is ejected into the whole system. In this case, the current density follows Equation 3.13[110, 121],

$$J = \frac{9}{8} \mu_{eff} \epsilon_0 \epsilon_r \frac{V^2}{d^3} \quad (3.14)$$

where J is the current density, V is the applied voltage.



4 β -FeSi₂ Synthesis

In Chapter 4, the synthesis β -FeSi₂ regarding the basic properties of β -FeSi₂, the synthesis mechanism, and its setup will be introduced. β -FeSi₂ NPs are synthesized with the direct gas-phase method in this chapter, and the appropriate synthesis parameters are fixed to produce β -FeSi₂ with a relatively uniform size. Nanoparticle synthesis control is the first step to maintain the reproducibility of the capacitors' electrical performance.

4.1 Basic information of β -FeSi₂

Orthorhombic β -FeSi₂, i.e., iron disilicide, is a stable, non-toxic semiconductor with an indirect bandgap is 0.78 eV[123] direct band gap of 0.83 – 0.87 V[124, 125]. It is thermodynamically stable at room temperature. Usually, β -FeSi₂ can be used in the field of photoluminescence[126-129]. Moreover, its large absorption coefficient is over 10^5 cm⁻¹ at 1 eV (much larger than that of crystalline silicon), which is a good option for solar cell materials[130-132].

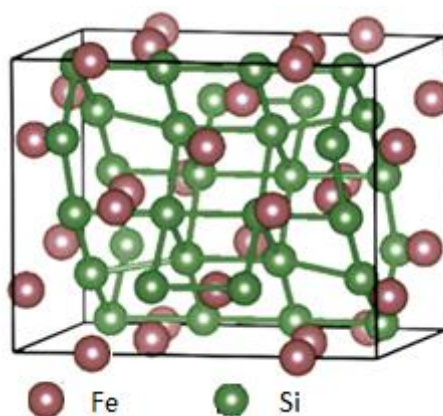


Figure 4.1 The cell structure of β -FeSi₂ crystal[133, 134]. The purple spheres are Fe ions, and the green spheres are Si ions.

Besides, β -FeSi₂ can be used in thermoelectric devices due to its large Seebeck coefficient and relatively high oxidation resistivity[11, 135-137]. The lattice structure of β -FeSi₂ is shown in Figure 4.1[133]. The purple balls represent Fe, and the green balls represent Si.

β -FeSi₂ is composed of two non-toxic elements, Fe and Si, which numerous exist on earth, making β -FeSi₂ a cost-effective material for industry. Throughout decades, various methods were carried out by scientists to synthesize β -FeSi₂, such as mechanical alloying[138], ion implantation[139], sputtering[130, 140], thermal annealing[141], and chemical vapor transport method[142]. In this work, gas-phase synthesis is employed to produce β -FeSi₂.

4.2 Synthesis setup and mechanism

Gas-phase synthesis of the β -FeSi₂ NPs was previously proposed by Kameyama in 1993[143]

using a radio frequency coupled plasma torch system. According to Kametama, silane (SiH_4) and iron pentacarbonyl ($\text{Fe}(\text{CO})_5$) are employed as precursors. These two precursors decompose and form the final $\beta\text{-FeSi}_2$ nanomaterials under a certain temperature, theoretically. However, in the real experiment, the materials produced are usually mixed compounds with iron silicides, such as Fe_5Si_3 , FeSi , $\beta\text{-FeSi}_2$, $\alpha\text{-Fe}$ and SiC . The production control, for example, the purity of a certain phase, cannot be guaranteed. According to the iron-silicon phase diagram (Figure 4.2), various compounds can be formed, such as Fe_2Si , Fe_5Si_3 , FeSi , $\alpha\text{-FeSi}_2$ and $\beta\text{-FeSi}_2$ [144].

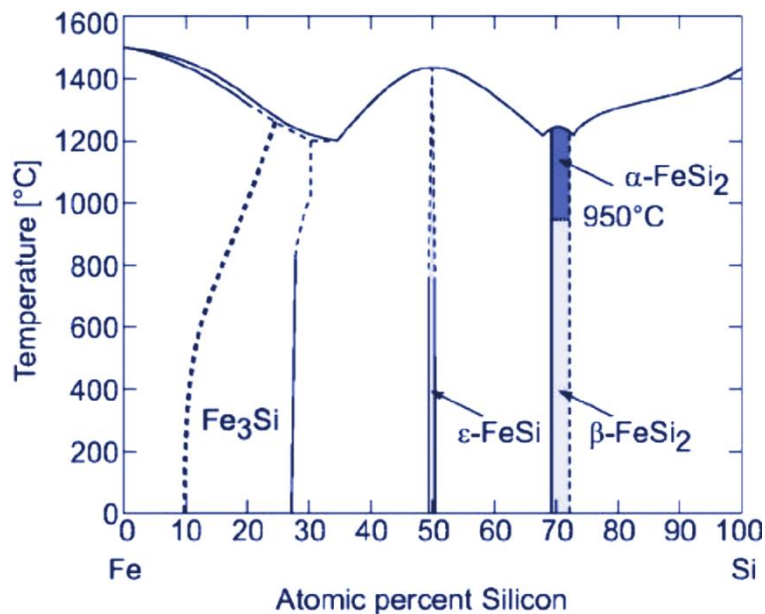


Figure 4.2 The Fe-Si binary phase diagram[145].

Iron disilicide is formed by the decomposition of two precursors, iron pentacarbonyl ($\text{Fe}(\text{CO})_5$) and silane (SiH_4). The whole gas-phase synthesis system is composed of a gas delivery pipeline, hot-wall reactor, and particle collecting tube (Figure 4.3).

Precursors go through the pipeline to the hot-wall-reactor at a mass flow controlled by flow controllers. A bottle filled with $\text{Fe}(\text{CO})_5$ (99%, Sigma-Aldrich) is located inside the thermalized bubbler equipment, and $\text{Fe}(\text{CO})_5$ is carried by nitrogen flow (99.999%, Air Liquide). Besides, SiH_4 mixed with argon (UHP, Air Liquide) in a ratio of 1: 9 is employed.

Notably, the vapor pressure of iron pentacarbonyl (IPC) increases with the rising temperature, and the pressure influences the flow of iron pentacarbonyl. In this case, the temperature is maintained at 22°C inside the thermalized bubbler equipment to deliver the needed amount of iron pentacarbonyl (IPC). The mass flow of the IPC together with the carrying gas nitrogen is 200 SCCM.

Before the synthesis of $\beta\text{-FeSi}_2$, nitrogen gas is pumped down and refilled several times to ensure that the oxygen concentration inside the tube is below 0.03%. The oxygen concentration is tested with an oxygen flow sensor at the end of the tube. When the synthesis starts, the valve of silane is turned on first, and then the valve for $\text{Fe}(\text{CO})_5$. The stoichiometric ratio of Si to Fe is 2.6:1[146], indicating the amount of Si is a little bit excessive, and pressure inside the tube is maintained around 500 mbar. Meanwhile, the reaction temperature stays at 620°C (900 K). The experiment undergoes around 2.5 hours and produces 7.04 g $\beta\text{-FeSi}_2$, with a yield of 68.4%. The yield is calculated by the ratio of the produced $\beta\text{-FeSi}_2$ NPs to the consumed amount of $\text{Fe}(\text{CO})_5$ and SiH_4 .

The amount of the consumed precursors are calculated by the difference of the remaining amount in the precursor bottle before and after the reaction.

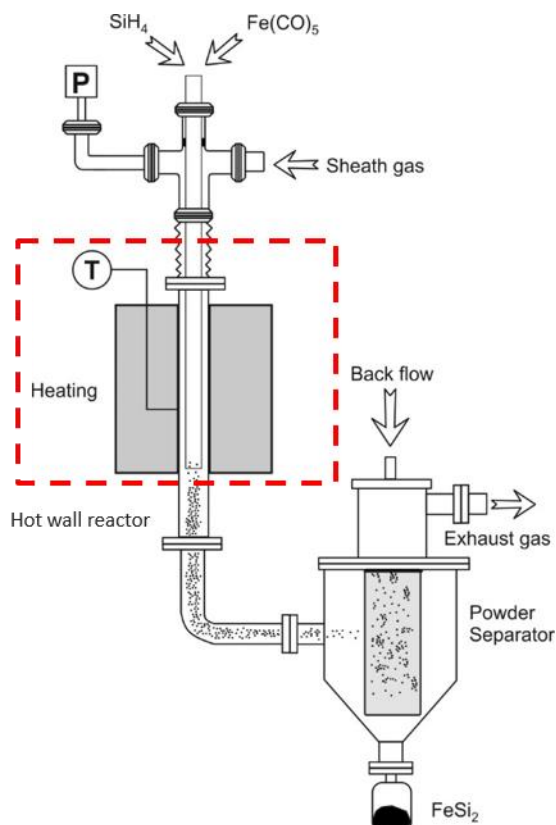
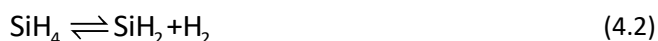


Figure 4.3 The hot-wall reactor for the direct gas-phase synthesis of β -FeSi₂, including the gas delivery pipelines (top), the hot-wall reactor (middle), and a particle collecting tube with the powder separator and the particles collecting bottle (right-down). Dr. Hans Orthner provides this graph.

In the synthesis of β -FeSi₂, an optimized gas-phase synthesis method[146] is employed, enabling large quantity and pure phase production. To produce pure β -FeSi₂, the partial pressure of the two precursors inside the reaction tube, the pressure and the temperature inside the reactor, and the ratio of these two precursors are the critical factors needed to be fixed. Based on a previous study by Petersen, E.L in 2003[147], the chemical reaction formulas of the decomposition of the precursors are shown from Equation 4.1 to Equation 4.11.

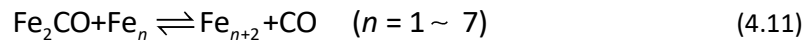
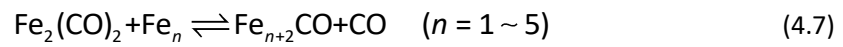
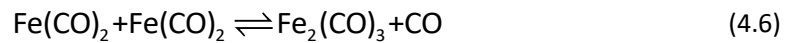
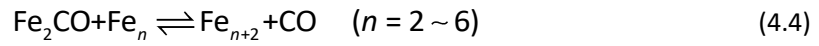


In this equation, M is the bath gas. In this case, Argon works as the third-body impact partner that carries silane. When the reactor's pressure is less than 1 atm (especiall in quite diluted system) and the bath gas during the decomposition process doesn't react, the decomposition of silane can be written in the following equation 4.2.



The decomposition of iron pentacarbonyl is much more complicated than the decomposition of silane. When Fe(CO)₅ decomposes at a temperature of 705 K and a pressure of 0.35 atm[148], a

series of reactions take place. To begin with, $\text{Fe}(\text{CO})_5$ is decomposed to $\text{Fe}(\text{CO})_2$. Then, $\text{Fe}(\text{CO})_2$ works as intermediates, continues to react and produces elemental Fe in the end. The main reactions are listed in Equation 4.3 to Equation 4.11[146, 149].



A previous study by Wen, J.Z in 2007[149] also suggests that under the temperature of around 900 K, iron carbonyls $\text{Fe}(\text{CO})_n$ decomposes so fast that $\text{Fe}(\text{CO})_5$ decomposes into Fe and CO rapidly. Under such a situation, the $\text{Fe}(\text{CO})_2$ reactions (from Equation 4.3 to Equation 4.11) can be neglected.

5 Capacitor Assembly and Electrical Measurement

Equipment

In this chapter, different capacitor assembly methods are employed to assemble the interdigitated structure and the parallel structure, aiming at enhancing the reproducibility of the capacitors' electrical performance.

5.1 Interdigitated structure capacitor

The microscope photo of the mask is shown in Figure 5.1. According to the scalebar in the image, the interdigitated electrode's overall size is $1.96 \mu\text{m} \times 1.96 \mu\text{m}$.

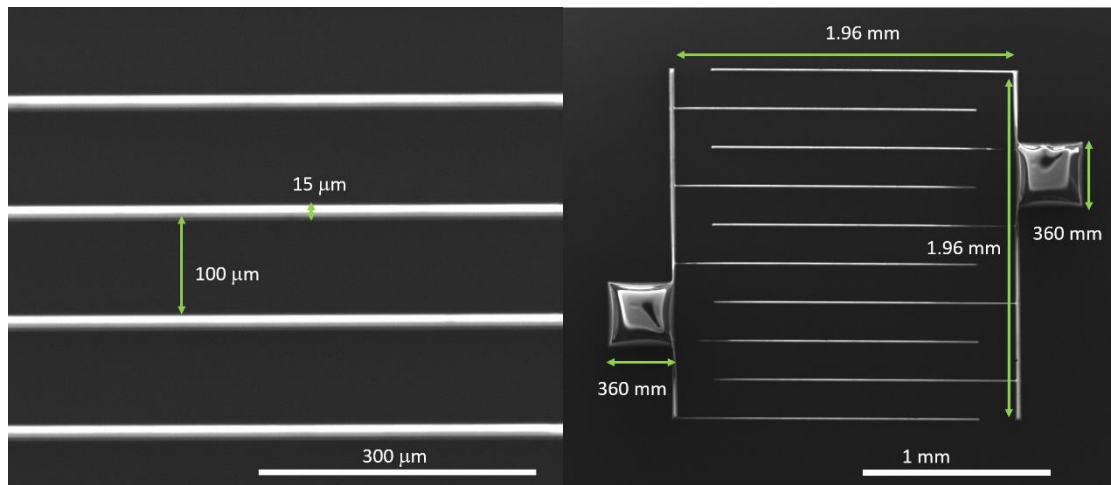


Figure 5.1 The structure of Cr coated photomask and the standard size of the pattern. The dark area is the area coated with Cr, and the light area is the transparent quartz substrate, with no Cr covered.

The assembly process of the interdigitated capacitors can be divided into several steps:

- 1) the formation of the interdigitated pattern on silica substrate using optical lithography,
- 2) the formation of the gold electrode via metal evaporation,
- 3) the connection of the interdigitated electrode to the chip carrier, bonded with $\text{Al}_{0.99}\text{Si}$ wire,
- 4) and last, the formation of the interdigitated electrodes by the spin-coating of $\beta\text{-FeSi}_2$ NPs onto the surface.

The whole preparation process of the interdigitated micro capacitors assembly is conducted in the cleanroom. The configuration of the capacitor is shown in Figure 5.2. The golden color in Figure 5.2 represents that the interdigitated electrodes are positively charged. In contrast, the gray color means the interdigitated electrodes are negatively charged, i.e., the electrodes are connected

to the source meter's positive and negative contact, separately.

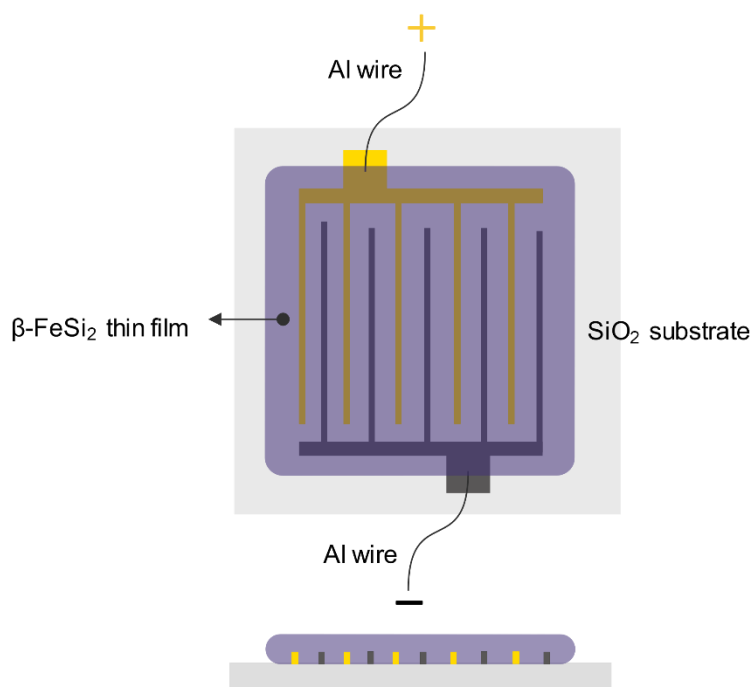


Figure 5.2 The interdigitated capacitor's schematic figure from Top view (top) and the side view (down). The golden color indicates that the interdigitated electrodes are positively charged, and the gray color indicates the electrodes are negatively charged.

Gold interdigitated structure in Figure 5.3 (a) is lithographically printed on a $4 \times 4 \text{ mm}^2$ silica substrate or a silicon substrate with an oxidation layer on top. The substrate is cleaned in acetone and isopropanol with an ultrasonic cleaner, and later on, dried with nitrogen. The positive photoresist (AZ1518, Microchemicals) is spin-coated onto the substrate's surface, with a rotating speed of 250 revolutions per minute (rpm) for 30 s. Later, the substrate with photoresist is baked on a hot plate at $100 \text{ }^\circ\text{C}$ for 60 – 65 s. Then the substrate with photoresist is exposed for 14 s in mask aligner with chromium mask. Afterwards, the substrate is dipped into a developer (AZ351B, Microchemicals) and subsequently in a stopper (deionized water). The exposed area will be dissolved in the developer AZ351B, producing an interdigitated structure on the substrate.

Au evaporation procedure is carried out in an evaporator. A thin film of 5 nm Ti and then a 50-nm-Au film are deposited on the surface. The 5-nm-Ti film is for increasing the adhesiveness of Au to the substrate. The liftoff procedure is done in hot acetone (around $70 \text{ }^\circ\text{C}$), which means that the Au layer on the photoresist exfoliates as the photoresist melts in hot acetone. At the same time, the other part remains on the surface. Thus the Au interdigitated structure is accomplished. Al wires are employed to bind the interdigitated structure to the chip carrier by the bonder machine.

The microscope photo of the gold interdigitated pattern on the silica substrate is shown in Figure 5.3 (a). The size of the interdigitated structure is $1.96 \text{ mm} \times 1.96 \text{ mm}$. There are 18 fingers (9 fingers for each electrode). The width of each finger is $20 \text{ }\mu\text{m}$, and the length 18 mm. The distance between two fingers is 10 mm.

A dispersion with $\beta\text{-FeSi}_2$ NPs in ethanol or deionized water with 10 mg/ml concentration is produced via ultrasonication. $6 \text{ }\mu\text{l}$ suspension (via a pipette) with $60 \text{ }\mu\text{l}$ $\beta\text{-FeSi}_2$ NPs in it is spin-

coated onto the as-prepared empty micro capacitor and dried in a ventilation hood. A interdigitated capacitor coated with β -FeSi₂ is produced, shown in Figure 5.3 (b).

To maintain the homogenous distribution of the β -FeSi₂ nanoparticles, different spin-coating rates (50 rpm, 250 rpm, 450 rpm, and 650 rpm) with the same amount of β -FeSi₂ dispersion (6 μ l) is carried out. It turns out that a rotation speed of 250 rpm is the best for the spin-coating process, because a speed of 50 rpm ruins the unity of the thin-film thickness, and the speed of 450 rpm and 650 rpm spin some β -FeSi₂ nanoparticles out of the substrate's surface.

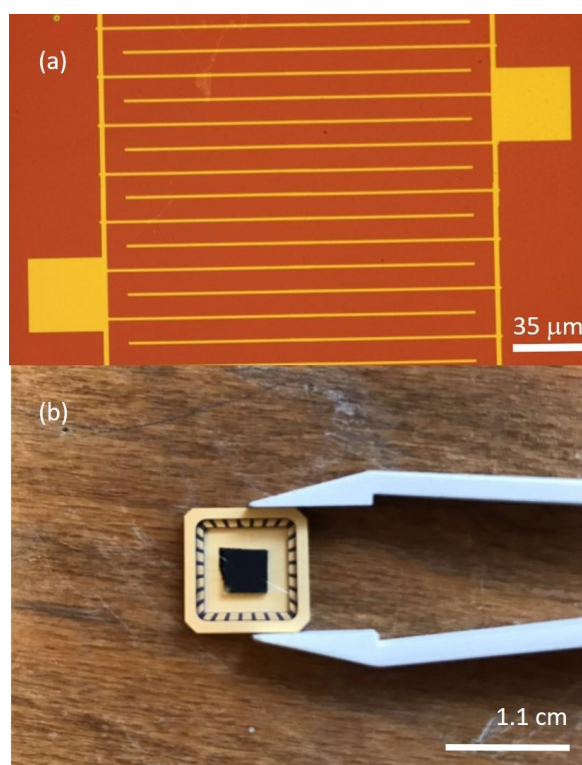


Figure 5.3 (a) A microscope image of the gold interdigitated structure on the silica substrate and (b) the photo of an assembled β -FeSi₂ micro capacitor.

5.2 Double-plate capacitor

Besides the interdigitated structure capacitor, the traditional parallel-plate capacitor is also produced for a reference study. A layer of a thickness of 50 nm Au is evaporated onto a quartz plate (3.8 cm \times 2.6 cm \times 1 mm), and 6 μ l β -FeSi₂ dispersion (10 mg/ml) is spin-coated on it. The diameter of the NPs coated area is around 0.75 cm. The thickness at the edge of the ink is thicker than the central part of the ink, as shown in Figure 5.8(left), a common situation called the coffee stain effect, due to the capillary flow caused by the evaporation of the drop. During the evaporation, the dispersed nanoparticles are carried to the edge by the liquid from the central area, causing the aggregation of nanoparticles on the edge[150]. Figure 5.4 (right) is the microscope photo of the β -FeSi₂ thin-film in Figure 6.13 (left) with a scale bar of 150 μ m.

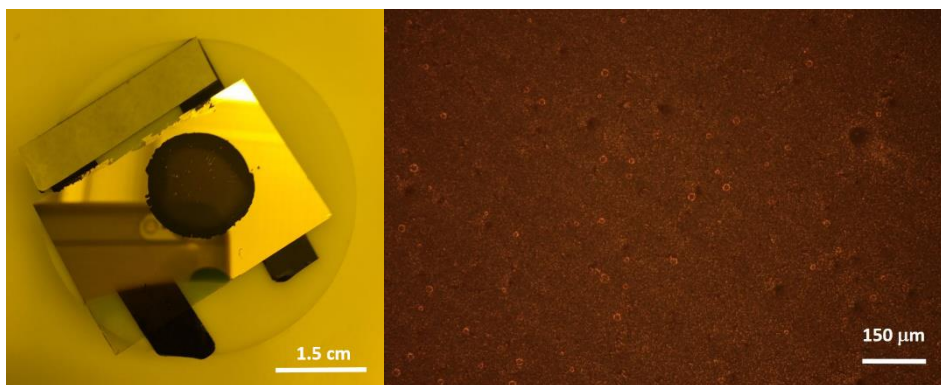


Figure 5.4 Parallel-plate quartz electrode coated with 50 nm Au layer, and then 60 μg $\beta\text{-FeSi}_2$ spin-coated on top (left). The microscope photo of $\beta\text{-FeSi}_2$ ink, magnified 10 times (right).

The conductive cables with the isolating coating layer are bonded with Silver glue to the Au surface (Figure 5.5). Afterwards a plate electrode is completed. The separator used here is the porous glass microfiber paper (GF/D CAT No. 1823-090, Whatman). The paper thickness is around 0.67 mm, and the pore size is about 2.7 μm . Two plate electrodes and the separator are assembled, as shown in Figure 5.5, forming a double-plate capacitor. Clips are needed to make sure the close contact of electrodes and separator. Before the test, the double-plate capacitor is placed in a sealed container saturated with water vapor for a longer time, typically 24 h. The electrode plate covers the other electrode, with a separator in between, making it harder for the nanoparticles to be infiltrated by water vapor in the air. Two or more clips are used to fix the position of these two electrodes, to maintain the stability of the structure of this double-plate capacitor (Figure 6.34).

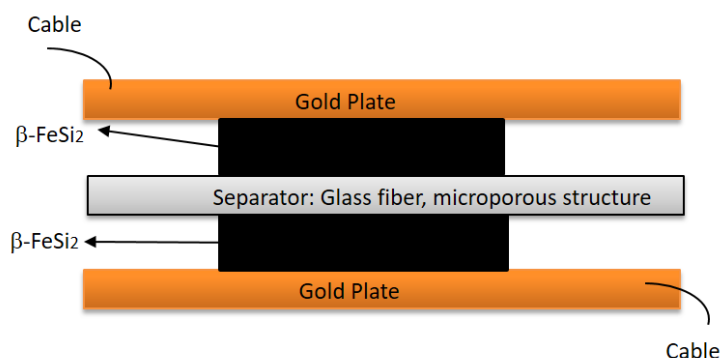


Figure 5.5 The double-plate capacitor configuration, with two double plates coated with gold as electrodes and a sheet of porous glass fiber as a separator.

5.3 The equipment of electrical measurement

The electric measurement (e.g., galvanostatic and potentiostatic test, cyclic voltammetry) setup (Figure 5.6) is composed of three parts, i.e., a container where the micro capacitor with $\beta\text{-FeSi}_2$ locates and is measured, a power supplier which provides the applied voltage/current, and a computer installed with LabVIEW (National Instrument) program. The machine is Source Measure Unit (SMU) Instruments Keithley's Series 2400. Keithley 2400 is used as a source meter, applying

voltage/current onto the sample and measuring the resistance, current, and voltage. The LabVIEW (National Instrument) program commands the Keithley 2400, computer, and humidity sensor (Arduino), records the real-time voltage/current, relative humidity, and temperature in TXT files. Data points are usually taken every 0.1 s. The relative humidity and temperature are measured with the humidity probe sensor plugged inside the container, measuring the real-time temperature and the real-time humidity.



Figure 5.6 The experimental setup configuration, with a sealed chamber where capacitors locate, a source measure unit that provides the voltage (current) and measures the output, and a computer that controls the whole setup with LabView software.

The micro capacitor β -FeSi₂ is measured in the air saturated water vapor to achieve the maximum stored charge. Before electric measurement starts, a beaker filled with deionized water and the micro capacitor with β -FeSi₂, is placed inside the container. The time-dependent relative humidity is measured to test how fast the relative humidity changes and the time needed to reach equilibrium status (Figure 5.6). The ambient temperature is 25 °C.

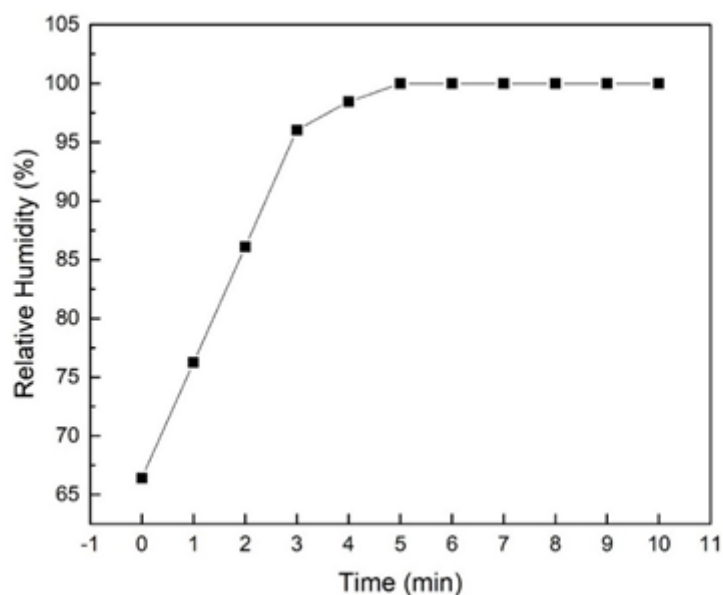


Figure 5.7 Relative humidity is measured in the sealed container, which varies along with the time and gets stable after a particular time. The real-time temperature is measured and recorded together with the relative humidity.

The container is first dried using silica gel to 16.9% RH. Then a beaker of deionized water is placed inside the chamber. The relative humidity increases immediately to 66.8% RH (at around

25 °C), at a speed of approximately 10% RH/min, and gets saturated after around an additional 5 min to nearly 100% RH (Figure 5.7).

To make sure that the nanoparticle film on the capacitor is thoroughly infiltrated with water vapor, usually, a longer time (several hours) is needed before the measurement starts. Notably, when the relative humidity is 100% RH (under ambient pressure and ambient temperature), the absolute humidity's corresponding value is 0.023 Kg/m³[151].

6 Result and Discussion

In this chapter, the successful synthesis of β -FeSi₂ is confirmed by the characterization results, including the scanning electron microscopy, X-ray diffraction, X-ray photoelectron spectroscopy, and the Brunauer-Emmett-Teller test. Besides, the electric performance of the interdigitated capacitors is shown through the potentiostatic test, the galvanostatic tests, and cyclic voltammetry. The stored charge is measured and calculated.

The function of β -FeSi₂ nanoparticles and water molecules on charge storage is checked. Considering the properties of β -FeSi₂ as semiconducting material, the semiconducting material's charge transfer behavior needs to be studied. A schematic model of the unit capacitor consisting of two adjacent nanoparticles is established, based on the working mechanism's analysis. Additionally, the capacitor's equivalent circuit is built, and a rough estimation of the capacitance is made.

Furthermore, the structure of the parallel double plate capacitor is tested. In this section, capacitors with β -FeSi₂ are tested to compare the capacitor structure's influence on charge storage ability. The capacitors with different nanomaterials such as SiO₂ and boron-doped Si (B-Si) are also tested to extend other materials' application on the capacitors. Different amounts of the additive polyacrylic acid (PAA) are mixed with the β -FeSi₂ nanoparticles to determine whether binders can improve the capacitors' electrical. We investigate which ratio of PAA leads to the best electrical performance. Meanwhile, the mass-dependent stored charge relationship is tested.

6.1 Characterization of β -FeSi₂

6.1.1 Scanning electron microscope

The scanning electron spectroscopy of as-synthesized β -FeSi₂ nanoparticles is shown in Figure 6.1. The scale bar shown in the graph is 500 nm. The figure shows that the β -FeSi₂ nanoparticles have the shape of a sponge. A rough idea regarding the nanoparticles' size (in the scale of tens of nanometers) can be achieved with this graph. According to Figure 6.1, the diameter of a single nanoparticle ranges from 20 – 60 nm.

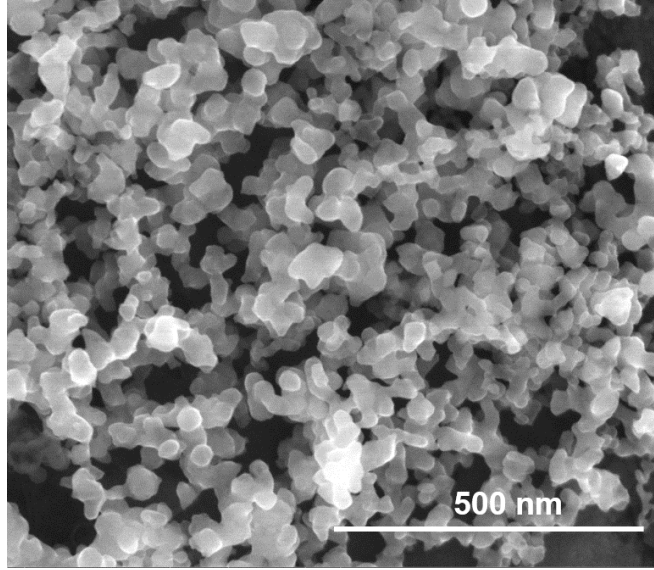


Figure 6.1 Scanning electron spectroscopy of as-synthesized β -FeSi₂ nanoparticles, the scale bar is 500 nm. The figure shows that the β -FeSi₂ nanoparticles have a sponge-like shape. The rough size of the nanoparticles (in the scale of tens of nanometers) can be thus estimated.

Two hundred fifty particles are employed to complete particle distribution analysis[152]. The nanoparticle size distribution closely fits with a log-normal distribution relation, and according to equation 6.1 below,

$$x_g = (\prod x_i)^{1/N} \quad (6.1)$$

N is the total number of calculated nanoparticles. In this case, 250 particles are involved in this calculation. x_i is the size for a single particle. The calculated geometric mean diameter of 250 particles is 35.3 nm.

Particle distributions are often lognormal distributed, the lognormal equation is shown in Equation 6.2[153].

$$F(x) = \frac{1}{\sqrt{2\pi x \ln \sigma_g}} e^{-\left[\frac{(\ln x - \ln CMD)^2}{2(\ln \sigma_g)^2} \right]} \quad (6.2)$$

σ_g is the geometric standard deviation characterizing the diversity of nanoparticle size. CMD is the count median diameter. There are 50% of the particles that are larger/smaller than CMD.

Through the histogram with size distribution, the geometric standard deviation σ_g and CMD are achieved (Figure 6.2). The calculated σ_g is 1.27, based on, which means the nanoparticle size is narrowly distributed. The Count median diameter is 34.5 nm.

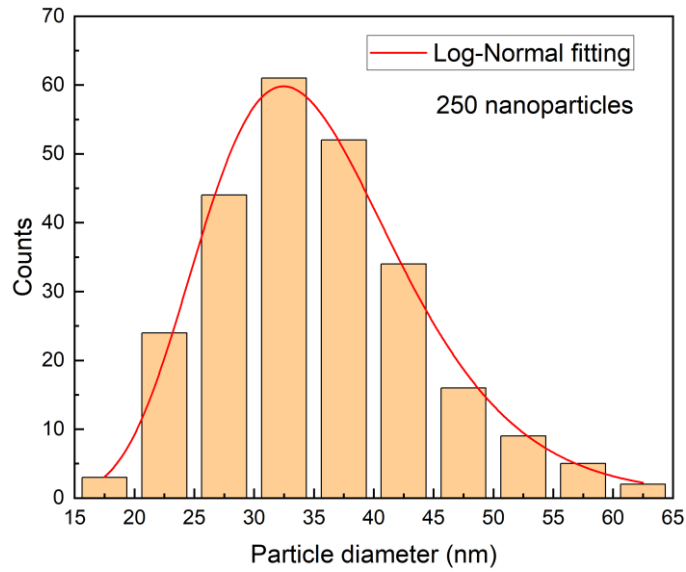


Figure 6.2 Histogram with size distribution. The particle distribution analysis achieved from the SEM spectroscopy, showing that the particle size distribution of the β -FeSi₂ nanoparticles conforms to the law of log-normal distribution, and the particle size distributes from 20 nm to 70 nm, with the most considerable portion of the β -FeSi₂ NPs' size ranging between 25 nm and 50 nm.

6.1.2 X-ray diffraction

The X-ray diffraction measurement of the as-synthesized β -FeSi₂ powder is applied with Cu-K α X-ray radiation source. And the x-ray tube voltage (Cu K α radiation) is 40 kV, and the working current is 40 mA. The scan angle 2θ ranges from 15° to 95°, with a scan rate of 8 °/min and a step size of 0.02°. θ is the angle formed by the incident waves and the crystal plane in Figure 3.14.

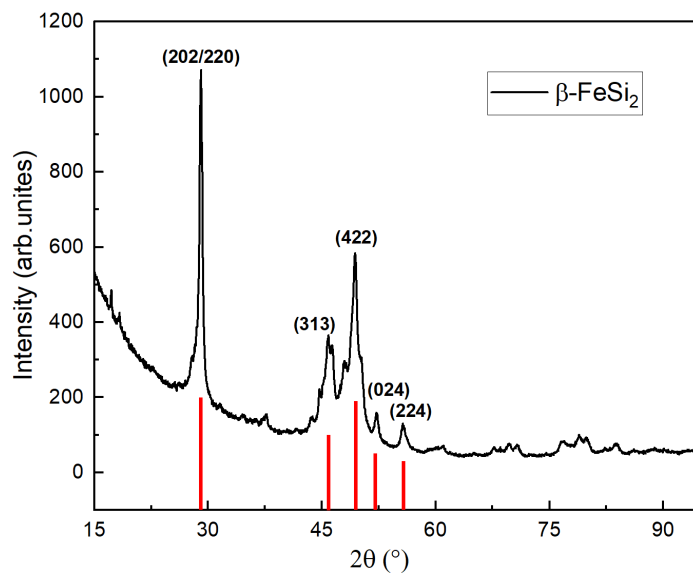


Figure 6.3 The X-ray diffraction pattern of the as-synthesized NPs with the typical characteristic peaks of β -FeSi₂ NPs noted as (202/220)(313)(422)(024)(224), proves that β -FeSi₂ NPs can be successfully synthesized at a SiH₄: Fe(CO)₅ ratio of 2.6:1.

XRD pattern (Figure 6.3) shows that the peaks of produced nanoparticles are perfectly aligned with the characteristic peaks of β -FeSi₂ in the literature[146]. The sharp peak shape indicates the crystalline structure of the β -FeSi₂ nanoparticles. According to the Scherrer formula, the size of the nanoparticles can be roughly estimated (Equation 6.3).

$$\beta = \frac{K \cdot \lambda}{D \cos \theta} \quad (6.3)$$

β is the full-width, half-maximum of the intensity(FWHM), θ is the Bragg angle, K is the shape factor that varies with the shape of the crystallites, and for spherical crystals, it is usually in the value of 0.89[154]. λ is the wavelength of X-ray, which is 0.154 nm in this case (the average value of $\kappa_{\alpha 1}$ and $\kappa_{\alpha 2}$), while D is the mean size of crystallite. Taking the peak at 29.06°, the β is 0.0094 rad. Hence the calculated D according to Equation 6.3 is 15.2 nm, smaller than the calculated size of the SEM result. The significant deviation at the particle size analysis is caused by the severe XRD peak broadening issue[155], when the Scherrer formula is used to calculate the particle size less than 100nm.

6.1.3 X-ray photoelectron spectroscopy

In this work, XPS is used to characterize the near-surface chemical status of the as-prepared β -FeSi₂ nanoparticles. The black line is the measured XPS spectrum, the green, yellow, purple, blue, and light blue lines are the fitted composites (Figure 6.4). The red line is the sum of all the above-fitted lines. It shows the surface composite includes β -FeSi₂, SiO₂, and elemental Si. The peak at high binding energy (around 103 eV) corresponds to the Si_{2p} photoelectrons emitted from Si bound to oxygen. The peak at a lower binding energy of approximately 99 eV to 100 eV corresponds to the Si_{2p} photoelectrons emitted from Si bound to FeSi₂. It needs to be noticed that the small peaks between these two peaks (from around 100.5 eV to 102 eV) are due to the transition compounds of SiO_y (0<y<2) [156].

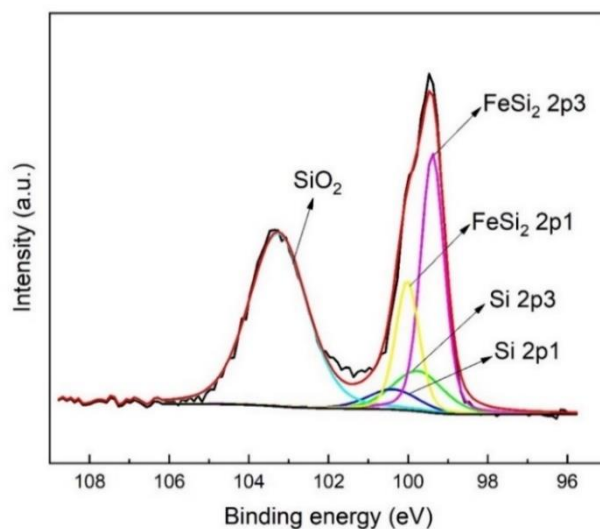


Figure 6.4 The experimental (black) and fitted (red) X-ray photoelectron spectrum of Si. The peaks of the experimental spectrum of β -FeSi₂ NPs can be divided and fitted into the peaks of SiO₂, FeSi₂, and elemental Si.

The measured and fitted X-ray photoelectron spectrum of O are shown in Figure 6.5, as supplementary. The spectrum indicates that almost all O (green line) exist in the form of SiO₂. There is a small peak (blue line) at 531 eV, which is the binding energy of C=O in residual carbon dioxide on the surface.

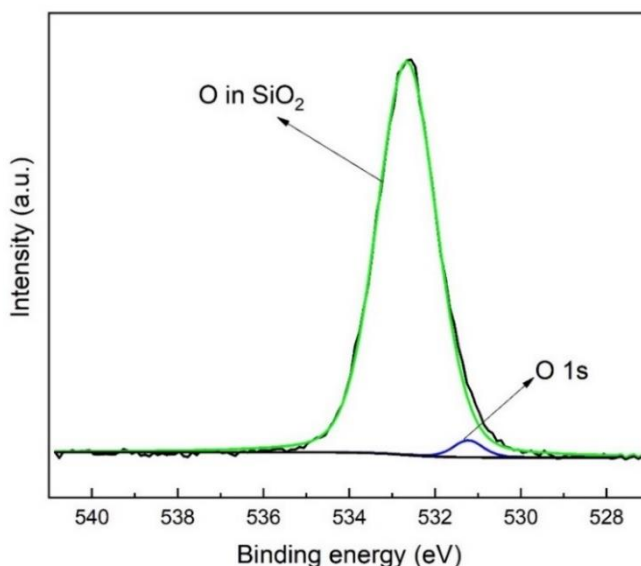


Figure 6.5 The experimental (black) and the fitted (blue and green) X-ray photoelectron spectrum of oxygen.

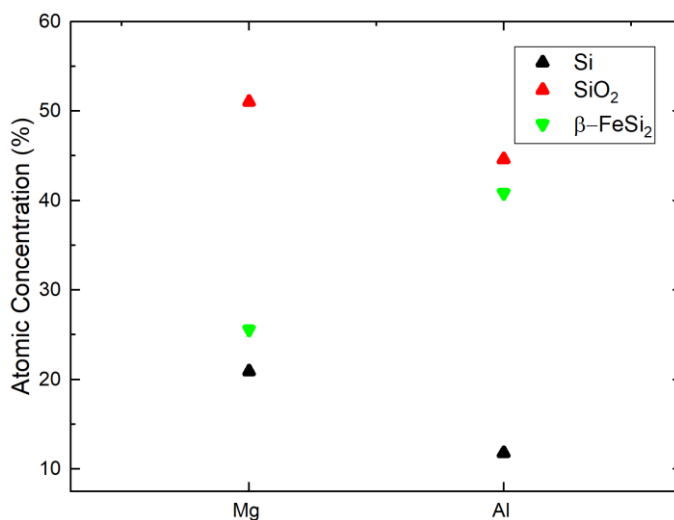


Figure 6.6 The X-ray Photoelectron Spectroscopy of β -FeSi₂ NPs, measured with Al K α X-rays and Mg K α X-rays, respectively, proving the core-shell structure of the β -FeSi₂ NPs, with a thin layer of Si/SiO₂ covering the β -FeSi₂ sphere NPs.

Al K α X-ray (1486.7 eV) and Mg K α X-ray (1253.6 eV) are employed in the measurement to characterize β -FeSi₂ nanoparticles. E_{photon} of Al K α X-ray is larger than Mg K α X-ray. The inelastic mean free path means how far on average an electron can travel through solid before losing any energy. According to the inelastic mean free path curve shown in Figure 6.7, the photoelectron excited by Al K α X-ray has larger kinetic energy than that of Mg K α X-ray. It means that Al K α X-ray measurement provides more information regarding the deeper part of the nanoparticle than the measurement carried out with Mg K α X-ray does.

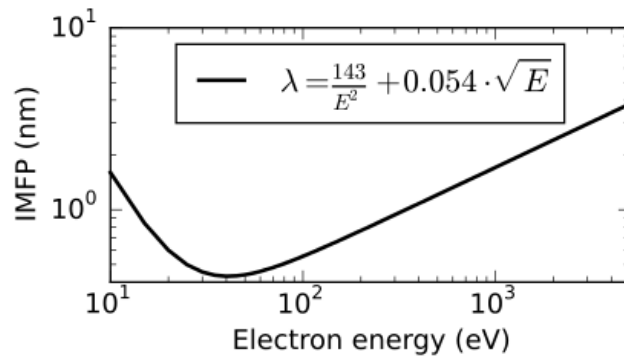


Figure 6.7 The inelastic mean free path (IMFP) curve of electrons in elements as a function of excited electron energy[157].

According to Figure 6.6 and Figure 6.7, the atomic concentration of SiO₂ and Si measured with Al K α X-ray is lower than that measured with Mg K α X-ray, which means that SiO₂ is mainly covering the surface. β -FeSi₂ mainly aggregates in the core, rather than the surface, indicating that the β -FeSi₂ nanoparticle is a core-shell structure, surrounded by SiO₂ and Si as the shell. The existence of SiO₂ is caused by the oxidation of Si when the β -FeSi₂ powder is stored in a glass bottle filled with air.

6.1.4 Brunauer-Emmett-Teller test

According to Brunauer-Emmett-Teller (BET), the specific surface area of β -FeSi₂ nanoparticles is around 32.9 m²/g.

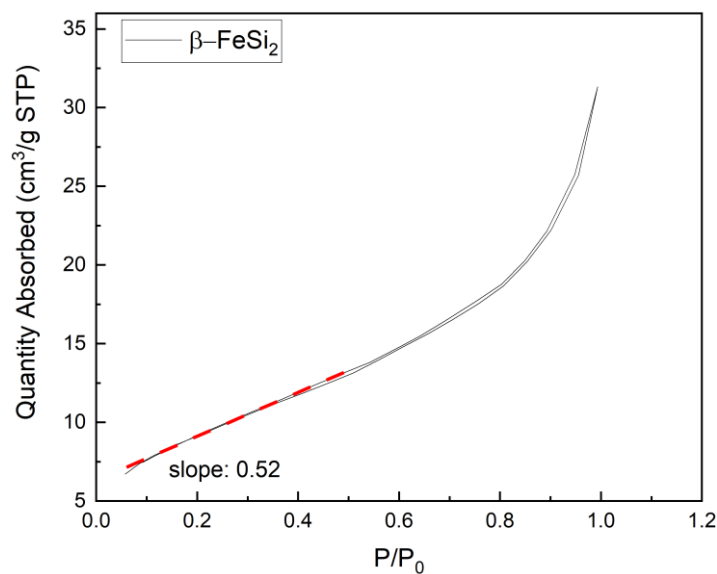


Figure 6.8 The adsorption isotherm plot of β -FeSi₂ NPs, showing that the β -FeSi₂ nanoparticles are non-porous nanomaterials.

Based on the adsorption isotherm theory of BDDT (established by Brunauer, Deming, Deming, and Teller, adsorption isotherms were categorized into five types), the adsorption isotherm plot of β -FeSi₂ is classified as Type III[158, 159]. It indicates that β -FeSi₂ is a non-porous particle. The low-

pressure regime slope is smaller than 1, suggesting that the tested nitrogen molecule has a weak adsorbate-adsorbent interaction (Figure 6.8).

6.2 Preliminary analysis of the electrical performance on the interdigitated capacitor

6.2.1 Mass control of the β -FeSi₂

To maintain the electric measurement's reproducibility afterward and to find out the optimal thickness of the β -FeSi₂ layer (neither too thick nor too thin), the mass and thickness control of the deposited β -FeSi₂ NPs thin-film is carried out. And the thickness of at different positions A (Center), B (Half center), C (Near edge) in Figure 6.9 is measured via the focused ion beam (FIBs).

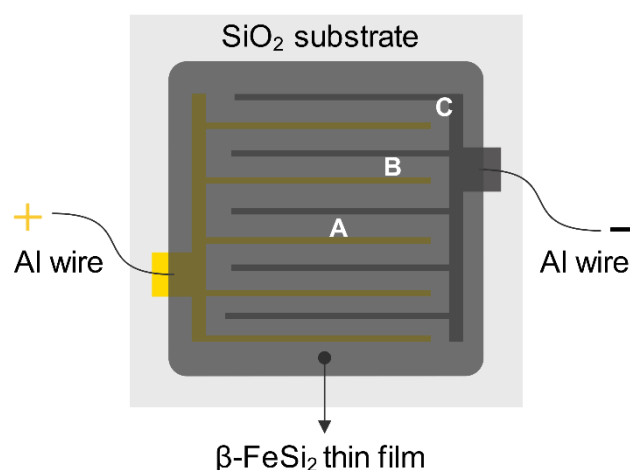


Figure 6.9 The schematic drawing of tested spots on the micro capacitor, A (center), B (half center), and C (near the edge).

FIBs are employed to sputter the ions out of the surface, etching the nanoparticles and some part of the silica substrate. In other words, FIB can be applied to dig a hole into the nanoparticle thin film. By checking the cross-section height, the thin film's thickness is measured through the measuring function of FIBs. The cross-section SEM photo of the cut β -FeSi₂ film on SiO₂ substrate is shown in Figure 6.10(b). The sample plate is slightly tilted so that the cross-section of nanoparticle thin film and SiO₂ substrate can be observed clearly. The thickness is measured after considering the tilted angle. According to Figure 6.10(b), the loosely stacked nanoparticles on top are β -FeSi₂, and the condensed and dark part is the silica substrate. The boundary is quite clear, measuring the thickness of β -FeSi₂ film feasible. Figure 6.10(a) is the SEM photo of β -FeSi₂ thin film from the top view.

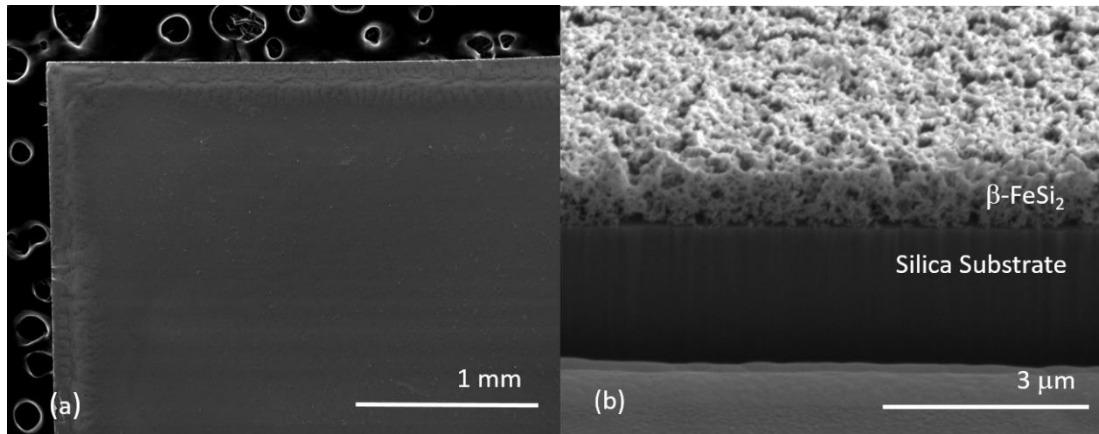


Figure 6.10 The top view SEM graph of the micro capacitor (a) and the cross-section SEM graph (b) of β -FeSi₂ nanoparticle thin film on the interdigitated structure. The darker part in (b) is the Si substrate.

Different amount of β -FeSi₂ nanoparticle dispersions are spin-coated at a rotation speed of 250 rpm onto the top of substrate, i.e., 2 μ l (20 μ g β -FeSi₂), 4 μ l (40 μ g β -FeSi₂), 6 μ l (60 μ g β -FeSi₂), and 8 μ l (80 μ g β -FeSi₂). Again, film thickness measurement is carried out on Position A, B, and C (Figure 6.9). Unfortunately, the thickness of the β -FeSi₂ thin film in 20 μ g sample is too thin to detect. For a mass loading of 80 μ g, the thickness of β -FeSi₂ thin film on edge is too thick to detect. The tilting angle of the sample is not big enough, the edge of the NPs thin films and Si substrate cannot be observed.

The correlation between the loading mass (40 μ g, 60 μ g, and 80 μ g) and the thickness on different positions (A, B, and C) are shown in Figure 6.11. Also, because of the coffee ring effect, the thickness of position B (Half center) is slightly larger than position A (Center). While the thickness of position C (Near edge) is much bigger than that in the center. The thickness of position C (Near edge) of 80 μ g is too big to be measured. Fortunately, because the gold interdigitated pattern is within the range of position A and position B in Figure 6.9, the highly increased thickness of the nanoparticles on the edges can be neglected.

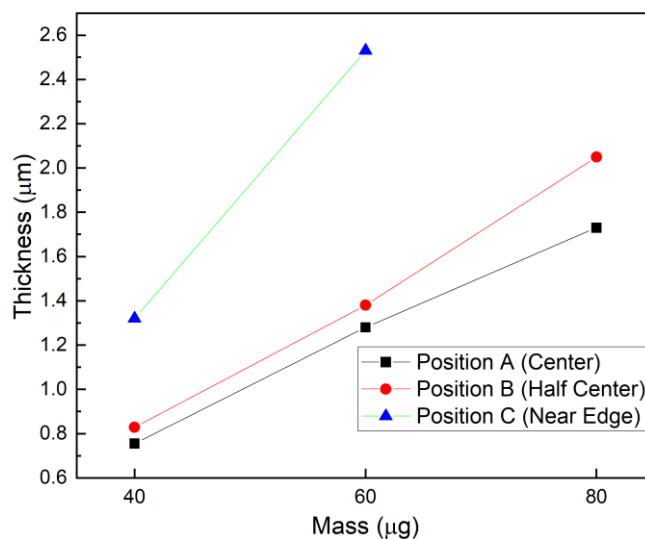


Figure 6.11 The loading mass of β -FeSi₂ dependent thin-film thickness at different positions A, B, and C follows a linear correlation.

The thickness at position A and position B at different loading mass is linearly correlated, indicating the positive correlation between the mass and its thickness. The average thickness is plotted in Figure 6.12.

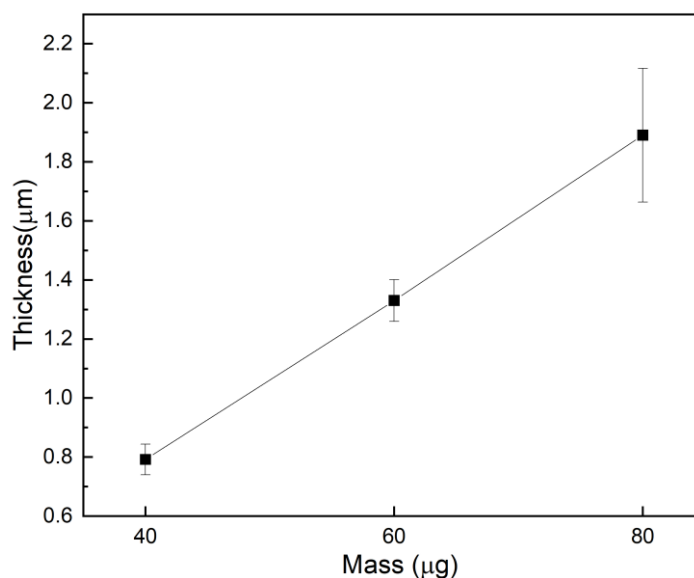


Figure 6.12 The arithmetic mean value of the thickness (at the same position spot A/B of the thin-film) of different β -FeSi₂ loading mass (40 μg, 60 μg and 80 μg), indicating a positive linear correlation. The average thickness of multiple capacitors achieves the data, the error bar shows the variability of data.

The porosity of the β -FeSi₂ thin film coated on the substrate is also an important parameter that should be noticed because the gaps between nanoparticles are the place where the water vapor stays and forms the electric double layer during the charging and discharging process. Besides, the looseness of the stacked nanoparticles provides easier access for the water molecules to the nanoparticles underneath.

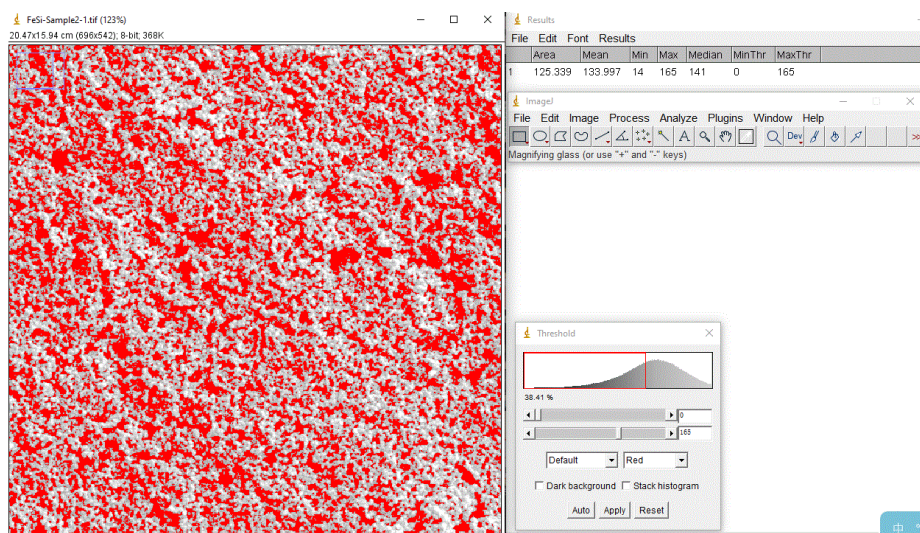


Figure 6.13 The porosity of β -FeSi₂ thin-film coated on the substrate, calculated with ImageJ. The red area represents the gaps between nanoparticles, and the gray areas are the nanoparticles.

Using the ImageJ software (Figure 6.13), the top-view porosity is roughly calculated by calculating the red area (representing gaps between nanoparticles) percentage over the whole area. The top-view porosity of β -FeSi₂ thin-film is estimated to be around 44.4%, based on the 2D SEM image. The cross-section view porosity is 48.1%, which is more or less similar to 44.4%. This relatively high porosity of the β -FeSi₂ thin film provides abundant space to keep water molecules, which is beneficial for charge storage.

6.2.2 Cyclic voltammetry

The cyclic Voltammetry (CV) is employed to determine the electrochemical reaction taking place during the charging and discharging process (Figure 6.14). The measurement is carried out under the same condition as the previous test (water vapor, \sim 100% RH), with Keithley 2400 on β -FeSi₂ interdigitated capacitor. The scanning voltage range is from 0 V to 3 V. The scanning rate is 0.1 mV/s.

According to the CV plot, no reduction peaks are observed, the curve is flat below around 1.7 V, and rises sharply after 2 V. The shape is quite similar to the shape of the oxygen evolution reaction of electrocatalyst, considering there is only water and β -FeSi₂ nanoparticles, the possibility of water electrolysis is taken into consideration. And further electrocatalyst measurement is carried out to figure out whether the β -FeSi₂ nanoparticles can split water in Appendix 11.1 [160].

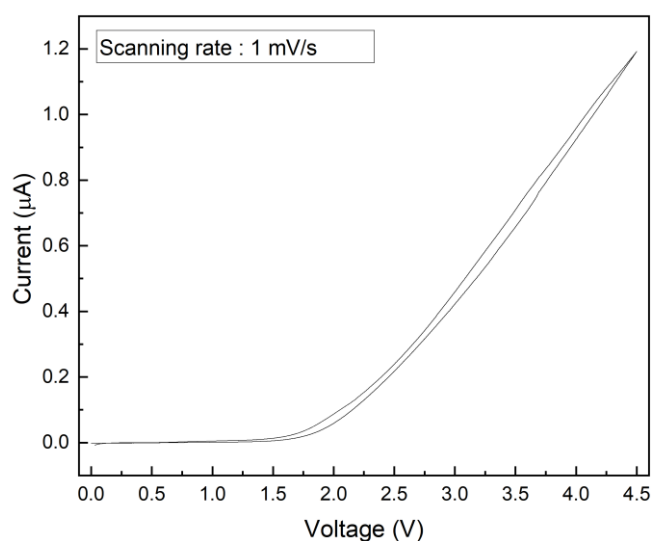


Figure 6.14 The cyclic voltammetry plot of the β -FeSi₂ capacitor, measured at a scanning rate of 1 mV/s, from 0 V to 4.5 V.

6.2.3 Potentiostatic measurement

As stated previously in Section 5.3, the micro capacitor coated with β -FeSi₂ is placed in a sealed container filled with air saturated water vapor for 12 h. Later the potentiostatic measurement is conducted with a source meter (Keithley 2400) to achieve voltage-dependent stored charge, i.e., voltage-dependent rate performance.

During potentiostatic measurement, a specific voltage is applied onto the micro capacitor for 120 s (i.e., charging process), and then the circuit is a shortcut (0 V) for 300 s (i.e., discharging process). One hundred twenty seconds of charging and 300 seconds of discharging is long enough for the current to reach a steady plateau (the current gets stable), which means the capacitor is fully charged and discharged. The applied voltage increases from 0 V to 3 V, each step width is 0.1 V. The whole process takes about 3.5 h. The current - time transient, i.e., $I(t)$ -curve, at different voltage is shown in Figure 6.15. To have a clearer view of the plots, the charging voltage step width in Figure 6.15 is 0.2 V.

When a particular voltage is applied, the measured transient current decreases in an exponential mode becomes steady in 120 s. In Figure 6.15, the ending current of the charging process increases along with the applied current. While for the discharging process, transient current also shows an exponential behavior. After 300 s, the discharge current is below $10^{-3} \mu\text{A}$, which is only 0.67% of the starting charging current of $0.15 \mu\text{A}$ at 3 V, indicating the capacitor is fully discharged.

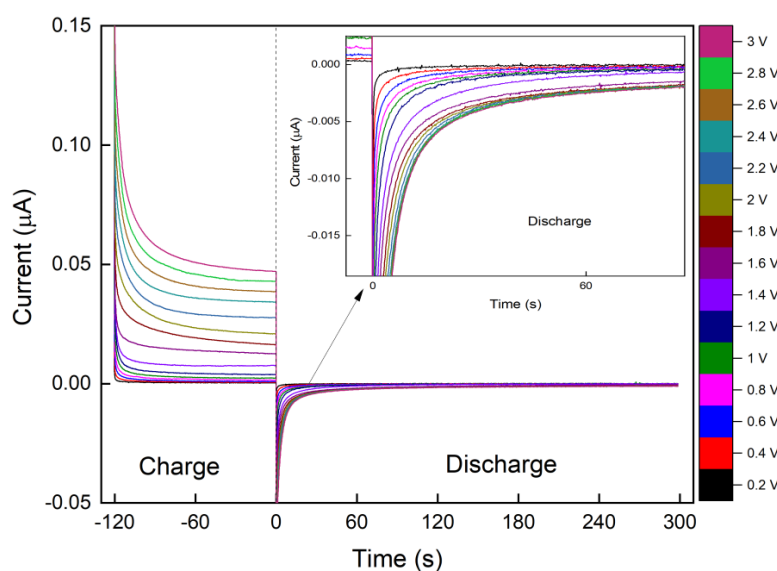


Figure 6.15 Typical $I(t)$ curve of $\beta\text{-FeSi}_2$ nanoparticle film in the charge and discharge process. The applied charging voltage ranges from 0.2 V to 3 V. The color scale on the right side indicates that different colors correspond to varying voltages in the figure.

The colors of the discharging plots are consistent with the colors of the charging plots. The zoom-in discharge graph (right-top) in Figure 6.15 shows that the discharging current plots first increase with the increasing charging voltage dramatically. However, after a specific applied voltage (around 2 V), the discharge transients' value has a much smaller change than before and almost overlap with each other, unlike the charging current plots that increase with the applied voltage.

The stored charge Q (μAs or μC) is achieved by integrating the shadowed area of discharge transient current plot over time (Figure 6.16), based on Equation 6.4.

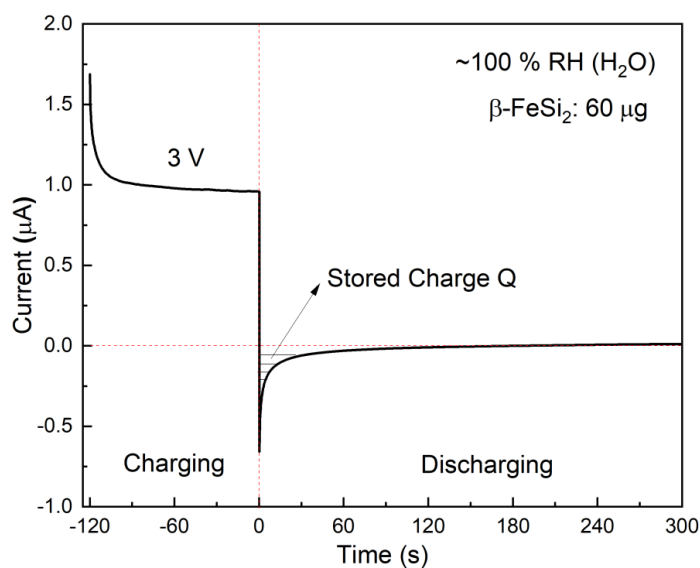


Figure 6.16 Typical $I(t)$ curve of β -FeSi₂ nanoparticle film in the charging (3 V) and discharging process, under 100%RH of water vapor in the tested atmosphere. The area of the region filled with a dashed horizontal line is the stored charge.

The baseline for the integration is the average current value of the last 50 data points of the current transient, rather than 0 μA , which is due to the equipment's measurement error. The specific charge (As/g or C/g) can also be employed as an essential index to characterize the capacitors' electrical performance.

$$Q = \int I dt \quad (6.4)$$

The integrating area of discharge transient at different charging voltage (0.1 V – 3 V) is calculated and plotted versus the applied voltage in Figure 6.17 (red line). Thus the stored charge-applied charging voltage (Q-V) plot of β -FeSi₂ micro capacitor is achieved. In Figure 6.17, the Q-V plot shows different behavior in different voltage range. From 0.1 V – 1.4 V, the plot shows a linear correlation. While from 1.5 V to around 1.9 V, a steep increase of charge takes place. Above 2 V, this increasing trend slows down, and the charge gets saturated after 2.5 V. The maximum capacitance of the interdigitated capacitor with β -FeSi₂ nanoparticles is around 0.4 μF .

As a reference, an interdigitated capacitor without β -FeSi₂ nanoparticles is also measured under the same condition, and the voltage-dependent stored charge plot is shown in Figure 6.17 (black line). The charge of the empty capacitor (no β -FeSi₂) is 2.4% of the charge of a capacitor with 60 μg β -FeSi₂ (regardless of lost particles during the spinning coating) at 3 V, showing the β -FeSi₂ nanoparticles contribute most of the charge.

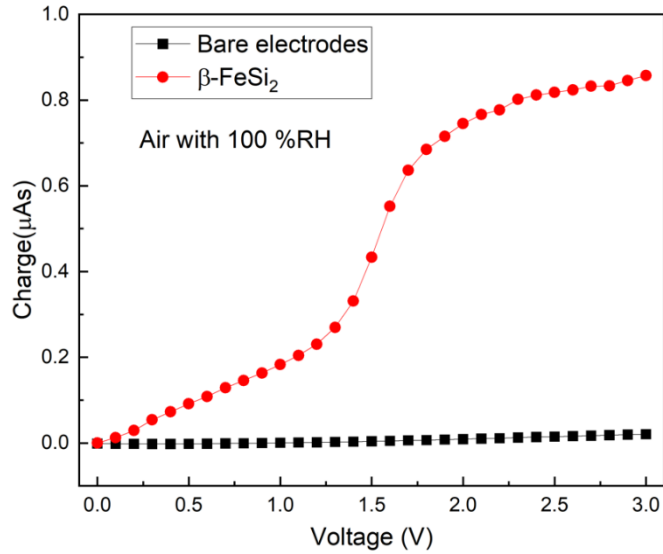


Figure 6.17 Redline: Stored charge-applied charging voltage (Q-V) plot of β -FeSi₂ micro capacitor at different charging voltage (0.1 V – 3 V). Blackline: Stored charge – applied charging voltage (Q-V) plot of the bare electrode without NPs under the same condition (100% RH of water vapor)

Besides, to verify the function of water vapor in the charge and discharge process, a reference test is carried out. A micro capacitor with β -FeSi₂ nanoparticles is tested in the air saturated with water vapor (100% RH) and dry air (3.9% RH). The voltage-dependent charge curves are plotted in Figure 6.18. The charge of the same capacitor under dry air is only 3% of the charge in the air saturated with water vapor, indicating water plays a significant role in this charge-storage process.

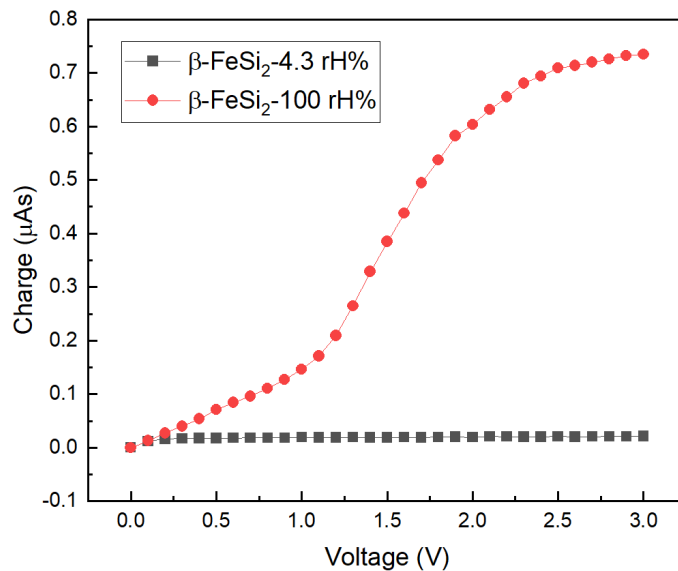


Figure 6.18 The stored charge of the capacitor measured in the air saturated with water vapor (black line) and in dry air (blue line), respectively, showing that the capacitance tested in the air saturated with water vapor is dramatically higher than in dry air.

Notably, the micro capacitors tested in Figure 6.17 and Figure 6.18 are different. Multiple capacitors are measured to make sure reproducibility. Identical capacitors are measured repeatedly

at other times to assure their robustness and stableness. In Figure 6.19, the interdigitated structure's cyclic performance at a charging voltage of 3 V is carried out. The cycle number is 140, and each cycle includes 2 min charging and 5 min discharging process.

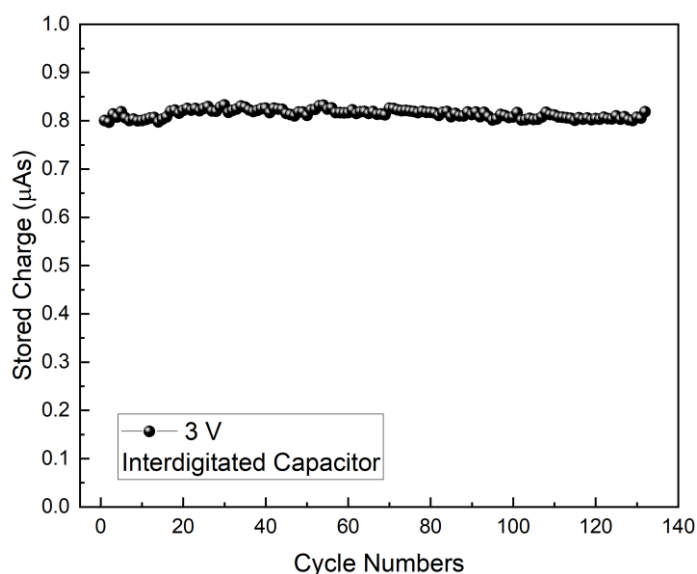


Figure 6.19 The interdigitated capacitor's cyclic performance with $\beta\text{-FeSi}_2$, at a charging voltage of 3 V, for 140 cycles, showing high retention of the capacitance.

According to Figure 6.19, the same capacitor's stored charge keeps more or less the same, even after 140 cycles, proving that the $\beta\text{-FeSi}_2$ interdigitated micro capacitor is a robust system.

6.2.4 Galvanostatic measurement

The galvanostatic test on the micro capacitors with $60\ \mu\text{g}\ \beta\text{-FeSi}_2$ is carried out to study the charging and discharging behavior from another angle. A current of $0.1\ \mu\text{A}$ is applied onto the micro capacitor for 10 min until the voltage reaches a plateau. Later on, the open-circuit voltage is measured for 15 min. The change in voltage is plotted in Figure 6.20. Figure 6.20 shows that at the beginning of the charging process, the voltage increases rapidly in several seconds and gradually reaches a plateau of around 1.7 V, representing two different processes, and will be illustrated in detail in Section 6.3.2. There is a voltage plummet between the ending charging point and the starting point of discharge due to the series resistance of the circuits and hence named IR drop[161]. The measured voltage decreases swiftly below 1 V for the discharging period and finally reaches a plateau of around 0.55 V at 15 min.

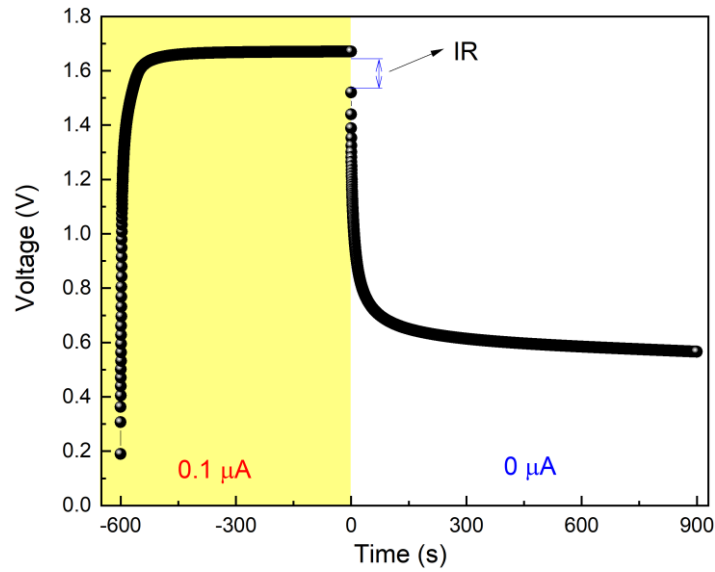


Figure 6.20 The Galvanostatic curve $V(t)$, charge at a constant current of $0.1 \mu\text{A}$. The voltage is measured during the charging process, and the open-circuit voltage is measured as well.

The followed galvanostatic tests with different current values ($0.04 \mu\text{A}$, $0.06 \mu\text{A}$, $0.08 \mu\text{A}$, $0.10 \mu\text{A}$, $0.12 \mu\text{A}$, $0.14 \mu\text{A}$, $0.16 \mu\text{A}$, $0.18 \mu\text{A}$, $0.2 \mu\text{A}$, and $0.22 \mu\text{A}$) is carried out, and the charging and discharging voltage-time curves are plotted in Figure 6.21. The plots show the higher the charging current is, the faster the capacitor is charged.

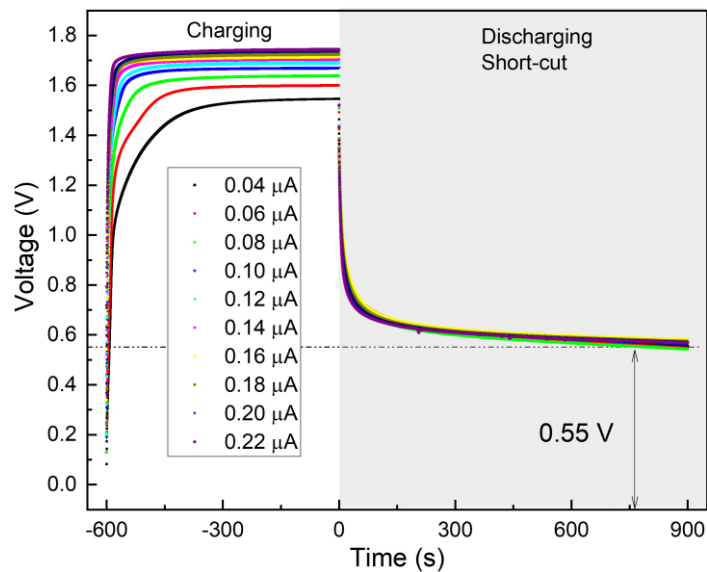


Figure 6.21 Voltage - time plot of galvanostatic test of different charging current ($0.04 \mu\text{A}$, $0.06 \mu\text{A}$, $0.08 \mu\text{A}$, $0.10 \mu\text{A}$, $0.12 \mu\text{A}$, $0.14 \mu\text{A}$, $0.16 \mu\text{A}$, $0.18 \mu\text{A}$, $0.2 \mu\text{A}$, and $0.22 \mu\text{A}$).

The steady voltage in Figure 6.21 increases as the charging current increases. To find out the applied current versus the steady-state voltage correlation, the applied voltage-dependent constant state of charging voltage V_{gc} (gc means galvanostatic charging) is plotted in Figure 6.22. It is stable as the charging current increased in Figure 6.21. However, according to Figure 6.22, V_{gc} still keeps growing with a slight slope.

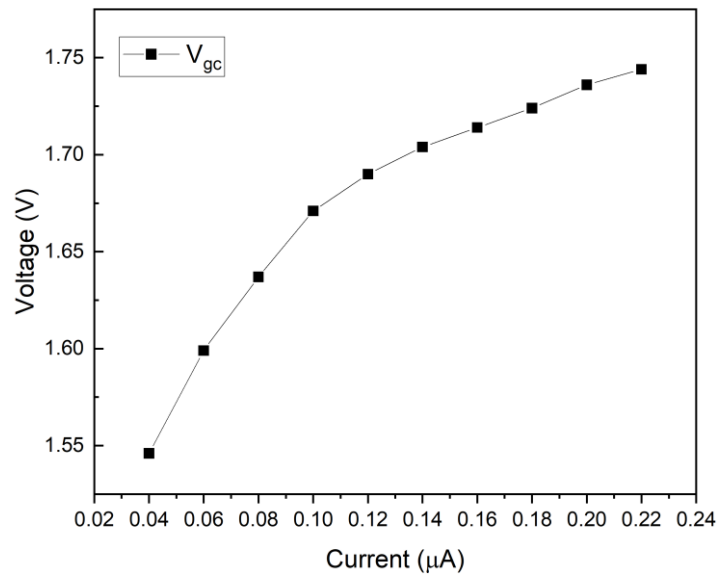


Figure 6.22 The plot of the charging current dependent V_{gc} of the galvanostatic measurement, showing a gradual growth of the voltage value.

When the capacitor is discharged, the ending point of the voltage V_{gd} stays around 0.55 V (Figure 6.23), even after 15 min, due to the series resistance (pure Ohmic behavior) of the whole circuit.

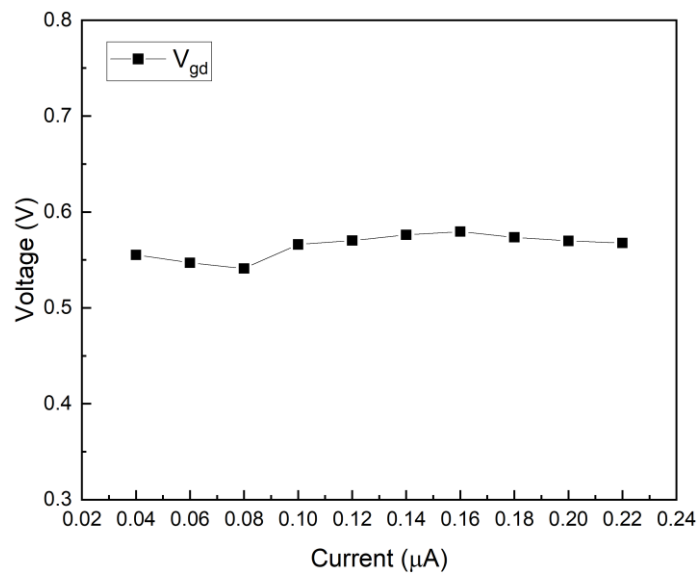


Figure 6.23 The V_{dg} versus the charging current plot of galvanostatic measurement, showing a stable trend of the current.

6.3 Mechanism discussion

6.3.1 Charge transfer behavior

We name the current at the starting charging point as I_{c1} , the current at the ending charging

point as I_{c2} , the current at the starting discharging point as I_{d1} , and the current at the ending discharging point as I_{d2} in Figure 6.24. I_{c2} is noted as the steady-state current.

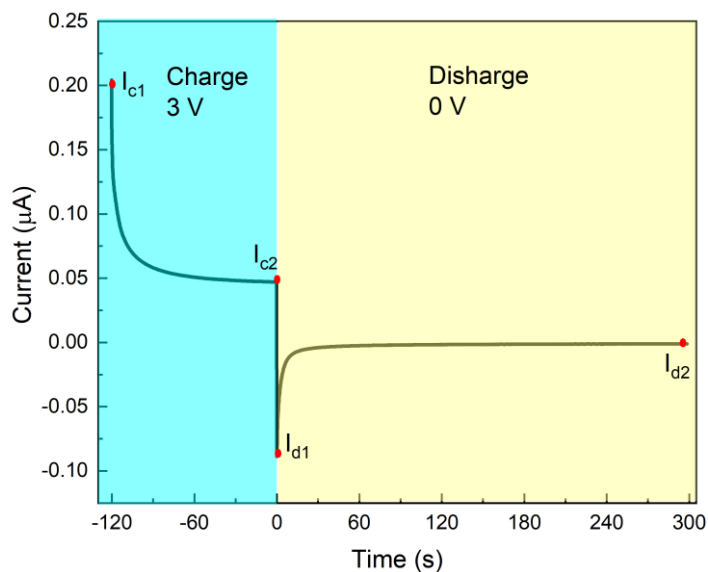


Figure 6.24 The plot of the current transient charged at 3 V. The starting charging point I_{c1} , the ending charging point I_{c2} , and starting discharging point I_{d1} and ending discharging point of the transient I_{d2} is marked with red dots in this figure, separately.

The plot of the steady-state current I_{c2} versus the applied voltage (from 0.1 V to 3 V) in the dry air is drawn in Figure 6.25 to figure out the charge transfer behavior under a dry atmosphere. As a comparison, the same method will be carried out with the interdigitated capacitor that runs in the air saturated with water vapor (Figure 6.27 and Figure 6.28), to figure out the function of water in the charge transfer behavior of this semiconducting β -FeSi₂.

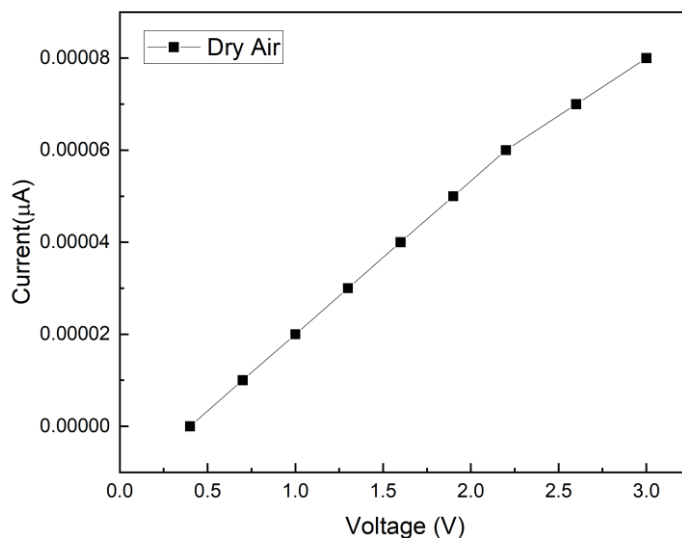


Figure 6.25 Plot of the voltage-dependent steady-state current I_{c2} of the interdigitated capacitor coated with β -FeSi₂ thin film, which is measured in the dry air.

The equations of Fowler-Nordheim tunneling, space-charge-limited current (SCLC), and Poole-Frenkel transport mechanisms are used to fit the $\log(I)$ - $\log(V)$ plot in Figure 6.26 to figure out the charge transfer mechanism under low relative humidity. A double logarithmic plot of Figure 6.25 is

plotted in Figure 6.26. The voltage-dependent current plot's fitting results show that the only satisfactory fitting (R-Square above 0.99) is with the space-charge-limited current equation, as shown in Equation 6.5 below.

$$I = aV + bV^m \quad (6.5)$$

When the injected charges are less than the charge carriers in the sample, linear I-V characteristics can be observed. At a voltage range between 0.1 V and 3 V, the steady-state current increases linearly with the applied voltage, indicating the Ohmic behavior.

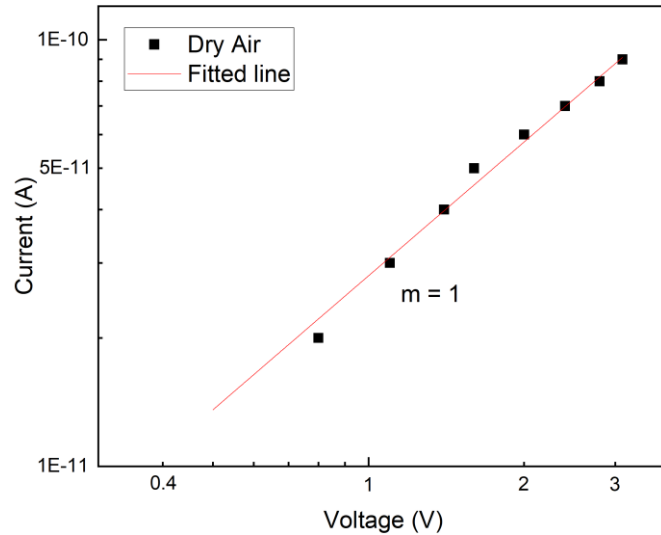


Figure 6.26 Dependence of the steady-state current I_{c2} on the applied voltage (up to 3 V), measured on the interdigitated capacitor at the ambient atmosphere. Red lines represent numerical fits of the experimental data.

The same approach is applied to the same interdigitated capacitor tested under the atmosphere (~ 100% RH water vapor). The applied voltage is from 0.1 V to 3 V, and the voltage-dependent steady-state current is plotted in Figure 6.27.

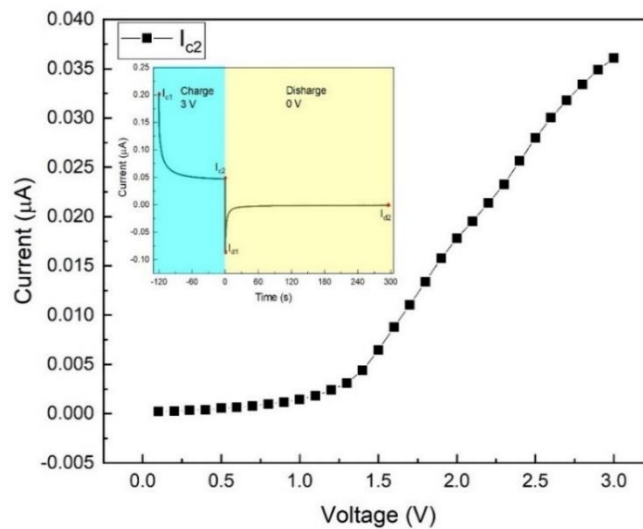


Figure 6.27 The plot of steady-state current I_{c2} versus the applied voltage (0.1 V to 3 V) in the air saturated with water vapor (100% RH)

The double logarithmic plot of Figure 6.27 is plotted in Figure 6.28. Similarly, the equations of Fowler-Nordheim tunneling, space-charge-limited current (SCLC), and Poole-Frenkel transport mechanisms are used to fit the $\log(I)$ - $\log(V)$ plot in Figure 6.28. It confirms that SCLC pattern fits well with the experimental result. The fitting result proves that below 1.1 V, the value of m in Equation 6.5 equals 1, indicating only Ohmic current exists (Figure 6.28). This phenomenon is similar to Figure 6.26.

The region between 1.1 V and 1.9 V, m is 4, which is the trap SCLC region, indicating the existence of “traps” in the charge transport system[162, 163]. The SCLC region with traps begins at a voltage that is noted as V^{TFL} , TFL means traps filled limit. V^{TFL} is 1.1 V in Figure 6.28. In this region, the unfilled traps' density is much greater than that of the density of the injected electrons. In other words, all the injected electrons are trapped.

While for the high voltage from 2 V to 3 V, the traps are filled, the current is dominated by the excessive injected charges through the electrode-semiconductor contact, which enters directly into the conduction band. In this case, $m = 2$, and this charge transfer behavior is also named the space-charge-limited current that is mainly governed by the Mott-Gurney law or the Child's trap-free square law solids[164]. And the corresponding voltage is the starting point of the SCLC trap-free region, which in this case is at the voltage of 2 V. Considering the value of V^{TFL} , it is well fitted with the Henderson, H Thurman[165] conclusion, i.e., the starting voltage of SCLC trap free region is approximately twice as big as V^{TFL} .

Theoretically, the trap-filled-limited curve should be vertical, but the experimental result from different materials, such as CdS[166-168], ZnS[169], and Si[170], shows that the curves are usually non-vertical. The reason for this deviation is still unknown. The three regions form the so-called Lampert Triangle in the dashed-line triangle in Figure 6.28, typical for semiconductors.

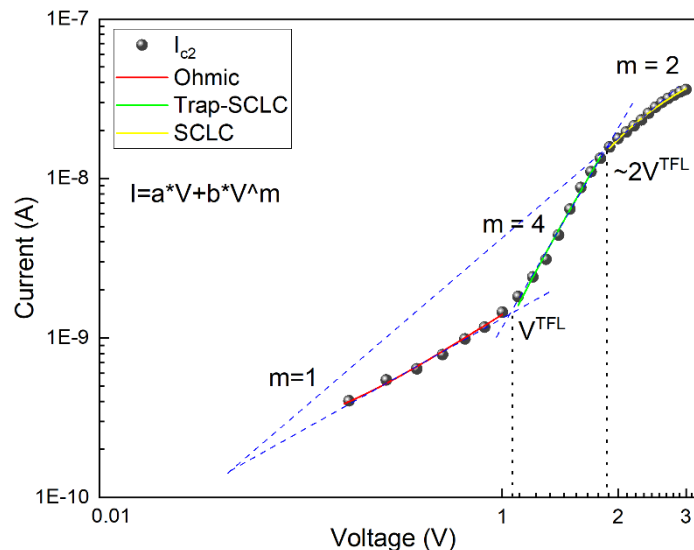


Figure 6.28 Double logarithmic plot of charging ending point I_{c2} versus charging voltage. The Red line (below 1 V) represents the Ohmic regime, the green line (1.1 V to 1.9 V) describes the SCLC regime, and the yellow line (2 V to 3 V) represents the SCLC regime with traps.

It is noticed that the $\log(I) - \log(V)$ plot in the ambient atmosphere (Figure 6.26) is different

from the $\log(I) - \log(V)$ plot (Figure 6.28) achieved in the air with saturated water vapor. Water molecules work as traps under an atmosphere with high relative humidity (1.1 V – 1.9 V). Later on, the water hydrolysis produces lots of cations and anions that can fill the traps (above 2 V), hence influencing the charge transportation behavior.[171]

6.3.2 The establishment of a working model

The electric double-layer capacitor exits because of the water thin-film on the β -FeSi₂ surface. According to Björneholm and Verdaguier[172, 173], in the ambient air with saturated water vapor, a bulk layer of the water film is formed on the nanoparticle surface. The thickness of the thin layer is assumed to be around 3 nm (Figure 6.29) in the air with saturated water vapor[174] (100% relative humidity), which is about ten times the diameter of one water molecule (0.28 nm)[175]. Hence the air with saturated water (100% RH)/ β -FeSi₂ interface can be viewed as a bulk water liquid/ β -FeSi₂ interface. The mechanism of the double electric layer in the solid/liquid interface fits this situation well.

Besides, as mentioned in Section 5.1, the porosity of the β -FeSi₂ thin film is around 45%, the loosely stacked nanoparticles (Figure 6.10 and Figure 6.13) proving full access for water molecules approaching to all the β -FeSi₂ nanoparticles, providing more space to accommodate water molecules, which means each single β -FeSi₂ nanoparticle has full access to the water molecules. In the discussion above, it is assumed that the water film covers all nanoparticles, and the later discussion is based on this.

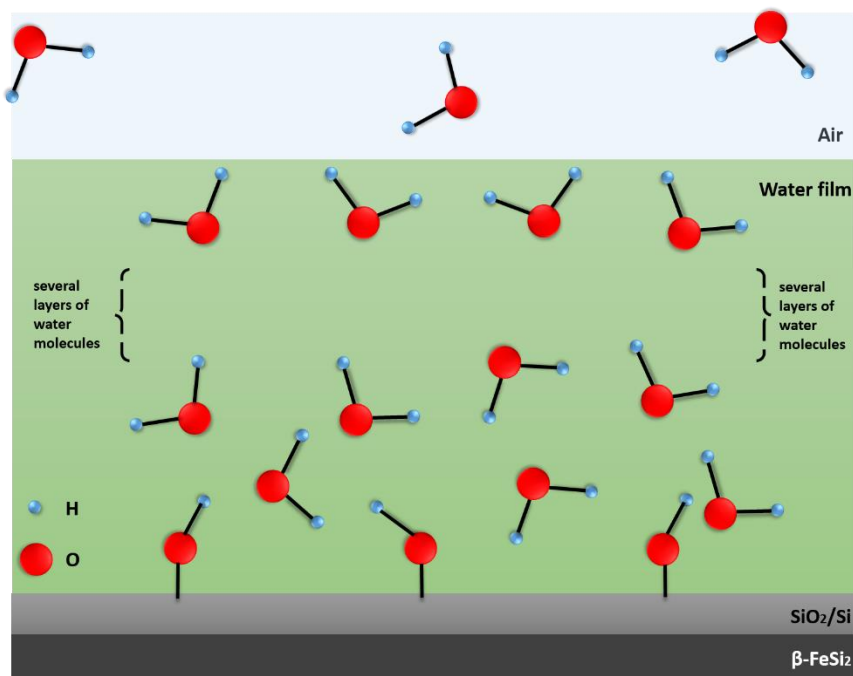


Figure 6.29 The Schematic graph of air with saturated water vapor (100% RH)/ β -FeSi₂ interface, more than 3 nm of the water thin film[173] is formed (around ten layers of water molecules). Red spots represent oxygen atoms, and blue spots represent hydrogen atoms.

Two adjacent particles can be viewed as an interdigitated capacitor to simplify the problem

for the sake of the later discussion. The schematic graph of two adjacent β -FeSi₂ nanoparticles, charged oppositely, in the air saturated with 100% RH H₂O is shown in Figure 6.30. According to Figure 6.30 and Figure 6.6 (XPS result), the dark grey core is β -FeSi₂, and the light grey shell is Si/SiO₂, while the light blue circle represents the water thin film.

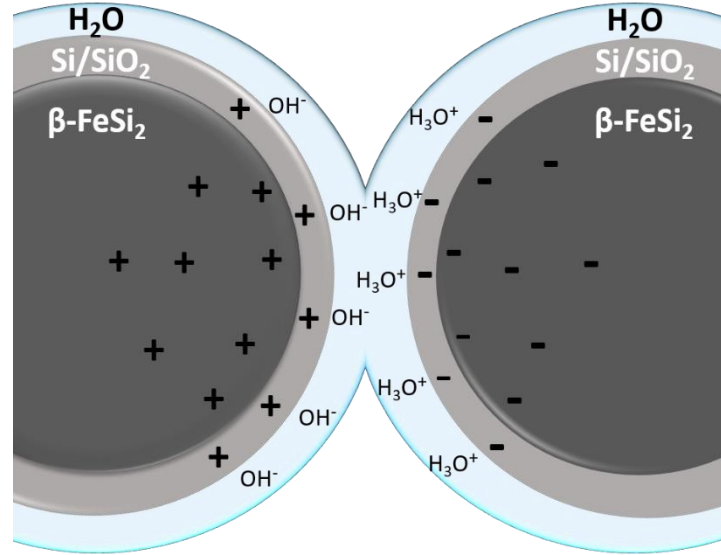


Figure 6.30 The Schematic graph of the charge distribution on nanoparticles while charging in the air saturated water vapor.

A mono-exponential function (Equation 6.6) is employed to fit the current transient in Figure 6.31. However, the current transient cannot be fitted with the mono-exponential equation.

$$I = I_0 + I_1 \exp(-t / \tau), \quad (6.6)$$

It indicates that more than one process taking place during the charging process. A bi-exponential Equation 6.7 is employed to fit the current transient. The coefficient of determination R squared is above 0.99, indicating that the bi-exponential equation fits well with the experimental data. The fitting result (red line) is shown in Figure 6.31.

$$I = I_0 + I_1 \exp(-t / \tau_1) + I_2 \exp(-t / \tau_2) \quad (6.7)$$

The time constant τ is the time a capacitor needed to charge from 0% to 63.25% of fully charged capacitance, or the time required to discharge from 100% to 36.8% capacitance. It is a parameter characterizing the charging/discharging speed of the capacitor. Based on Equation 6.7, the current in the charging process can be fitted with bi-exponential equations, and the current is composited of three parts, I_0 , $I_1 \exp(-t/\tau_1)$, and $I_2 \exp(-t/\tau_2)$. I_0 is the leakage current of the capacitor, $I_1 \exp(-t/\tau_1)$ is the current contributed by the electrical double layer, and $I_2 \exp(-t/\tau_2)$ is contributed by electrostatic capacity.

In this case, the two time constants of the charging process vary quite a lot from each other, τ_2 (14.7 s) is almost 20 times higher than τ_1 (0.7 s), indicating that two different processes are taking

place. These two time constants represent the electric double layer's formation and the static electric capacitor, respectively. For the discharging process, the value of the time constant τ_1' (1.1 s) and τ_2' (14.3 s) are close to the value of the charging process, indicating the reversibility of these two processes.

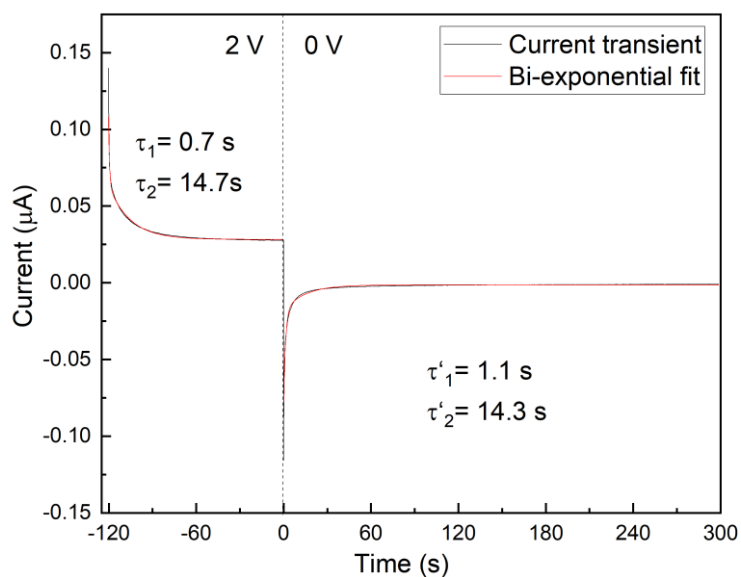


Figure 6.31 Bi-exponential fit with charge and discharge current transient, in which the charging voltage is 3 V. The charging process has two time constants τ_1 (0.7 s) and τ_2 (14.7 s), and the discharging process τ_1' (1.1 s) and τ_2' (14.3 s).

According to the schematic graph in Figure 6.30 and the fitting result of the current transient in Figure 6.31, the overall capacitance of the β -FeSi₂ capacitor is composed of the electric double-layer capacitance (with green dashed line representing the electric double-layer capacitor), and the electrostatic capacitance (red dashed line representing the electrostatic capacitor) produced by the adjacent nanoparticles in Figure 6.32.

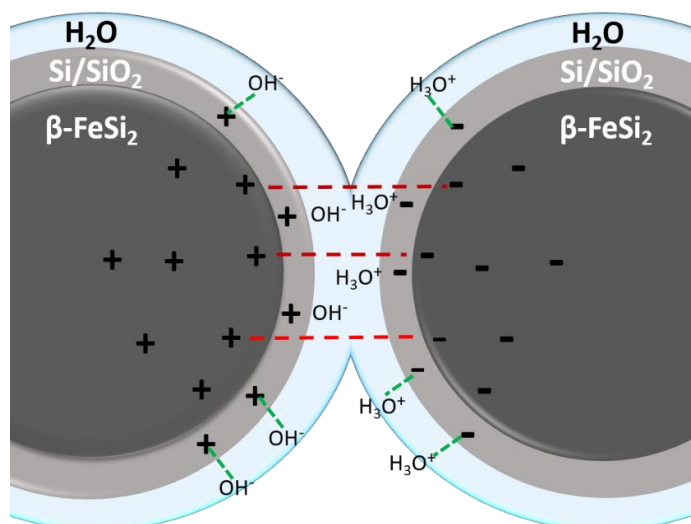


Figure 6.32 The Schematic graph of the charge distribution on nanoparticles while charging in the air saturated water vapor. The electrostatic capacitance exists between two nanoparticles with opposite charges (Red dashed line). The electric double-layer capacitance exists on the interface of β -FeSi₂/H₂O (Green dashed line).

For the capacitor of the adjacent $\beta\text{-FeSi}_2$ nanoparticles, the core part of the $\beta\text{-FeSi}_2$ nanoparticle can be viewed as the electrodes, and the Si/SiO₂ layer and water thin film with higher resistance can be considered to be the dielectric medium. In the charging process, the opposite charges accumulate on each side of the nanoparticles. The charges are electrostatically stored in the nanoparticles.

The equivalent circuit is a widely used method to analyze the circuit physically while maintaining the system's electrical characteristics. Based on the conventional model of the B.E. Conway's illustration in his work *Electrochemical Supercapacitors: Scientific Fundamentals and Technological Applications* (1999), together with the schematic model mentioned in Figure 6.32, an equivalent circuit of the micro capacitor composed with multiple pairs of the adjacent nanoparticles that works in the air with 100% RH is shown in Figure 6.33. The equivalent circuit is a typical multi-RC-element ladder network that comprises R_k , and C_k ($k = 1, \dots, n$). By a rough estimation of the volume of nanoparticle film and the average particle, there are numerous micro capacitors, in the magnitude of 13, which act together in parallel as the whole capacitor. Hence, the interdigitated capacitor's equivalent circuit can be viewed as the multiple parallel plate capacitors connected in parallel (Figure 6.33).

This circuit model is the classic universal circuit model. A more accurate and detailed circuit model needs to be clarified further with electrochemical impedance spectroscopy.

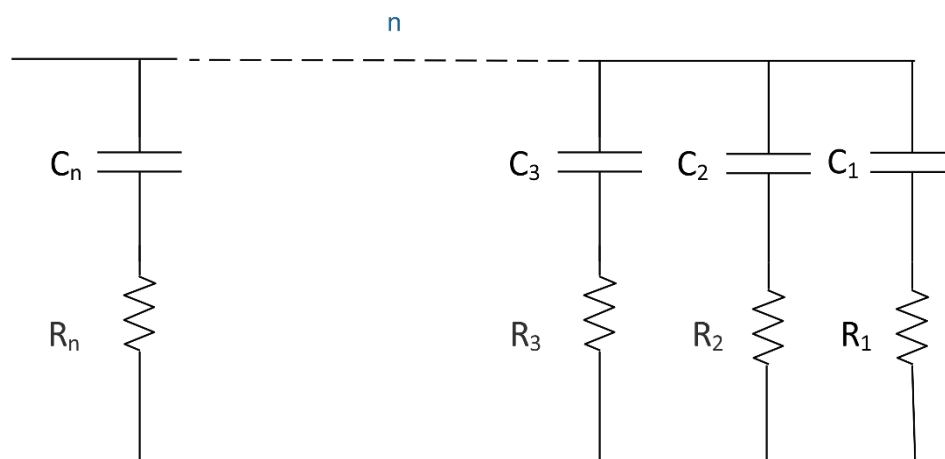


Figure 6.33 The equivalent circuit model of the multi pairs of the adjacent-nanoparticle micro capacitor.

So the overall capacitance is the superimposition of unit capacitance. Considering all pairs of electrodes are with same structure and parameters, the unit capacitance should be the same. The overall capacitance equation is shown in Equation 6.8.

$$C = C_1 + C_2 + \dots + C_n = nC \quad (6.8)$$

Besides, the capacitance value can also be calculated by “transforming” the original capacitor structure to the conventional double-plate capacitor and summing the charge stored on the interface of the nanoparticles and water molecules.

Based on the conventional electrical double layer capacitor[176] and the traditional capacitor's capacitance (Equation 6.9), a rough and straightforward calculation of the theoretical capacitance is conducted.

$$C_{dl} = \frac{A\epsilon\epsilon_0}{d} \quad (6.9)$$

ϵ_0 also can be noted as ϵ_0 is the permittivity of the vacuum, F/m. ϵ is the dielectric constant, also known as relative permittivity. Dielectric constant ϵ of the air saturated with water vapor under room temperature is 1.00021[177]. A is the surface area of capacitance (m^2 or m^2/g). In this case, A is the specific surface area of β -FeSi₂ nanoparticles, i.e., 32.86 m^2/g . d is the distance between two capacitor plates: m. The rough capacitance calculation is Capacitance is around 8.7 μF for 60 μg β -FeSi₂, assuming the thickness of the electric double layer is from 0.3 nm to 3 nm, which is the size of one molecule to ten water molecules. Usually, the practical capacitance is around 20% of ideal capacitance, or even lower[54]. The actual capacitance of the β -FeSi₂ capacitor is approximately 0.1 – 3 μF , based on the thickness of the electric double layer, which agrees reasonably well with the experimental data.

6.3.3 Oxygen sensing measurement

Based on the assumption that the water-splitting does exist at a specific voltage (the accurate water-splitting voltage is varied on different materials), so in this session, the exact water-splitting voltage of β -FeSi₂ is determined by measuring the oxygen produced in the charging process. By roughly estimating the interdigitated capacitor oxygen production, it is found out that the amount of oxygen produced by the interdigitated capacitor is far below the limit of the available oxygen sensing technique. Hence here parallel-plate capacitor that is fully covered by β -FeSi₂ thin film is employed. Clamps are used to make sure effective and close contact between electrodes and separator. The real capacitor and its schematic structure are demonstrated in Figure 6.34.

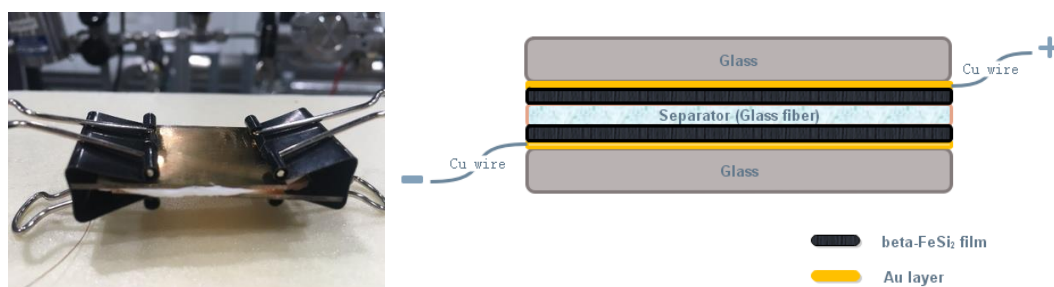


Figure 6.34 The configuration of a real parallel-plate capacitor (above) and the schematic structure of a parallel plate capacitor (down).

The oxygen sensing set-up (Figure 6.35) comprises a water vapor chamber, a sample chamber, and an oxygen sensor. The type of oxygen sensor is OxyTrans II from Pro-Chem Analytik, which uses a particular micro fuel cell to measure the oxygen concentration. The measurement of the full range is from 0 to 1000 ppm. After the sample is put inside the sample chamber, the whole setup is pumped down to around 0.01 mbar. As a gas carrier, a constant nitrogen flow goes through the water chamber till the pressure in the sample chamber gets stable reaches around 20 mbar. Repeat the above process three times, ensuring that before the voltage is applied to the interdigitated

capacitor, the chamber's oxygen concentration stays below three ppm (parts per million).

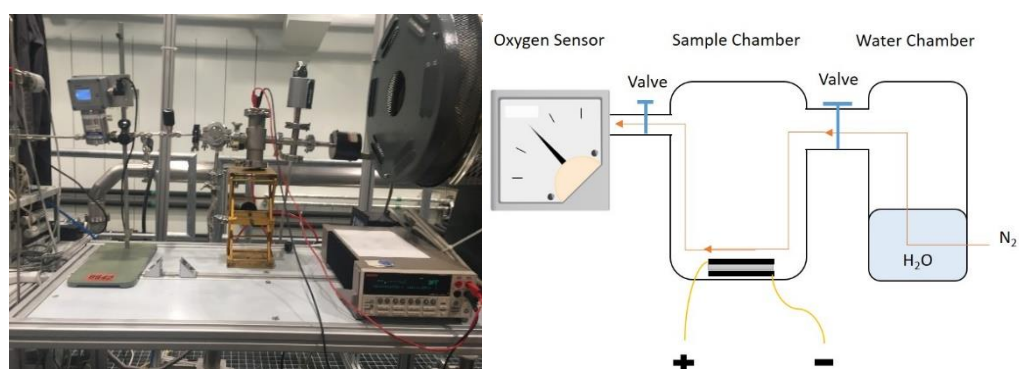


Figure 6.35 The in-situ oxygen sensing system (Left). The oxygen-sensing system's schematic components (right) consist of an oxygen sensor, a sample chamber where the interdigitated capacitor locates and a water chamber that the nitrogen gas can go through.

As a reference, the parallel-plate capacitor is first placed in the sample chamber for 10 min to observe the oxygen concentration stability in the whole sealed setup. Later on, 3 V is applied to the capacitor for another 10 min, and again for 10 min, 0 V is applied to observe the difference in Figure 6.36.

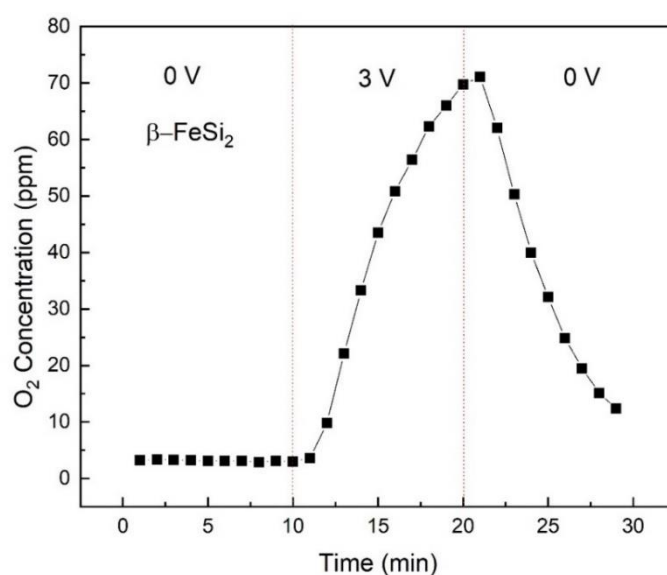


Figure 6.36 The plot of oxygen concentration versus time. The whole testing process includes three steps: I, no voltage is applied for the first ten minutes. II, 3 V is applied for the next 10 minutes. III, Stop applying voltage and wait another 10 minutes.

According to Figure 6.36, nitrogen flow runs continuously and constantly during the process, and the oxygen concentration change is observed and recorded. The oxygen concentration variation through time is plotted in Figure 6.36. According to the plot, oxygen concentration stays at around 3 ppm during the first 0 V period. The oxygen concentration increases at 1 min after applying 3 V, reaching 70 ppm after 10 min. The initial current after applying 3 V is 5 mA and gradually decreases to 2.61 mA. Then 0 V is applied for 10 min, and the oxygen concentration decreases again to 3 ppm. It is worth pointing out that there is a 1 min delay of oxygen signals due to the postponement of oxygen transmission in the chamber of the whole system. This result initially proves the ability of water splitting of β -FeSi₂ parallel-plate capacitor.

The yielded oxygen concentration versus applied voltage is shown in Figure 6.37. Oxygen concentration produced below 2.5 V is too low to be measured. After 2.5 V, the concentration of oxygen starts to increase and rise sharply afterward. The oxygen concentration can reach 250 ppm at 3.75 V.

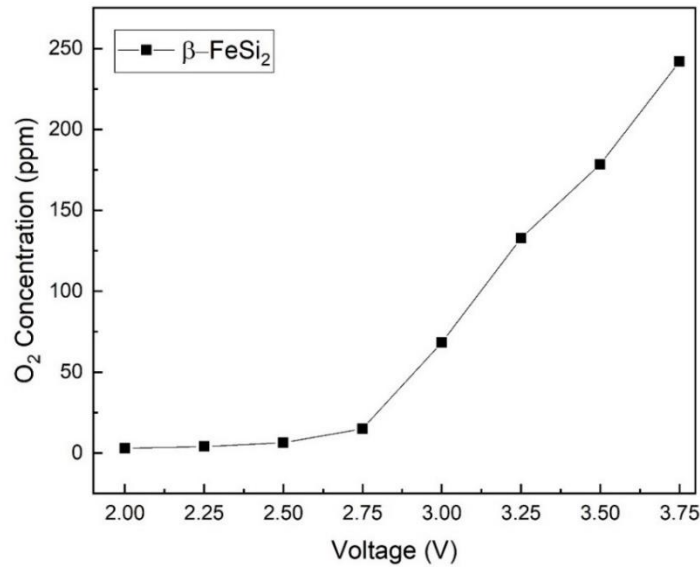


Figure 6.37 The oxygen concentration measured at a different applied voltage (2 V to 3.75 V) of the β -FeSi₂ interdigitated capacitor.

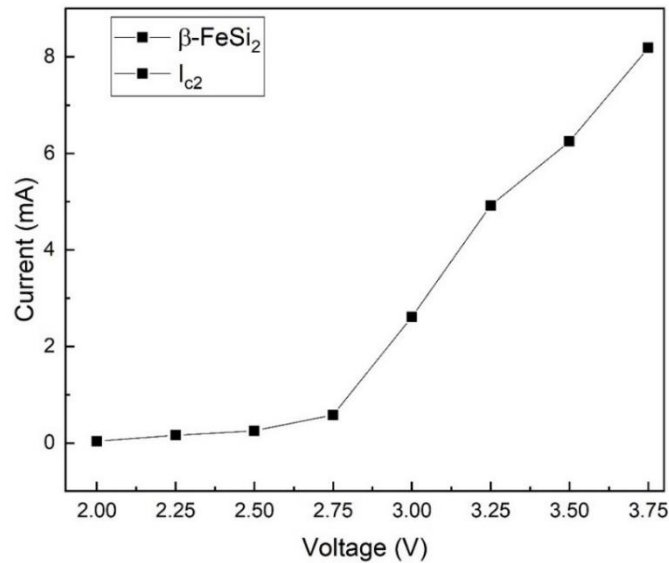


Figure 6.38 The steady-state charged current I_{c2} -Voltage plot of β -FeSi₂ capacitor. The applied voltage ranges from 2 V to 3.75 V.

The voltage-dependent I_{c2} plot (Figure 6.38) synchronizes perfectly with the trend of the oxygen concentration-voltage plot above, proving the positive correlation with oxygen production and the steady-state charged current I_{c2} (I_{c2} is shown in Figure 6.24).

According to Figure 6.36 and Figure 6.38, at 3 V, the produced amount of oxygen P_o is 70 ppm/s in the stable status (ppm: parts per million), the overall molar flow rate of a mixed of the carried gas nitrogen f_n is 50 SCCM. SCCM represents the standard cubic centimetre per minute. One SCCM equals to $7.45 \cdot 10^{-7}$ mol/s, so 50 SCCM is $3.725 \cdot 10^{-5}$ mol/s. The actual O₂ produced per

second m_o is $2.61 \cdot 10^{-9}$ mol, as shown in the following equation.

$$p_o \times f_n = m_o \quad (6.10)$$

The steady-state current at a charging voltage of 3 V (I_o) is 2.61 mA. Hence the moles of the charged-in electrons per second m_e is $2.71 \cdot 10^{-8}$ mol/s.

$$I_o / (e \times N_a) = m_e \quad (6.11)$$

e is the elementary charge 1.6×10^{-19} C. N_a is the Avogadro constant, $6.02 \cdot 10^{23}$ mol⁻¹. According to the oxygen evolution reaction (OER),



The moles of O_2 can be calculated with the oxygen evolution reaction equation, by the moles of electrons divided by 4, which is $6.78 \cdot 10^{-9}$ mol/s. The roughly calculated efficiency per second η is 38.5%.

$$m_o / (m_e / 4) = \eta \quad (6.13)$$

The amount of the electrons used to produce oxygen divided by the total amount of the charged-in electrons divided is 38.5%, which means that 38.5% of all the electrons charged into the capacitor is used for water splitting. That is a tremendous waste, so this capacitor's working voltage is better under 2.5 V when no apparent water splitting occurs.

In summary, the β -FeSi₂ is a semiconducting material, so the interdigitated capacitor with β -FeSi₂ nanoparticles is related to the field of semiconductor electrochemistry. Based on the charge transfer behavior of semiconductors. The charge transferred behavior follows the rule of the space-charge-limited current pattern. The water molecules can work as the "traps." Also, the schematic model with two adjacent nanoparticles is established. According to the model, the capacitance is composed of the capacitance coming from the electric double layer and the static capacitance between two adjacent nanoparticles with the opposite charge. As it is known to all, that water splitting also exists at a higher range of the applied voltage, so the accurate voltage of water splitting with β -FeSi₂ is tested in in-situ oxygen sensing measurement. The results show that after around 2.5 V, oxygen starts to be observed, indicating the beginning of the water splitting. So the working voltage of β -FeSi₂ interdigitated capacitor is from 0 V to 2.5 V.

6.4 Parallel plate capacitor with different materials

Except for the interdigitated structure, the conventional structure, i.e., the possibility of using the double plate structure with β -FeSi₂, is also explored. And the contradiction in the electric performance of these two structures is made.

Besides, it is clear that on the surface of β -FeSi₂ NPs, there is a thin layer of Si/SiO₂. Different materials need to be tested to figure out how much charge Si/SiO₂ can contribute to the overall charge and to explore the possibility of applying other materials onto the same interdigitated micro

capacitor. So in this session, the parallel-plate capacitor is employed to study the different materials, i.e., SiO₂, B-doped silicon.

6.4.1 Parallel plate capacitor with β -FeSi₂ nanoparticles

The synthesis process of the parallel plate capacitor can be found in Section 5.2. 60 μ g β -FeSi₂ NPs are spin-coated on each single electrode plate, so the total active material is 120 μ g. The whole capacitor package with the separator (glass fiber) is placed in the sealed container filled with saturated water vapor in the air for over 24 h, making sure the water molecule can have full access to the nanoparticles.

The charge-voltage plot (Figure 6.39) can also be divided into three zones, zone I, zone II, and zone III, based on the plot's slope. The plot indicates similar behavior as the interdigitated capacitor (Figure 6.17). This proves that the three-zone of the voltage-dependent stored charge plot has nothing to do with geometry but is related to the β -FeSi₂ nanoparticles and water vapor.

The capacitance of different zones is the slope of the linear fitting equation. Based on the fitting, zone I's capacitance is 0.19 F/g, zone II is 0.39 F/g, and zone III has a capacitance of 0.29 F/g. The specific capacitance is comparable to the 3D printing flexible electric double-layer capacitors with a specific capacitance of 38.5 mF/g [178].

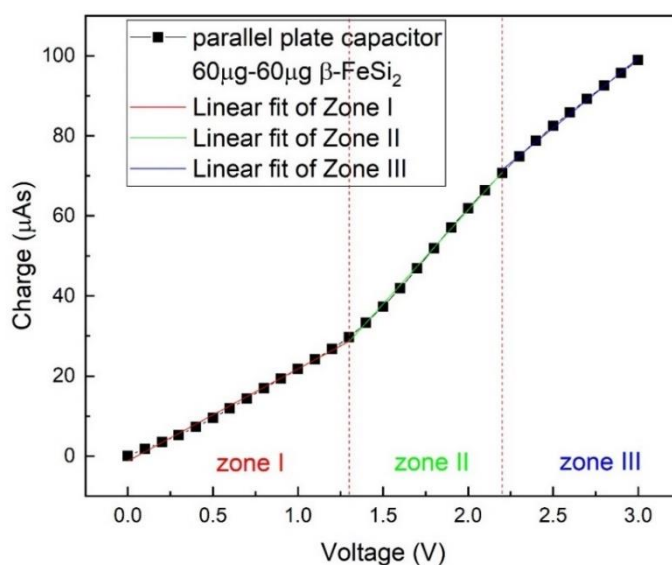


Figure 6.39 The charge-voltage plot of a parallel plate capacitor with β -FeSi₂

Since the mass loading of the parallel-plate capacitor and the interdigitated capacitor is different, so the specific capacitance is calculated and plotted in Figure 6.40, in the convenience comparing the electric performance. The capacitance of the parallel-plate capacitor at 2.5 V is about 11.7 times the capacitance of the interdigitated capacitor. The reasons can be explained with cyclic voltammetry of the double plate capacitor with β -FeSi₂ in Figure 6.41.

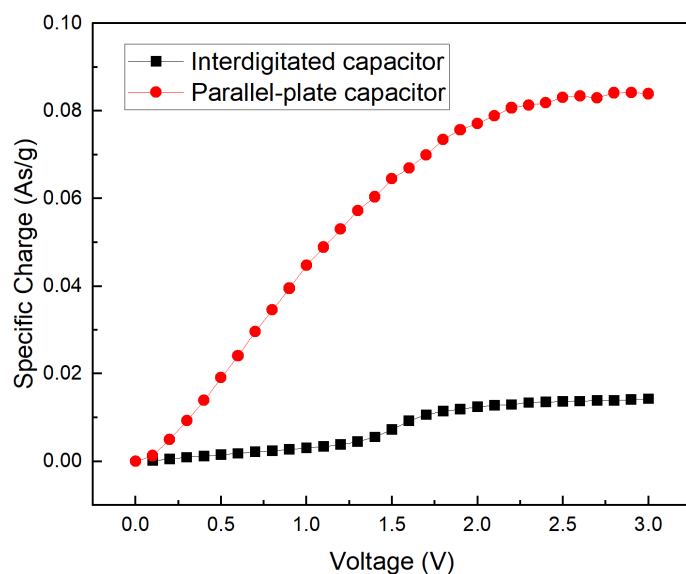


Figure 6.40 Specific charge of a parallel-plate capacitor, compared with an interdigitated capacitor.

According to the cyclic voltammetry plot in Figure 6.41, unlike the cyclic voltammetry plot of the interdigitated structure, the plot of one cycle of scanning (forward and reverse scanning) is in the shape of a rhombus, indicating that the geometry of double plate capacitor also plays a pretty important role, together with $\beta\text{-FeSi}_2$. The resistance of the whole capacitor is quite significant. The high resistance is due to the low conductivity of $\beta\text{-FeSi}_2$ as semiconducting materials.

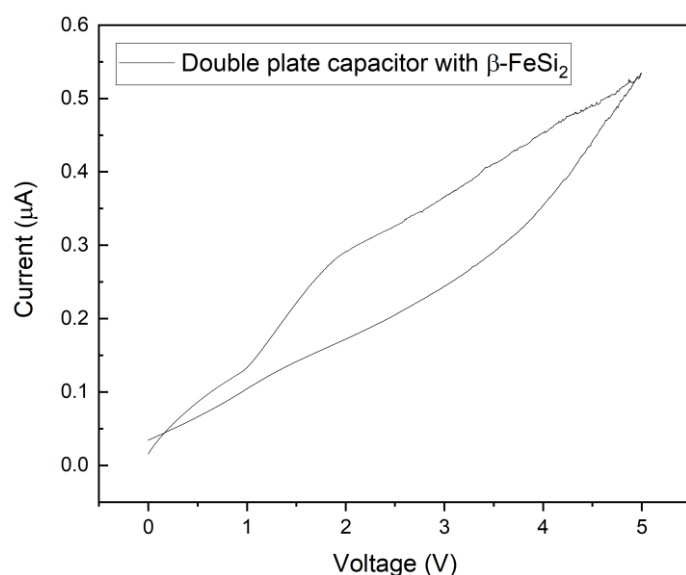


Figure 6.41 Cyclic Voltammetry of double plate capacitor with $\beta\text{-FeSi}_2$ nanoparticles

The voltage-dependent series resistance (V/I_{c2}) of the double plate capacitor with $\beta\text{-FeSi}_2$ nanoparticles is plotted in Figure 6.42. The maximum resistance is up to $8\text{ M}\Omega$, which is only 0.1% of the resistance of the $\beta\text{-FeSi}_2$ interdigitated capacitor. The double plate capacitor's series resistance goes down to $1\text{ M}\Omega$ as the applied voltage goes up. This trend is similar to that of $\beta\text{-FeSi}_2$ interdigitated capacitor, i.e., the series resistance goes down as the applied voltage goes up.

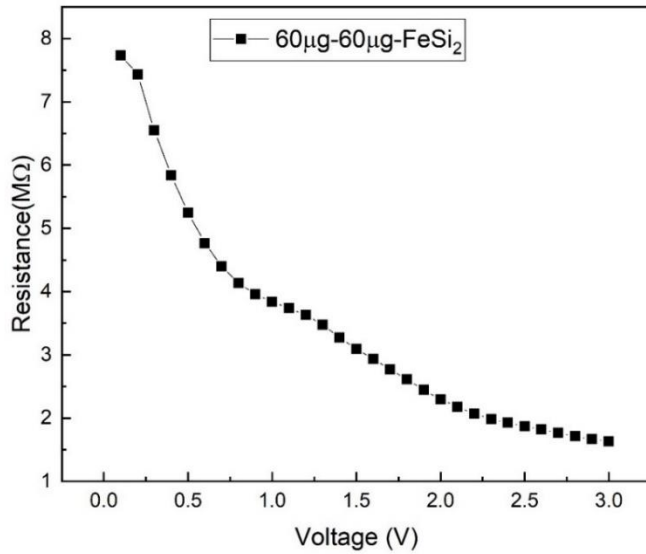


Figure 6.42 The series resistance of β -FeSi₂ parallel-plate capacitor.

6.4.2 Parallel plate capacitor with SiO₂ nanoparticles

According to the XPS result, there is a thin layer of SiO₂ on the surface of β -FeSi₂. A parallel plate capacitor with the same amount of pure SiO₂ (Aerosil OX50, Evonik) is charged and discharged at the same voltage range to figure out the charge contribution of SiO₂. Need to be mentioned, the specific surface area of SiO₂ (around 50 m²/g) is similar to β -FeSi₂ (approximately 32.9 m²/g). A plot of voltage depended stored charge with SiO₂ nanoparticles is shown in Figure 6.43.

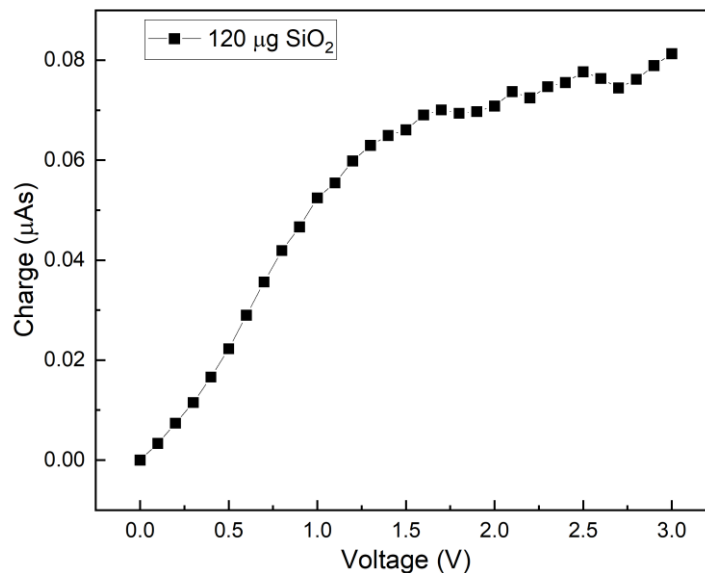


Figure 6.43 The stored charge of the parallel-plate capacitor with SiO₂ nanoparticles.

The Q-V plot of SiO₂ and β -FeSi₂ NPs are plotted in Figure 6.44. The Q-V plot of SiO₂ doesn't show similar behavior as β -FeSi₂, and the stored charge is only 0.08 μAs. The stored charge of β -FeSi₂ is 4 orders of magnitude as the charge stored in the same amount of SiO₂, indicating that the contribution of SiO₂ to charges is nearly negligible. The reason for the poor electric performance is the high series resistance which is shown in Figure 6.45.

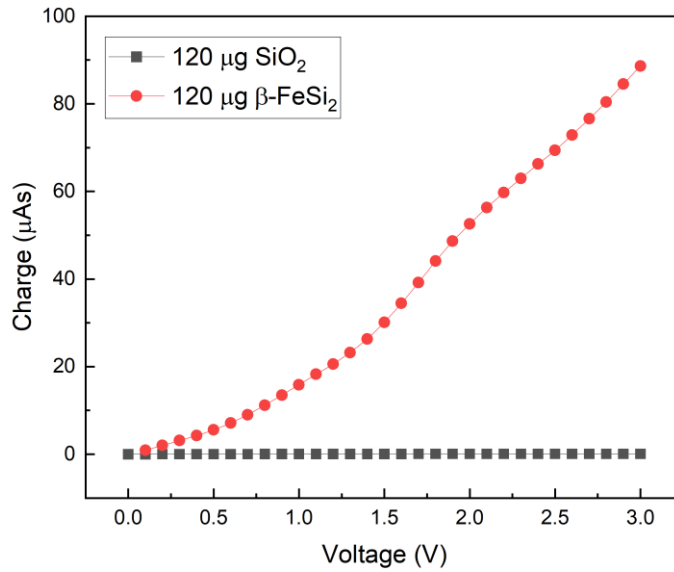


Figure 6.44 Stored charge comparison between β -FeSi₂ and SiO₂(both in parallel plate capacitor configuration).

A series resistance V/I_{c1} is 2100 M Ω at 3 V, three orders of magnitude higher than the series resistance of β -FeSi₂ (around 1.5 M Ω). It is most probably because of the low conductivity, which leads to poor power performance.

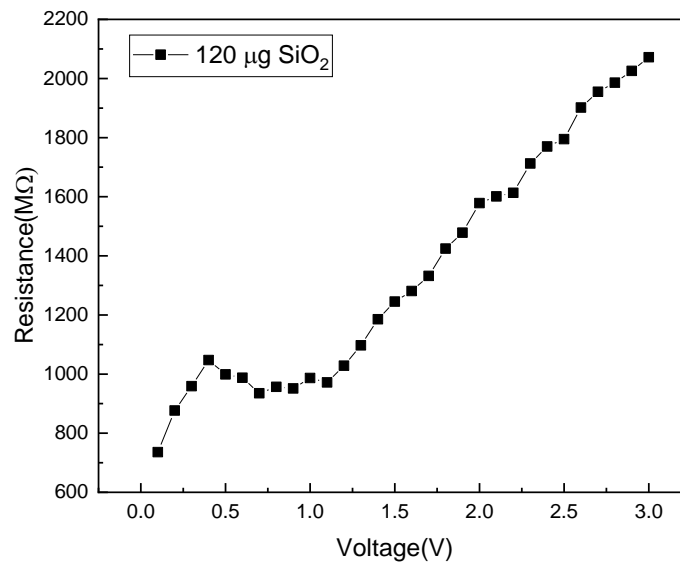


Figure 6.45 The series resistance of the SiO₂ parallel-plate capacitor.

6.4.3 Parallel plate capacitor with B-doped silicon

Besides the SiO₂ mentioned above, B-doped silicon's storage capability is also tested to explore the possibility of applying other materials in the potentiostatic test under the same condition (100% RH, water vapor). In this case, highly boron-doped silicon is employed, which is provided by IVG (Institute for combustion and gas dynamics university of Duisburg-Essen).

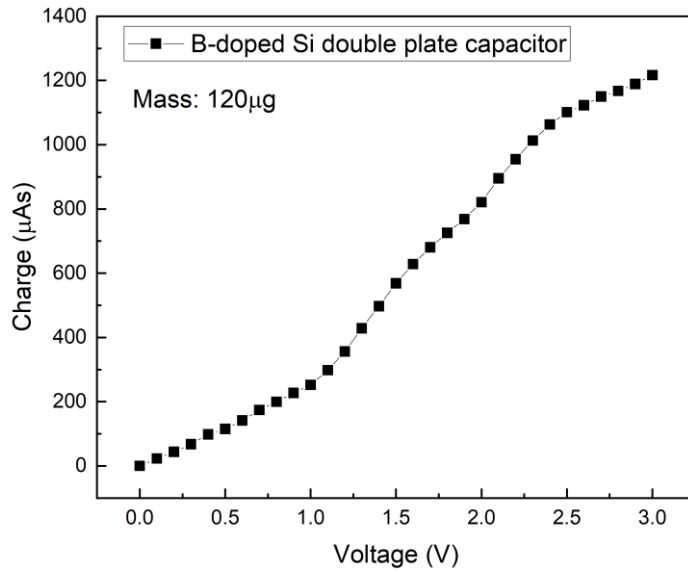


Figure 6.46 The stored charge-applied voltage plot of a parallel plate capacitor with B-doped Si.

Boron doped silicon is with a 0.4% mass concentration of boron and a specific surface area of $19.5 \text{ m}^2/\text{g}$. The stored charge is surprisingly high (Figure 6.46). The stored charge at 3 V is around $1400 \text{ } \mu\text{As}$ under the same measuring condition, which is approximately 10-20 times higher than $\beta\text{-FeSi}_2$ capacitor with the same mass loading.

The series resistance (when the capacitor is fully charged) of B-doped silicon is a maximum of $5 \text{ M}\Omega$, down to $200 \text{ k}\Omega$, much lower than that of the $\beta\text{-FeSi}_2$ capacitor (Figure 6.47). Under the same applied voltage, the larger the series resistance is, the smaller the current transient. The series resistance difference is 1 – 2 orders of magnitude, which primarily influence the current transient by order of magnitude. As the earlier chapter described, the stored charge is achieved by integrating the current transient over time. Therefore the lower series resistance becomes one of the main reasons for higher capacitance.

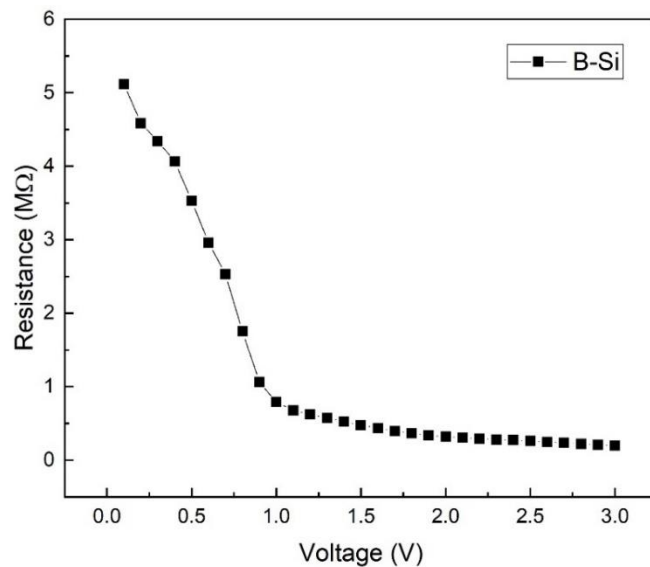


Figure 6.47 The series resistance (V/I_{c2}) of the B-doped silicon capacitor, with a sharp decreasing trend before 1 V and a gentle decrease afterward.

6.5 Mass-dependent stored charge

The β -FeSi₂ interdigitated capacitors with different loading mass are electrically measured. The stored charge at different mass (20 μg , 40 μg , 60 μg , 80 μg , and 100 μg) applied at different applied voltage (1 V, 2 V, and 3 V) is plotted in Figure 6.48.

The charge doesn't have a linear correlation with mass, it increases first and then decreases, as the mass increase and get stable later on. For less mass loading capacitor (20 μg – 40 μg), nanoparticles are both electric well connected and have good access to water vapor. For extensive mass loading (above 60 μg), the nanoparticles on top are not electric well-connected, which might explain the charge decreases along with the increasing mass.

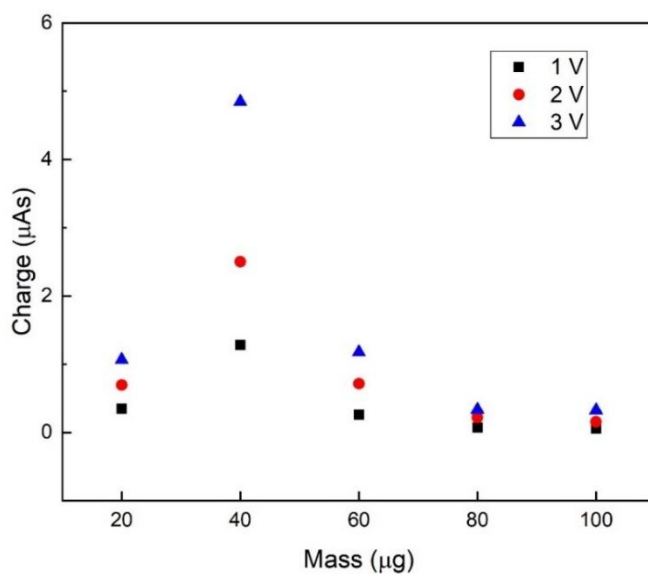


Figure 6.48 Stored charge dependence on the loading mass of β -FeSi₂ nanoparticles coated interdigitated capacitor.

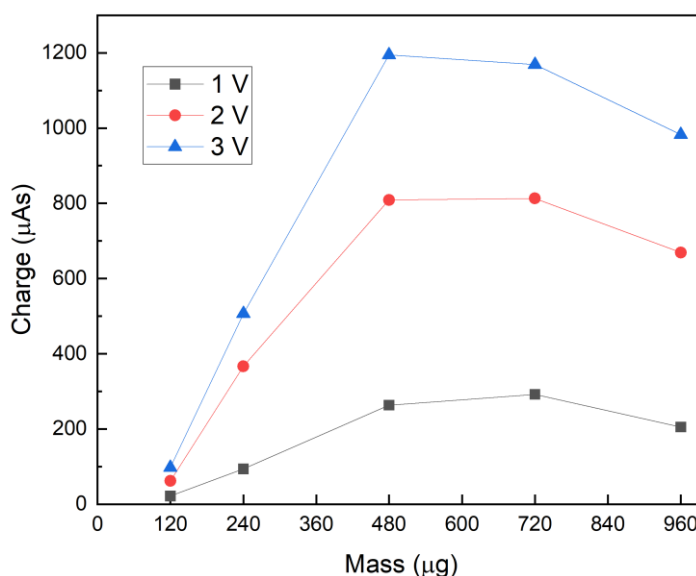


Figure 6.49 Stored charge dependence on the parallel plate capacitor's loading mass coated with β -FeSi₂ nanoparticles.

Mass dependence is also measured with a parallel-plate capacitor in Figure 6.49. The charge and discharge current transient of capacitors with 120 μg , 240 μg , 480 μg , 720 μg , and 960 μg are measured. Not surprisingly, the mass-charge correlation shows a similar behavior as the interdigitated structure.

6.6 Additive polyacrylic acid

The $\beta\text{-FeSi}_2$ nanoparticles coated on the interdigitated micro capacitor have a pretty weak contact with each other, as well as with the interdigitated structure, i.e., the conductive electrodes, according to SEM photo (Figure 6.1). To solve this problem, polyacrylic acid (PAA) is employed as the binder to enhance the contact between the $\beta\text{-FeSi}_2$ nanoparticles.

Polyacrylic acid[179] is an amorphous high-molecular polymer with long-chain carbon chains and carboxyl functional groups (Figure 6.50). It is an adhesive additive widely used in the battery industry and can largely improve the contact between the active material nanoparticles and the current collector. Polyacrylic acid has better adhesion strength[180], higher thermal stability, smaller volume expansion, and larger diffusivity than the other adhesive additive, such as polyvinylidene difluoride (PVDF) and Carboxymethyl Cellulose (CMC)[181]. Most importantly, polyacrylic acid is electrochemical inert under the working voltage. There are no side reactions needed to be considered.

The stored charge of interdigitated capacitors gets higher as the PAA concentration goes up until 16.7% because PAA is a helpful adhesive additive that enhances the inter-contact between nanoparticles. However, PAA is not conductive, so excessive PAA will negatively influence conductivity and lead to poorer electrical performance.

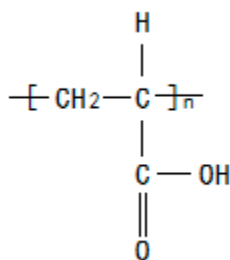


Figure 6.50 The molecular structure of polyacrylic acid.

Polyacrylic acid is a white powder and soluble in water and ethanol and is often used in the form of a gel (light yellow). 25% polyacrylic acid gel (in water) is employed and added to the $\beta\text{-FeSi}_2$ suspension. Figure 6.51 shows the micrograph of the micro capacitor spin-coated with 60 $\beta\text{-FeSi}_2$ and 20 wt.% PAA. The $\beta\text{-FeSi}_2$ suspension with a different ratio of PAA is spin-coated with a rotating speed of 1300 rpm for 2 min. However, PAA is so sticky that $\beta\text{-FeSi}_2$ NPs are not homogeneously distributed. Hence the thickness of $\beta\text{-FeSi}_2$ thin film on edge is thicker than that on the center.



Figure 6.51 The microscope graph of the micro capacitor coated with 60 μg $\beta\text{-FeSi}_2$ and 20 wt.% PAA.

In addition, 3 μg (4.76 wt.%), 9 μg (13 wt.%), 12 μg (16.7 wt.%), and 15 μg (20 wt.%) of polyacrylic acid gel is added to capacitors with same amount of $\beta\text{-FeSi}_2$ (60 μg) under 100% RH. The stored charge of $\beta\text{-FeSi}_2$ with various PAA concentrations (Figure 6.52) shows 12 μg polyacrylic acid gel (16.7 wt.%) in the capacitor can provide the best performance of all. The capacity is four times higher than the pure $\beta\text{-FeSi}_2$ capacitor.

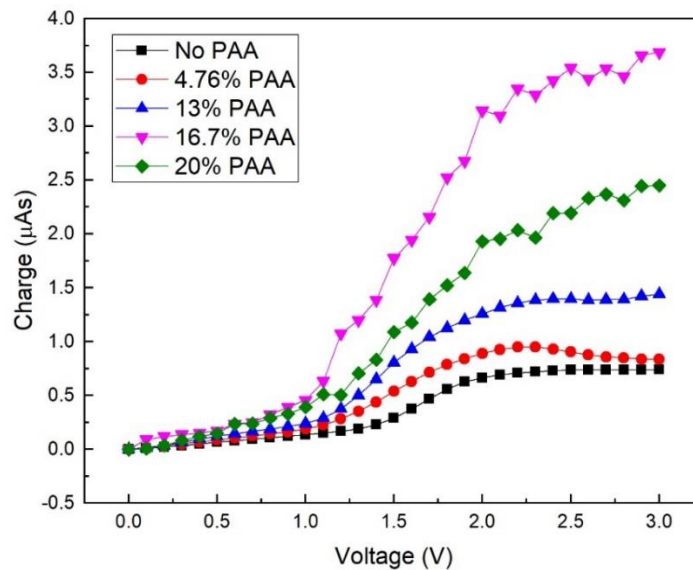


Figure 6.52 Charge storage of capacitor with different PAA concentrations in the air saturated water vapor (100% RH).

To get a hint of the stored charge-PAA concentration relationship, series resistance R_{c1} and R_{c2} are calculated and plotted in Figure 6.53 and Figure 6.54. R_{c1} is defined as V divided by I_{c1} , and R_{c2} is V divided by I_{c2} (I_{c1} and I_{c2} is noted in Figure 6.24). The PAA concentration-dependent R_{c1} and R_{c2} plots show the opposite trend of PAA concentration-dependent stored charge. What is more, the system resistance of the micro capacitor with 16.7 wt.% is the lowest.

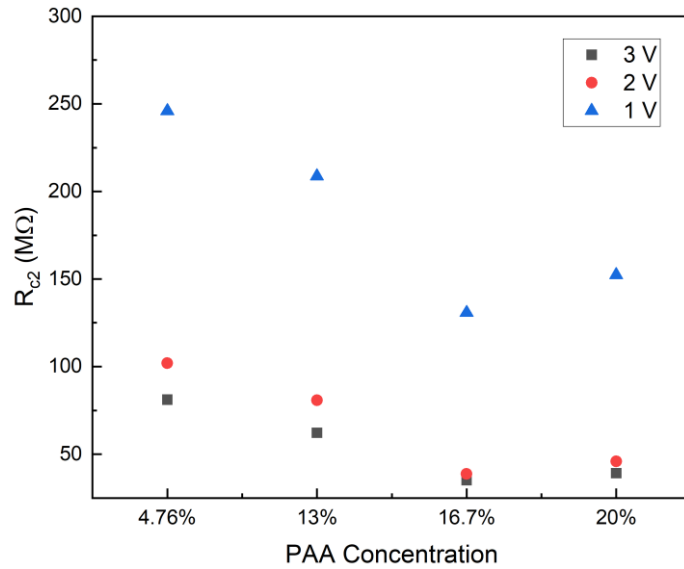


Figure 6.53 Different PAA concentration-dependent series resistance R_{c2} of the interdigitated capacitor coated with β -FeSi₂ nanoparticles.

The stored charge of interdigitated capacitors increases as the PAA concentration goes up until 16.7% because PAA is a helpful adhesive additive that enhances the inter-contact between nanoparticles. However, PAA is not conductive, so excessive PAA will negatively influence conductivity and lead to poorer electrical performance.

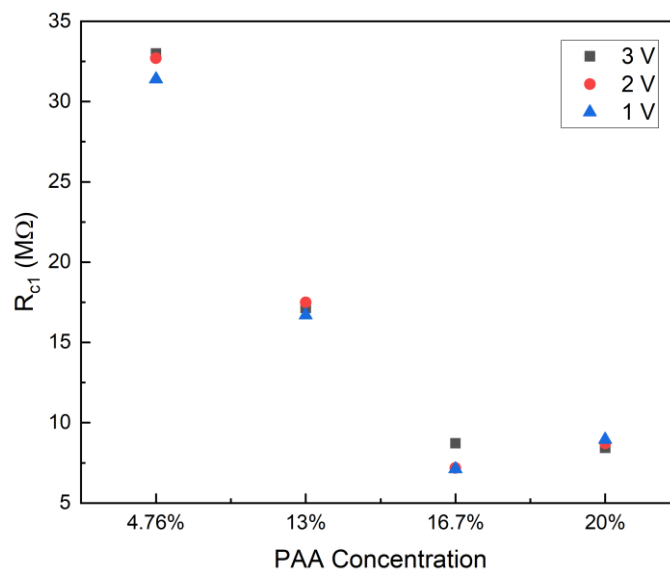


Figure 6.54 Different PAA concentration-dependent series resistance R_{c1} of the interdigitated capacitor coated with β -FeSi₂ nanoparticles.

7 Summary

The present work aims at developing an open-type micro interdigitated capacitor and studying its working mechanism. The micro capacitor is fabricated by printing the Au interdigitated pattern onto the silicon dioxide substrate. The substrate with interdigitated pattern is covered by a thin film of β -FeSi₂ nanoparticles. β -FeSi₂ nanoparticles work as the electrode material, together with the Au interdigitated pattern functioning as the conductive electrode component. Unlike the sealed flat or radial supercapacitor, the proposed micro interdigitated capacitor enables full access to the ambient air saturated with water vapor working as the electrolyte. The micro interdigitated capacitor is environmentally friendly and cost-effective, because the electrode material and electrolyte are abundant on the earth, and completely non-toxic. Additionally, the capacitor is portable due to its small size, facilitating the multi-capacitor electronic package.

- 1) β -FeSi₂ semiconducting nanoparticles are synthesized by gas-phase method in the hot-wall reactor, by the decomposition of two precursors, silane (SiH₄) and iron pentacarbonyl (Fe(CO)₅). The XRD pattern shows that the as-synthesized nanoparticle is pure β -FeSi₂. The SEM photo and XPS spectra proves that β -FeSi₂ is a sponge-like nanoparticle with a thin layer of Si/SiO₂ on the surface. The nanoparticle's size mainly distributes between 18.5 nm and 62.7 nm, with an average size of 35.5 nm. BET result indicates that the specific surface area of the as-synthesized β -FeSi₂ is 32.9 m²/g, with no porous structure on the surface.
- 2) The assembly of the interdigitated structure employs the technique of optical lithography. A gold interdigitated pattern (1.96 mm × 1.96 mm) is printed on a 4 × 4 mm² SiO₂ substrate, and β -FeSi₂ thin film is formed by spin coating. The capacitor is placed in the air saturated with water vapor. Then, the time-dependent current transient is measured at different charging voltage (0.1 V – 3 V). The charge versus applied voltage plot shows the capacitor can store charge in the air saturated with water vapor. However, the interdigitated capacitor running in the dry air or without β -FeSi₂ thin film has negligible charge storage ability.
- 3) The contribution of water molecules and β -FeSi₂ NPs of capacitance is investigated. Considering the β -FeSi₂ to be a semiconducting material, the working mechanism of the interdigitated capacitor coated with β -FeSi₂ nanoparticles is related to the field of semiconductor electrochemistry. The charge transfer behavior of the semiconducting β -FeSi₂ NPs follows the rule of the space-charge-limited current pattern. In addition, the schematic model with two adjacent nanoparticles is established. According to the model, the capacitance comes from the electric double layer and the static capacitance between two adjacent nanoparticles with the opposite charge. The accurate voltage of water splitting with β -FeSi₂ is obtained in the in-situ oxygen sensing measurement: after around 2.5 V, oxygen can be observed, indicating the beginning of the water splitting. So the working voltage of β -FeSi₂ interdigitated capacitor is from 0 V to 2.5 V.
- 4) The electrical performance of the parallel-plate capacitor is investigated, compared to the performance of the interdigitated capacitor. The parallel-plate capacitor has a similar Q-V plot

to the interdigitated micro capacitor. However, the parallel-plate capacitor's capacitance is approximately 11 times higher than the interdigitated micro capacitor, showing its potential in the application of the devices with higher energy density. The strengths of the interdigitated and parallel-plate capacitors leads to different applications: the interdigitated capacitor can be applied in the occasion that requires a small-sized structure but a relatively lower energy density. For higher energy density applications, the traditional parallel-plate capacitor is widely employed.

- 5) The electrical performance's dependence of β -FeSi₂ NPs on mass is also studied in this work. The stored charge of the interdigitated capacitor goes up first, along with the increasing mass, and then decreases after 40 μ g. For lower mass-loading capacitor (20 μ g – 40 μ g), nanoparticles are electrically well-connected. For higher mass-loading (above 60 μ g), the nanoparticles on the top surface are not electrically well-connected, leading to the decreased charge along with the increasing mass. The parallel-plate capacitor has the same mass dependence behavior.
- 6) Polyacid acid (PAA) is added to β -FeSi₂ nanoparticles to enhance the electric contact between nanoparticles. The electrical performance of the interdigitated capacitor with different PAA ratios are investigated. The Q-V plot shows that with a higher concentration of PAA (4.76% – 16.7%), the stored charge of the interdigitated capacitor increases. However, as more PAA is added (20%), the stored charge drops. The series resistance of the capacitor decreases as the PAA concentration increases (up to 16.7%), then increases as the PAA concentration reaches 20%. The change of the series resistance indicates excessive PAA concentration can block the connection between nanoparticles, resulting in the decreased electric conductivity.
- 7) Furthermore, another two materials, SiO₂ NPs and B-Si NPs are used in the parallel-plate capacitors to explore the possibility of different materials. The parallel-plate capacitor with SiO₂ NPs has a negligible stored charge compared to the capacitor with β -FeSi₂ NPs. The series resistance of the SiO₂ capacitor is about three order of magnitudes higher than the capacitor with β -FeSi₂ NPs, causing a much lower stored charge of the SiO₂ capacitor. On the contrary, the capacitor with B-Si NPs shows superior capacitance than β -FeSi₂ NPs. The applied voltage-dependent stored charge of the B-Si capacitor shows a similar kink as the β -FeSi₂ capacitor. , Compared to the β -FeSi₂ capacitor, the B-Si capacitor stores more charges and has a lower resistance, resulting in a higher self-discharge rate.

8 Further work and outlook

- 1) Electrical performance in a different atmosphere, such as acetone and the mixture of acetone and water, is also measured to explore the possibility of using another gaseous atmosphere in the charging and discharging measurement. The Q-V plot of acetone in Figure 8.1 (left) is linearly correlated, with no similar kink as the Q-V plot of the same capacitor tested in water vapor. The stored charge is lower than that of the water vapor saturated in the air. While the Q-V plot achieved under a mixture of water/acetone, in Figure 8.1 (right), is linearly correlated before 2 V (same behavior as in acetone), followed by a plateau. Interestingly, the stored charge achieved in the water/acetone atmosphere is 3-4 times higher than the stored charge in the water vapor or acetone. The Q-V plot differs from the different atmospheres, indicating different charge and discharge mechanisms. The reason why the capacitor in the water/acetone atmosphere shows superior performance is not clear. Further work needs to be done to study the interdigitated capacitor's working mechanism with β -FeSi₂ nanoparticles in a different atmosphere.

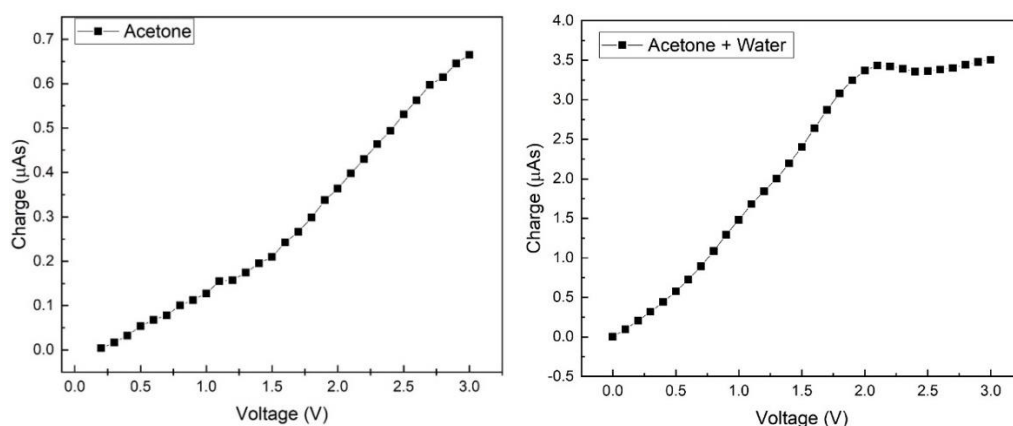


Figure 8.1 Charge storage in saturated acetone vapor (Left). Charge storage in saturated water-acetone mixture vapor (Right).

- 2) Considering water vapor is not as conductive as other electrolytes, potassium hydroxide (KOH) is used to improve the parallel-plate capacitor's conductivity. The glass microfiber soaked with KOH solution is dried before use. The experimental result in Figure 8.2 (left) shows the charge with KOH glass microfiber is 56 times without KOH. However, the gold layer on the capacitor with KOH separator is relatively easy to be exfoliated in Figure 8.2 (right), thus aggregating the cyclic property. Further study is needed to improve the structure of the capacitor with a KOH solution.

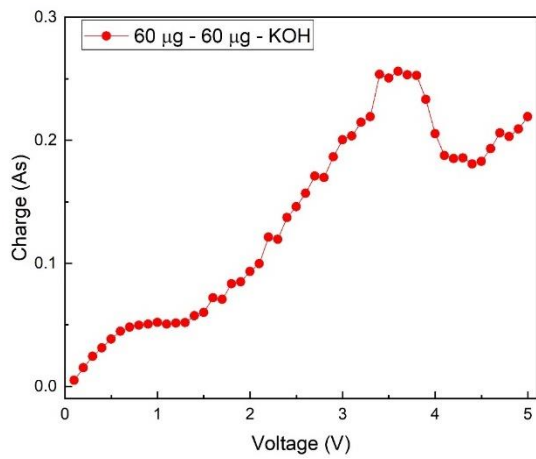


Figure 8.2 Parallel capacitor with KOH additive (Left). The exfoliation condition of gold-coated plate electrode with KOH additive (right).

9 Reference

- [1] J.T. Kiehl, K.E. Trenberth, Earth's annual global mean energy budget, *Bulletin of the American Meteorological Society* 78(2) (1997) 197-208.
- [2] V. Etacheri, R. Marom, R. Elazari, G. Salitra, D. Aurbach, Challenges in the development of advanced Li-ion batteries: a review, *Energy & Environmental Science* 4(9) (2011) 3243-3262.
- [3] S.W. Kim, D.H. Seo, X. Ma, G. Ceder, K. Kang, Electrode materials for rechargeable sodium-ion batteries: potential alternatives to current lithium-ion batteries, *Advanced Energy Materials* 2(7) (2012) 710-721.
- [4] X. Lu, Y. Zeng, M. Yu, T. Zhai, C. Liang, S. Xie, M.S. Balogun, Y. Tong, Oxygen-deficient hematite nanorods as high-performance and novel negative electrodes for flexible asymmetric supercapacitors, *Advanced materials* 26(19) (2014) 3148-3155.
- [5] K. Naceur, J. Gagné, *Global EV outlook 2017*, International Energy Agency (IEA): Paris, France (2016).
- [6] V.S. Bagotsky, A.M. Skundin, Y.M. Volkovich, *Electrochemical power sources: batteries, fuel cells, and supercapacitors*, John Wiley & Sons 2015.
- [7] Z. Liu, S. Wang, N. Otagawa, Y. Suzuki, M. Osamura, Y. Fukuzawa, T. Ootsuka, Y. Nakayama, H. Tanoue, Y. Makita, A thin-film solar cell of high-quality β -FeSi₂/Si heterojunction prepared by sputtering, *Solar Energy Materials and Solar Cells* 90(3) (2006) 276-282.
- [8] G. Dalapati, S. Liew, A. Wong, Y. Chai, S. Chiam, D. Chi, Photovoltaic characteristics of p- β -FeSi₂ (Al)/n-Si (100) heterojunction solar cells and the effects of interfacial engineering, *Applied Physics Letters* 98(1) (2011) 013507.
- [9] Y. Maeda, Semiconducting β -FeSi₂ towards optoelectronics and photonics, *Thin Solid Films* 515(22) (2007) 8118-8121.
- [10] D. Leong, M.A. Harry, K. Homewood, K.J.R. Kirkby, *Optoelectronic semiconductor devices*, Google Patents, 2001.
- [11] Q. Meng, W. Fan, R. Chen, Z. Munir, Thermoelectric properties of nanostructured FeSi₂ prepared by field-activated and pressure-assisted reactive sintering, *Journal of Alloys and Compounds* 492(1-2) (2010) 303-306.
- [12] M. Umemoto, Preparation of thermoelectric β -FeSi₂ doped with Al and Mn by mechanical alloying (Overview), *Materials Transactions, JIM* 36(2) (1995) 373-383.
- [13] R. Ware, D. McNeill, Iron disilicide as a thermoelectric generator material, *Proceedings of the Institution of Electrical Engineers, IET*, 1964, pp. 178-182.
- [14] J. Theis, R. Bywalez, S. Küpper, A. Lorke, H. Wiggers, Charge storage in β -FeSi₂ nanoparticles, *Journal of Applied Physics* 117(5) (2015) 054303.
- [15] M.S. Halper, J.C. Ellenbogen, *Supercapacitors: A brief overview*, MITRE Nanosystems Group (2006).
- [16] J.M. Miller, *Ultracapacitor applications*, The Institution of Engineering and Technology 2011.
- [17] G. Goodman, *Ceramic capacitor materials*, Marcel Dekker, New York 1986.
- [18] B. Chu, X. Zhou, K. Ren, B. Neese, M. Lin, Q. Wang, F. Bauer, Q. Zhang, A dielectric polymer with high electric energy density and fast discharge speed, *Science* 313(5785) (2006) 334-336.
- [19] B. Epstein, H. Brooks, The theory of extreme values and its implications in the study of the dielectric strength of paper capacitors, *Journal of Applied Physics* 19(6) (1948) 544-550.

-
- [20] A. Balakrishnan, K. Subramanian, Nanostructured ceramic oxides for supercapacitor applications, CRC Press 2014.
- [21] J.L. Stevens, J.S. Shaffer, J.T. Vandenharm, The service life of large aluminum electrolytic capacitors: effects of construction and application, Industry Applications Conference, 2001. Thirty-Sixth IAS Annual Meeting. Conference Record of the 2001 IEEE, IEEE, 2001, pp. 2493-2499.
- [22] Y.-g. LIU, J.-f. YI, The Influence of Forming Sintering Process on the Electrical Properties of Tantalum Capacitors with Solid Electrolyte, Rare Metals and Cemented Carbides 4 (2008) 004.
- [23] J.W. Kim, T. Wada, S.G. Kim, H. Kato, Sub-micron porous niobium solid electrolytic capacitor prepared by dealloying in a metallic melt, Materials Letters 116 (2014) 223-226.
- [24] J.R. Miller, R. Outlaw, B. Holloway, Graphene double-layer capacitor with ac line-filtering performance, Science 329(5999) (2010) 1637-1639.
- [25] G.-h. Yuan, Z.-h. Jiang, A. Aramata, Y.-z. Gao, Electrochemical behavior of activated-carbon capacitor material loaded with nickel oxide, Carbon 43(14) (2005) 2913-2917.
- [26] C. Niu, E.K. Sichel, R. Hoch, D. Moy, H. Tennent, High power electrochemical capacitors based on carbon nanotube electrodes, Applied physics letters 70(11) (1997) 1480-1482.
- [27] X. Chen, R. Paul, L. Dai, Carbon-based supercapacitors for efficient energy storage, National Science Review 4(3) (2017) 453-489.
- [28] T. Chen, L. Dai, Carbon nanomaterials for high-performance supercapacitors, Materials Today 16(7-8) (2013) 272-280.
- [29] R. Vellacheri, A. Al-Haddad, H. Zhao, W. Wang, C. Wang, Y. Lei, High performance supercapacitor for efficient energy storage under extreme environmental temperatures, Nano Energy 8 (2014) 231-237.
- [30] K. Chen, Y. Yang, K. Li, Z. Ma, Y. Zhou, D. Xue, CoCl₂ designed as excellent pseudocapacitor electrode materials, ACS Sustainable Chemistry & Engineering 2(3) (2013) 440-444.
- [31] T. Brezesinski, J. Wang, S.H. Tolbert, B. Dunn, Ordered mesoporous α -MoO₃ with iso-oriented nanocrystalline walls for thin-film pseudocapacitors, Nature materials 9(2) (2010) 146.
- [32] L. Huang, D. Chen, Y. Ding, S. Feng, Z.L. Wang, M. Liu, Nickel-cobalt hydroxide nanosheets coated on NiCo₂O₄ nanowires grown on carbon fiber paper for high-performance pseudocapacitors, Nano letters 13(7) (2013) 3135-3139.
- [33] J. Xiao, L. Wan, S. Yang, F. Xiao, S. Wang, Design hierarchical electrodes with highly conductive NiCo₂S₄ nanotube arrays grown on carbon fiber paper for high-performance pseudocapacitors, Nano letters 14(2) (2014) 831-838.
- [34] S.-B. Ma, K.-W. Nam, W.-S. Yoon, X.-Q. Yang, K.-Y. Ahn, K.-H. Oh, K.-B. Kim, A novel concept of hybrid capacitor based on manganese oxide materials, Electrochemistry Communications 9(12) (2007) 2807-2811.
- [35] M.S. Hong, S.H. Lee, S.W. Kim, Use of KCl aqueous electrolyte for 2 V manganese oxide/activated carbon hybrid capacitor, Electrochemical and Solid-State Letters 5(10) (2002) A227-A230.
- [36] R.L. Brendel, R.A. Stevenson, C.A. Frysz, H. Zeng, EMI feedthrough filter terminal assembly having surface mounted, internally grounded hybrid capacitor, Google Patents, 2004.
- [37] L. Demarconnay, E. Raymundo-Pinero, F. Béguin, Adjustment of electrodes potential window in an asymmetric carbon/MnO₂ supercapacitor, Journal of Power Sources 196(1) (2011) 580-586.
- [38] I.-H. Kim, J.-H. Kim, B.-W. Cho, Y.-H. Lee, K.-B. Kim, Synthesis and electrochemical characterization of vanadium oxide on carbon nanotube film substrate for pseudocapacitor

applications, *Journal of the electrochemical society* 153(6) (2006) A989-A996.

[39] K. Brezesinski, J. Wang, J. Haetge, C. Reitz, S.O. Steinmueller, S.H. Tolbert, B.M. Smarsly, B. Dunn, T. Brezesinski, Pseudocapacitive contributions to charge storage in highly ordered mesoporous group V transition metal oxides with iso-oriented layered nanocrystalline domains, *Journal of the American Chemical Society* 132(20) (2010) 6982-6990.

[40] H.I. Becker, Low voltage electrolytic capacitor, Google Patents, 1957.

[41] K. Kenmochi, Aluminum electrolytic capacitor and a manufacturing method therefor, Google Patents, 1987.

[42] L. Gu, X. Ruan, M. Xu, K. Yao, Means of eliminating electrolytic capacitor in AC/DC power supplies for LED lightings, *IEEE Transactions on Power Electronics* 24(5) (2009) 1399-1408.

[43] H.X. Zhou, A. Szabo, J.F. Douglas, J.B. Hubbard, A Brownian dynamics algorithm for calculating the hydrodynamic friction and the electrostatic capacitance of an arbitrarily shaped object, *The Journal of chemical physics* 100(5) (1994) 3821-3826.

[44] P.H. Netherwood, L.L. Rice, Electrostatic capacitor, Google Patents, 1962.

[45] N. Ohmatoi, Electrostatic capacitor type sensing device, Google Patents, 1990.

[46] P. Simon, Y. Gogotsi, Materials for electrochemical capacitors, *Nanoscience And Technology: A Collection of Reviews from Nature Journals*, World Scientific 2010, pp. 320-329.

[47] K. Jurewicz, C. Vix-Guterl, E. Frackowiak, S. Saadallah, M. Reda, J. Parmentier, J. Patarin, F. Béguin, Capacitance properties of ordered porous carbon materials prepared by a templating procedure, *Journal of Physics and Chemistry of Solids* 65(2-3) (2004) 287-293.

[48] W. Huang, H. Zhang, Y. Huang, W. Wang, S. Wei, Hierarchical porous carbon obtained from animal bone and evaluation in electric double-layer capacitors, *Carbon* 49(3) (2011) 838-843.

[49] Y. Dong, Z.-S. Wu, W. Ren, H.-M. Cheng, X. Bao, Graphene: a promising 2D material for electrochemical energy storage, *Science Bulletin* 62(10) (2017) 724-740.

[50] J.M. Soon, K.P. Loh, Electrochemical double-layer capacitance of MoS₂ nanowall films, *Electrochemical and Solid-State Letters* 10(11) (2007) A250-A254.

[51] H.v. Helmholtz, Ueber einige Gesetze der Vertheilung elektrischer Ströme in körperlichen Leitern, mit Anwendung auf die thierisch-elektrischen Versuche (Schluss.), *Annalen der Physik* 165(7) (1853) 353-377.

[52] G. Gouy, Sur la fonction électro capillaire *Ann. Phys.* 9 (1917) 129 - 184.

[53] T.F. Young, *Statistical Thermodynamics* (Fowler, R. H.; Guggenheim, E. A.), *Journal of Chemical Education* 18(4) (1941) 198.

[54] B.E. Conway, *Electrochemical supercapacitors: scientific fundamentals and technological applications*, Springer Science & Business Media 2013.

[55] W. Deng, X. Ji, Q. Chen, C.E. Banks, Electrochemical capacitors utilising transition metal oxides: an update of recent developments, *Rsc Advances* 1(7) (2011) 1171-1178.

[56] A. Rudge, J. Davey, I. Raistrick, S. Gottesfeld, J.P. Ferraris, Conducting polymers as active materials in electrochemical capacitors, *Journal of power sources* 47(1-2) (1994) 89-107.

[57] R.N. Reddy, R.G. Reddy, Sol-gel MnO₂ as an electrode material for electrochemical capacitors, *Journal of Power Sources* 124(1) (2003) 330-337.

[58] Z.S. Wu, D.W. Wang, W. Ren, J. Zhao, G. Zhou, F. Li, H.M. Cheng, Anchoring hydrous RuO₂ on graphene sheets for high-performance electrochemical capacitors, *Advanced Functional Materials* 20(20) (2010) 3595-3602.

[59] C. Yuan, L. Yang, L. Hou, J. Li, Y. Sun, X. Zhang, L. Shen, X. Lu, S. Xiong, X.W. Lou, Flexible

hybrid paper made of monolayer Co₃O₄ microsphere arrays on rGO/CNTs and their application in electrochemical capacitors, *Advanced Functional Materials* 22(12) (2012) 2560-2566.

[60] S. Sivakkumar, J.M. Ko, D.Y. Kim, B. Kim, G. Wallace, Performance evaluation of CNT/polypyrrole/MnO₂ composite electrodes for electrochemical capacitors, *Electrochimica Acta* 52(25) (2007) 7377-7385.

[61] D. Belanger, X. Ren, J. Davey, F. Uribe, S. Gottesfeld, Characterization and long-term performance of polyaniline-based electrochemical capacitors, *Journal of the Electrochemical Society* 147(8) (2000) 2923.

[62] W. Tian, X. Mao, P. Brown, G.C. Rutledge, T.A. Hatton, Electrochemically nanostructured polyvinylferrocene/polypyrrole hybrids with synergy for energy storage, *Advanced Functional Materials* 25(30) (2015) 4803-4813.

[63] S. Li, J. Chen, M. Cui, G. Cai, J. Wang, P. Cui, X. Gong, P.S. Lee, A High-Performance Lithium-Ion Capacitor Based on 2D Nanosheet Materials, *Small* 13(6) (2017) 1602893.

[64] K. Kierzek, E. Frackowiak, G. Lota, G. Gryglewicz, J. Machnikowski, Electrochemical capacitors based on highly porous carbons prepared by KOH activation, *Electrochimica Acta* 49(4) (2004) 515-523.

[65] R. Signorelli, D.C. Ku, J.G. Kassakian, J.E. Schindall, Electrochemical double-layer capacitors using carbon nanotube electrode structures, *Proceedings of the IEEE* 97(11) (2009) 1837-1847.

[66] Q. Ke, J. Wang, Graphene-based materials for supercapacitor electrodes—A review, *Journal of Materiomics* 2(1) (2016) 37-54.

[67] H. Wada, S. Nohara, N. Furukawa, H. Inoue, N. Sugoh, H. Iwasaki, M. Morita, C. Iwakura, Electrochemical characteristics of electric double layer capacitor using sulfonated polypropylene separator impregnated with polymer hydrogel electrolyte, *Electrochimica Acta* 49(27) (2004) 4871-4875.

[68] T. Sato, G. Masuda, K. Takagi, Electrochemical properties of novel ionic liquids for electric double layer capacitor applications, *Electrochimica Acta* 49(21) (2004) 3603-3611.

[69] A. Todoroki, H. Shiomi, Y. Mizutani, Y. Suzuki, Electrical Shorting between the Carbon-Fiber Cloth Electrodes of Structural Capacitors with a Glass-Fiber Cloth Separator, *Open Journal of Composite Materials* 4(03) (2014) 140.

[70] F. Liang, K. Hayashi, A high-energy-density mixed-aprotic-aqueous sodium-air cell with a ceramic separator and a porous carbon electrode, *Journal of The Electrochemical Society* 162(7) (2015) A1215-A1219.

[71] H. Watanabe, T. Tatsumi, S. Ohnishi, T. Hamada, I. Honma, T. Kikkawa, A new cylindrical capacitor using hemispherical grained Si (HSG-Si) for 256Mb DRAMs, *IEEE International Electron Devices Meeting, Technical Digest, San Francisco, CA, 1992*, pp. 259-262.

[72] H. Pröbstle, C. Schmitt, J. Fricke, Button cell supercapacitors with monolithic carbon aerogels, *Journal of Power Sources* 105(2) (2002) 189-194.

[73] H.B. Palmer, The capacitance of a parallel-plate capacitor by the Schwartz-Christoffel transformation, *Electrical Engineering* 56(3) (1937) 363-368.

[74] M.S.A. Rahman, S.C. Mukhopadhyay, P.-L. Yu, Novel planar interdigital sensors, *Novel Sensors for Food Inspection: Modelling, Fabrication and Experimentation*, Springer 2014, pp. 11-35.

[75] S. Zheng, Z.-S. Wu, S. Wang, H. Xiao, F. Zhou, C. Sun, X. Bao, H.-M. Cheng, Graphene-based materials for high-voltage and high-energy asymmetric supercapacitors, *Energy Storage Materials* 6 (2017) 70-97.

-
- [76] H. Pan, C.K. Poh, Y.P. Feng, J. Lin, Supercapacitor electrodes from tubes-in-tube carbon nanostructures, *Chemistry of Materials* 19(25) (2007) 6120-6125.
- [77] L.-F. Chen, X.-D. Zhang, H.-W. Liang, M. Kong, Q.-F. Guan, P. Chen, Z.-Y. Wu, S.-H. Yu, Synthesis of nitrogen-doped porous carbon nanofibers as an efficient electrode material for supercapacitors, *ACS nano* 6(8) (2012) 7092-7102.
- [78] M.D. Stoller, S. Park, Y. Zhu, J. An, R.S. Ruoff, Graphene-based ultracapacitors, *Nano letters* 8(10) (2008) 3498-3502.
- [79] C. Zhan, M. Naguib, M. Lukatskaya, P.R. Kent, Y. Gogotsi, D.-e. Jiang, Understanding the MXene pseudocapacitance, *The journal of physical chemistry letters* 9(6) (2018) 1223-1228.
- [80] W.W. Liu, Y.Q. Feng, X.B. Yan, J.T. Chen, Q.J. Xue, Superior micro-supercapacitors based on graphene quantum dots, *Advanced Functional Materials* 23(33) (2013) 4111-4122.
- [81] Q. Jiang, N. Kurra, M. Alhabeb, Y. Gogotsi, H.N. Alshareef, All pseudocapacitive MXene-RuO₂ asymmetric supercapacitors, *Advanced Energy Materials* 8(13) (2018) 1703043.
- [82] Z. Chen, S. Ye, S.D. Evans, Y. Ge, Z. Zhu, Y. Tu, X. Yang, Confined assembly of hollow carbon spheres in carbonaceous nanotube: a spheres-in-tube carbon nanostructure with hierarchical porosity for high-performance supercapacitor, *Small* 14(19) (2018) 1704015.
- [83] C. Qu, Y. Jiao, B. Zhao, D. Chen, R. Zou, K.S. Walton, M. Liu, Nickel-based pillared MOFs for high-performance supercapacitors: design, synthesis and stability study, *Nano Energy* 26 (2016) 66-73.
- [84] C.R. Ryder, J.D. Wood, S.A. Wells, M.C. Hersam, Chemically tailoring semiconducting two-dimensional transition metal dichalcogenides and black phosphorus, *ACS nano* 10(4) (2016) 3900-3917.
- [85] Y. Sun, N. Liu, Y. Cui, Promises and challenges of nanomaterials for lithium-based rechargeable batteries, *Nature Energy* 1(7) (2016) 1-12.
- [86] J. Qiao, X. Kong, Z.-X. Hu, F. Yang, W. Ji, High-mobility transport anisotropy and linear dichroism in few-layer black phosphorus, *Nature communications* 5(1) (2014) 1-7.
- [87] M.R. Lukatskaya, S. Kota, Z. Lin, M.-Q. Zhao, N. Shpigel, M.D. Levi, J. Halim, P.-L. Taberna, M.W. Barsoum, P. Simon, Ultra-high-rate pseudocapacitive energy storage in two-dimensional transition metal carbides, *Nature Energy* 2(8) (2017) 1-6.
- [88] S. Mao, Z. Wen, T. Huang, Y. Hou, J. Chen, High-performance bi-functional electrocatalysts of 3D crumpled graphene-cobalt oxide nanohybrids for oxygen reduction and evolution reactions, *Energy & Environmental Science* 7(2) (2014) 609-616.
- [89] D.W. Wang, F. Li, M. Liu, G.Q. Lu, H.M. Cheng, 3D aperiodic hierarchical porous graphitic carbon material for high-rate electrochemical capacitive energy storage, *Angewandte Chemie International Edition* 47(2) (2008) 373-376.
- [90] L. Zhou, K. Zhang, Z. Hu, Z. Tao, L. Mai, Y.M. Kang, S.L. Chou, J. Chen, Recent developments on and prospects for electrode materials with hierarchical structures for lithium-ion batteries, *Advanced Energy Materials* 8(6) (2018) 1701415.
- [91] X. Cai, M. Peng, X. Yu, Y. Fu, D. Zou, Flexible planar/fiber-architected supercapacitors for wearable energy storage, *Journal of Materials Chemistry C* 2(7) (2014) 1184-1200.
- [92] L. Liu, Z. Niu, L. Zhang, W. Zhou, X. Chen, S. Xie, Nanostructured graphene composite papers for highly flexible and foldable supercapacitors, *Advanced Materials* 26(28) (2014) 4855-4862.
- [93] G. Hasegawa, Monolithic electrode for electric double-layer capacitors based on macro/meso/microporous S-containing activated carbon with high surface area, *Studies on Porous Monolithic Materials Prepared via Sol-Gel Processes*, Springer 2013, pp. 79-89.

-
- [94] C. Koch, T.J. Rinke, *Photolithography: Basics of Microstructuring*, MicroChemicals 2017.
- [95] J.I. Goldstein, D.E. Newbury, J.R. Michael, N.W. Ritchie, J.H.J. Scott, D.C. Joy, *Scanning electron microscopy and X-ray microanalysis*, Springer 2017.
- [96] A. Khursheed, *Scanning electron microscope*, Google Patents, 2007.
- [97] L.A. Giannuzzi, *Introduction to focused ion beams: instrumentation, theory, techniques and practice*, Springer Science & Business Media 2004.
- [98] B.E. Warren, *X-ray Diffraction*, Courier Corporation 1990.
- [99] J.M. Hollander, W.L. Jolly, *X-ray photoelectron spectroscopy*, *Accounts of chemical research* 3(6) (1970) 193-200.
- [100] R. Arrigo, M. Hävecker, M.E. Schuster, C. Ranjan, E. Stotz, A. Knop-Gericke, R. Schlögl, *In situ study of the gas-phase electrolysis of water on platinum by NAP-XPS*, *Angewandte Chemie International Edition* 52(44) (2013) 11660-11664.
- [101] D. Shah, D.I. Patel, S. Bahr, P. Dietrich, M. Meyer, A. Thißen, M.R. Linford, *Liquid water, by near-ambient pressure XPS*, *Surface Science Spectra* 26(2) (2019) 024003.
- [102] P. Van der Heide, *X-Ray photoelectron spectroscopy, An Introduction to Principles and Practices* (2011).
- [103] S. Brunauer, L. Copeland, *Physical adsorption of gases and vapors on solids*, *Symposium on Properties of Surfaces*, ASTM International, 1963.
- [104] T. Dobbelaere, P.M. Vereecken, C. Detavernier, *A USB-controlled potentiostat/galvanostat for thin-film battery characterization*, *HardwareX* 2 (2017) 34-49.
- [105] B. Bozzini, P. Bocchetta, B. Alemán, M. Amati, A. Gianoncelli, L. Gregoratti, H. Sezen, A. Taurino, M. Kiskinova, *Electrodeposition and pyrolysis of Mn/polypyrrole nanocomposites: a study based on soft X-ray absorption, fluorescence and photoelectron microspectroscopies*, *Journal of Materials Chemistry A* 3(37) (2015) 19155-19167.
- [106] D.K. Gosser, *Cyclic voltammetry: simulation and analysis of reaction mechanisms*, VCH New York 1993.
- [107] H.M. Jafari, K. Abdelhalim, L. Soleymani, E.H. Sargent, S.O. Kelley, R. Genov, *Nanostructured CMOS wireless ultra-wideband label-free PCR-free DNA analysis SoC*, *IEEE Journal of Solid-State Circuits* 49(5) (2014) 1223-1241.
- [108] T.M. Nahir, R.A. Clark, E.F. Bowden, *Linear-sweep voltammetry of irreversible electron transfer in surface-confined species using the Marcus theory*, *Analytical Chemistry* 66(15) (1994) 2595-2598.
- [109] T. Schmidt, H. Gasteiger, G. Stäb, P. Urban, D. Kolb, R. Behm, *Characterization of high-surface-area electrocatalysts using a rotating disk electrode configuration*, *Journal of The Electrochemical Society* 145(7) (1998) 2354-2358.
- [110] L. Tsybeskov, S. Duttagupta, P. Fauchet, *Photoluminescence and electroluminescence in partially oxidized porous silicon*, *Solid state communications* 95(7) (1995) 429-433.
- [111] C. Peng, K. Hirschman, P. Fauchet, *Carrier transport in porous silicon light-emitting devices*, *Journal of applied physics* 80(1) (1996) 295-300.
- [112] L. Tsybeskov, S. Duttagupta, K. Hirschman, P. Fauchet, *Stable and efficient electroluminescence from a porous silicon-based bipolar device*, *Applied physics letters* 68(15) (1996) 2058-2060.
- [113] M. Ben-Chorin, F. Möller, F. Koch, *Nonlinear electrical transport in porous silicon*, *Physical Review B* 49(4) (1994) 2981.

-
- [114] S.M. Sze, K.K. Ng, *Physics of semiconductor devices*, John Wiley & Sons 2006.
- [115] J. Frenkel, On pre-breakdown phenomena in insulators and electronic semi-conductors, *Physical Review* 54(8) (1938) 647.
- [116] M. Rafiq, Z. Durrani, H. Mizuta, M. Hassan, S. Oda, Field-dependant hopping conduction in silicon nanocrystal films, *Journal of Applied Physics* 104(12) (2008) 123710.
- [117] F. Yilmaz, *Conducting polymers*, (2016).
- [118] S. Bhattacharyya, A. Laha, S. Krupanidhi, Analysis of leakage current conduction phenomenon in thin SrBi₂Ta₂O₉ films grown by excimer laser ablation, *Journal of applied physics* 91(7) (2002) 4543-4548.
- [119] Y. Liang, Y. Li, H. Wang, J. Zhou, J. Wang, T. Regier, H. Dai, Co₃O₄ nanocrystals on graphene as a synergistic catalyst for oxygen reduction reaction, *Nature materials* 10(10) (2011) 780.
- [120] W. Aigner, M. Wiesinger, H. Wiggers, M. Stutzmann, R.N. Pereira, Three-Dimensional Percolation and Performance of Nanocrystal Field-Effect Transistors, *Physical Review Applied* 5(5) (2016) 054017.
- [121] W. Hu, Z. Wang, Y. Du, X.-X. Zhang, T. Wu, Space-Charge-Mediated Anomalous Ferroelectric Switching in P(VDF-TrEE) Polymer Films, *ACS applied materials & interfaces* 6(21) (2014) 19057-19063.
- [122] R. Pereira, S. Niesar, W. You, A. Da Cunha, N. Erhard, A. Stegner, H. Wiggers, M.-G. Willinger, M. Stutzmann, M. Brandt, Solution-processed networks of silicon nanocrystals: The role of internanocrystal medium on semiconducting behavior, *The Journal of Physical Chemistry C* 115(41) (2011) 20120-20127.
- [123] R. Imlau, E. Mehmedovic, P. Xu, A.A. Stewart, C. Leidinger, R.E. Duninborkowski, G. Bihlmayer, H. Wiggers, R. Carius, U. Kolb, Structural and electronic properties of β -FeSi₂ nanoparticles: The role of stacking fault domains.
- [124] M. Bost, J.E. Mahan, A clarification of the index of refraction of beta-iron disilicide, *Journal of applied physics* 64(4) (1988) 2034-2037.
- [125] E. Arushanov, E. Bucher, C. Kloc, O. Kulikova, L. Kulyuk, A. Siminel, Photoconductivity in n-type β -FeSi₂ single crystals, *Physical Review B* 52(1) (1995) 20.
- [126] C. Spinella, S. Coffa, C. Bongiorno, S. Pannitteri, M. Grimaldi, Origin and perspectives of the 1.54 μ m luminescence from ion-beam-synthesized β -FeSi₂ precipitates in Si, *Applied Physics Letters* 76(2) (2000) 173-175.
- [127] D. Leong, M. Harry, K. Reeson, K. Homewood, On the origin of the 1.5 μ m luminescence in ion beam synthesized β -FeSi₂, *Applied physics letters* 68(12) (1996) 1649-1650.
- [128] K. Lefki, P. Muret, N. Cherief, R. Cinti, Optical and electrical characterization of β -FeSi₂ epitaxial thin films on silicon substrates, *Journal of applied physics* 69(1) (1991) 352-357.
- [129] T. Suemasu, Y. Iikura, T. Fujii, K.i. Takakura, N. Hiroi, F. Hasegawa, Improvement of 1.5 μ m Photoluminescence from Reactive Deposition Epitaxy (RDE) Grown β -FeSi₂ Balls in Si by High Temperature Annealing, *Japanese journal of applied physics* 38(6A) (1999) L620.
- [130] B. Tatar, K. Kutlu, M. Ürgen, Synthesis of β -FeSi₂/Si heterojunctions for photovoltaic applications by unbalanced magnetron sputtering, *Thin Solid Films* 516(1) (2007) 13-16.
- [131] M. Powalla, K. Herz, Co-evaporated thin films of semiconducting β -FeSi₂, *Applied surface science* 65 (1993) 482-488.
- [132] N. Dahal, V. Chikan, Phase-controlled synthesis of iron silicide (Fe₃Si and FeSi₂) nanoparticles in solution, *Chemistry of Materials* 22(9) (2010) 2892-2897.

-
- [133] P. Schaaf, M. Milosavljevic, S. Dhar, N. Bibic, K.-P. Lieb, M. Wölz, G. Principi, Mössbauer Optimization of the Direct Synthesis of β -FeSi₂ by Ion Beam Mixing of Fe/Si Bilayers, *Hyperfine interactions* 139(1-4) (2002) 615-621.
- [134] I. Goldfarb, F. Cesura, M. Dascalu, Magnetic Binary Silicide Nanostructures, *Advanced Materials* 30(41) (2018) 1800004.
- [135] A. Heinrich, H. Griessmann, G. Behr, K. Ivanenko, J. Schumann, H. Vinzelberg, Thermoelectric properties of β -FeSi₂ single crystals and polycrystalline β -FeSi_{2+x} thin films, *Thin Solid Films* 381(2) (2001) 287-295.
- [136] Y. Qiu, H.-L. Shen, Y.-G. Yin, K.-H. Wu, Fabrication and thermoelectric properties of β -FeSi₂ prepared by mechanical alloying, *Transactions of Nonferrous Metals Society of China* 17(s1B) (2007) s618-s621.
- [137] L. Han, T. Xin-Feng, C. Wei-Qiang, Z. Qing-Jie, Quick preparation and thermal transport properties of nanostructured β -FeSi₂ bulk material, *Chinese Physics B* 18(1) (2009) 287.
- [138] H. Nagai, S. Katsuyama, S. Nakayama, H. Kobayashi, K. Majima, M. Ito, Effects of mechanical alloying and copper addition on thermoelectric properties of n-type and p-type β -FeSi₂, *Materials Transactions, JIM* 39(4) (1998) 515-521.
- [139] M. Naito, M. Ishimaru, Formation process of β -FeSi₂ from amorphous Fe-Si synthesized by ion implantation: Fe concentration dependence, *Journal of microscopy* 236(2) (2009) 123-127.
- [140] T. Ootsuka, Z. Liu, M. Osamura, Y. Fukuzawa, N. Otagawa, Y. Nakayama, H. Tanoue, Y. Makita, β -FeSi₂ based metal-insulator-semiconductor devices formed by sputtering for optoelectronic applications, *Materials Science and Engineering: B* 124 (2005) 449-452.
- [141] J.M. Higgins, A.L. Schmitt, S. Jin, Transition Metal Silicide Nanowires: Synthetic Methods and Applications, *Silicon and Silicide Nanowires: Applications, Fabrication, and Properties* (2016) 59.
- [142] T. Kameyama, K. Sakanaka, H. Arakawa, A. Motoe, T. Tsunoda, K. Fukuda, Preparation of ultrafine Fe-Si-C powders in a radio-frequency thermal plasma and their catalytic properties, *Journal of materials science* 28(17) (1993) 4630-4636.
- [143] J. Wang, S. Ji, K. Mimura, Y. Sato, S. Song, H. Yamane, M. Shimada, M. Isshiki, Growth of β -FeSi₂ single crystals by the chemical vapor transport method, *physica status solidi (a)* 201(13) (2004) 2905-2909.
- [144] C. Kloc, E. Arushanov, M. Wendl, H. Hohl, U. Malang, E. Bucher, Preparation and properties of FeSi, α -FeSi₂ and β -FeSi₂ single crystals, *Journal of Alloys and Compounds* 219(1-2) (1995) 93-96.
- [145] U. Starke, W. Weiss, M. Kutschera, R. Bandorf, K. Heinz, High quality iron silicide films by simultaneous deposition of iron and silicon on Si (111), *Journal of applied physics* 91(9) (2002) 6154-6161.
- [146] R. Bywalez, H. Orthner, E. Mehmedovic, R. Imlau, A. Kovacs, M. Luysberg, H. Wiggers, Direct gas-phase synthesis of single-phase β -FeSi₂ nanoparticles, *Journal of nanoparticle research* 15(9) (2013) 1878.
- [147] E.L. Petersen, M.W. Crofton, Measurements of high-temperature silane pyrolysis using SiH₄ IR emission and SiH₂ laser absorption, *The Journal of Physical Chemistry A* 107(50) (2003) 10988-10995.
- [148] D. Woiki, A. Giesen, P. Roth, A shock tube study on the thermal decomposition of Fe (CO)₅, *Proc. Int. Symp. Shock Waves*, 2001, p. 253.
- [149] J.Z. Wen, C.F. Goldsmith, R.W. Ashcraft, W.H. Green, Detailed kinetic modeling of iron nanoparticle synthesis from the decomposition of Fe (CO)₅, *The Journal of Physical Chemistry C*

111(15) (2007) 5677-5688.

[150] R.D. Deegan, O. Bakajin, T.F. Dupont, G. Huber, S.R. Nagel, T.A. Witten, Capillary flow as the cause of ring stains from dried liquid drops, *Nature* 389(6653) (1997) 827-829.

[151] S. Manabe, R.T. Wetherald, Thermal equilibrium of the atmosphere with a given distribution of relative humidity, *Journal of the Atmospheric Sciences* 24(3) (1967) 241-259.

[152] G.W. Gee, J.W. Bauder, Particle-size analysis 1, Soil Science Society of America, American Society of Agronomy 1986.

[153] D. Kroetsch, C. Wang, Particle size distribution, Soil sampling and methods of analysis 2 (2008).

[154] J.I. Langford, A. Wilson, Scherrer after sixty years: a survey and some new results in the determination of crystallite size, *Journal of applied crystallography* 11(2) (1978) 102-113.

[155] T. Ungar, Microstructural parameters from X-ray diffraction peak broadening, *Scripta Materialia* 51(8) (2004) 777-781.

[156] A. Ishizaka, S. Iwata, Si-SiO₂ interface characterization from angular dependence of x-ray photoelectron spectra, *Applied Physics Letters* 36(1) (1980) 71-73.

[157] M. Seah, W. Dench, *Surf. Interface Anal.* (1979).

[158] S. Brunauer, L.S. Deming, W.E. Deming, E. Teller, On a theory of the van der Waals adsorption of gases, *Journal of the American Chemical Society* 62(7) (1940) 1723-1732.

[159] F. Zhang, C. Yuan, X. Lu, L. Zhang, Q. Che, X. Zhang, Facile growth of mesoporous Co₃O₄ nanowire arrays on Ni foam for high performance electrochemical capacitors, *Journal of Power Sources* 203 (2012) 250-256.

[160] D. Do, H. Do, Effects of adsorbate–adsorbate interaction in the description of adsorption isotherm of hydrocarbons in micro–mesoporous carbonaceous materials, *Applied surface science* 196(1-4) (2002) 13-29.

[161] M. Lu, *Supercapacitors: materials, systems, and applications*, John Wiley & Sons 2013.

[162] M. Rafiq, Y. Tsuchiya, H. Mizuta, S. Oda, S. Uno, Z. Durrani, W. Milne, Charge injection and trapping in silicon nanocrystals, *Applied Physics Letters* 87(18) (2005) 182101.

[163] P. Mark, W. Helfrich, Space-charge-limited currents in organic crystals, *Journal of Applied Physics* 33(1) (1962) 205-215.

[164] N.F.G. Mott, R. W., *Electronic Processes in Ionic Crystals*, (1950).

[165] H.T. Henderson, K. Ashley, Space-charge-limited current in neutron-irradiated silicon, with evidence of the complete lampert triangle, *Physical Review* 186(3) (1969) 811.

[166] R. Smith, A. Rose, Space-charge-limited currents in single crystals of cadmium sulfide, *Physical Review* 97(6) (1955) 1531.

[167] M. Lampert, A. Rose, R. Smith, Space-charge-limited currents as a technique for the study of imperfections in pure crystals, *Journal of Physics and Chemistry of Solids* 8 (1959) 464-466.

[168] R.H. Bube, Trap density determination by space-charge-limited currents, *Journal of Applied Physics* 33(5) (1962) 1733-1737.

[169] W. Ruppel, Space-charge-limited currents in zinc sulphide single crystals, *Helvetica Physica Acta* 31 (1958) 311.

[170] B.L. Gregory, A.G. Jordan, Experimental investigations of single injection in compensated silicon at low temperatures, *Physical Review* 134(5A) (1964) A1378.

[171] G. Zuo, M. Linares, T. Upreti, M. Kemerink, General rule for the energy of water-induced traps in organic semiconductors, *Nature materials* 18(6) (2019) 588.

-
- [172] O. Björneholm, M.H. Hansen, A. Hodgson, L.-M. Liu, D.T. Limmer, A. Michaelides, P. Pedevilla, J. Rossmeisl, H. Shen, G. Tocci, Water at interfaces, *Chemical reviews* 116(13) (2016) 7698-7726.
- [173] A. Verdager, C. Weis, G. Oncins, G. Ketteler, H. Bluhm, M. Salmeron, Growth and structure of water on SiO₂ films on Si investigated by kelvin probe microscopy and in situ x-ray spectroscopies, *Langmuir* 23(19) (2007) 9699-9703.
- [174] P.K. Gupta, M. Meuwly, Dynamics and vibrational spectroscopy of water at hydroxylated silica surfaces, *Faraday discussions* 167 (2013) 329-346.
- [175] J.S. D'Arrigo, Screening of membrane surface charges by divalent cations: an atomic representation, *American Journal of Physiology-Cell Physiology* 235(3) (1978) C109-C117.
- [176] Y. Wang, Y. Song, Y. Xia, Electrochemical capacitors: mechanism, materials, systems, characterization and applications, *Chemical Society Reviews* 45(21) (2016) 5925-5950.
- [177] G. Birnbaum, S. Chatterjee, The dielectric constant of water vapor in the microwave region, *Journal of Applied Physics* 23(2) (1952) 220-223.
- [178] M. Areir, Y. Xu, D. Harrison, J. Fyson, R. Zhang, Development of 3D printing technology for the manufacture of flexible electric double-layer capacitors, *Materials and Manufacturing Processes* 33(8) (2018) 905-911.
- [179] J. Lin, J. Wu, Z. Yang, M. Pu, Synthesis and properties of poly (acrylic acid)/mica superabsorbent nanocomposite, *Macromolecular Rapid Communications* 22(6) (2001) 422-424.
- [180] J.-H. Lee, U. Paik, V.A. Hackley, Y.-M. Choi, Effect of poly (acrylic acid) on adhesion strength and electrochemical performance of natural graphite negative electrode for lithium-ion batteries, *Journal of Power Sources* 161(1) (2006) 612-616.
- [181] B. Koo, H. Kim, Y. Cho, K.T. Lee, N.S. Choi, J. Cho, A highly cross-linked polymeric binder for high-performance silicon negative electrodes in lithium ion batteries, *Angewandte Chemie* 124(35) (2012) 8892-8897.
- [182] N. Marković, T. Schmidt, V. Stamenković, P. Ross, Oxygen reduction reaction on Pt and Pt bimetallic surfaces: a selective review, *Fuel cells* 1(2) (2001) 105-116.
- [183] M. Gong, D.-Y. Wang, C.-C. Chen, B.-J. Hwang, H. Dai, A mini review on nickel-based electrocatalysts for alkaline hydrogen evolution reaction, *Nano Research* 9(1) (2016) 28-46.
- [184] T.L. Barr, S. Seal, Nature of the use of adventitious carbon as a binding energy standard, *Journal of Vacuum Science & Technology A: Vacuum, Surfaces, and Films* 13(3) (1995) 1239-1246.
- [185] J.F. Moulder, Handbook of X-ray photoelectron spectroscopy, *Physical electronics* (1995) 230-232.

10 List of graphs

Figure 1.1 Global electric car sales by key markets, 2010-2020. (IEA analysis based on IEA data and EV-Volumes (2020)). The light blue color represents the sales in China, and purple represents the USA, green represents Europe, yellow represents Japan, and the orange color represents the worldwide sales [5].	1
Figure 3.1 There are three types of capacitors, including the electrolytic, electrochemical, and electrostatic capacitors. The electrochemical capacitors have two categories, double-layer capacitor and pseudocapacitor, and the combination of these two types is called the hybrid capacitor.	5
Figure 3.2 The electrostatic capacitor's configuration, which includes a positively charged conductive electrode and a negative charged conductive electrode with a non-conducting dielectric.	6
Figure 3.3 The electrolytic capacitor's configuration with the aluminum foil as the anode and its aluminum oxide layer as the dielectric. Unlike other capacitors, the liquid or solid electrolyte works as the cathode electrode in the electrolytic capacitor.	6
Figure 3.4 The configuration of the electric double-layer capacitor. The black-shaped material covering the current collectors is the materials with large specific surface area, such as graphene [24], activated carbon [25], and carbon nanotube [26].	7
Figure 3.5 Helmholtz model (left), Gouy-Chapman model (middle) and Gouy-Chapman- Stern model (right) [54].	8
Figure 3.6 The schematic diagram of the interdigitated pattern, produced via lithography. The size of the overall interdigitated pattern is on a scale of several millimeters. The width of each finger of the interdigitated electrode can be several micrometers.	10
Figure 3.7 The flow chart of the lithography process, including photoresist coating, exposing and developing. It briefly explains how the positive photoresist and the negative photoresist work differently.	12
Figure 3.8 The mask Aligner (Karl Süss) is used to transfer the pattern from the mask to the substrate.	13
Figure 3.9 The schematic graph of a photomask with a simple pattern, formed by three transparent areas and Cr thin-film area.	13
Figure 3.10 The evaporator BOC-Edwards Auto 500.	14
Figure 3.11 Left: Kulicke & Soffa 4123 Wedge Bonder. Right: The schematic graph showing how the gold interdigitated pattern is connected to the chip carrier.	15
Figure 3.12 The photo of Scanning Electron Microscope (Inspect F, FEI).	16
Figure 3.13 The photo of the focused ion beam machine (Helios NANO LAB).	16
Figure 3.14 The schematic diagram of the incident waves and their corresponding atomic diffraction waves on the crystal planes.	17
Figure 3.15 Schematic graph of photoelectron emission irradiated by X-ray.	18
Figure 3.16 Galvanostatic test of thin-film batteries as an example [104]. The red horizontal line represents the applied current (left), and the blue curved line is the measured potential (right).	20
Figure 3.17 The current transient over time $I(t)$ of a capacitor's potentiostat measurement (at a particular applied potential). The current transient behaves exponentially, and the area filled with the horizontal bars represents the stored charge Q .	20
Figure 3.18 Single-cycle of cyclic voltammetry scan shows how the applied voltage varies with	

time (left). The cyclic voltammetry curve of the applied voltage-dependent current (right). The blue arrows indicate the direction of the scanning voltage [107].	21
Figure 3.19 The two basic R-C circuits: series circuit (a) and parallel circuit (b).	22
Figure 4.1 The cell structure of β -FeSi ₂ crystal [133, 134]. The purple spheres are Fe ions, and the green spheres are Si ions.	25
Figure 4.2 The Fe-Si binary phase diagram [145].	26
Figure 4.3 The hot-wall reactor for the direct gas-phase synthesis of β -FeSi ₂ , including the gas delivery pipelines (top), the hot-wall reactor (middle), and a particle collecting tube with the powder separator and the particles collecting bottle (right-down). Dr. Hans Orthner provides this graph.	27
Figure 5.1 The structure of Cr coated photomask and the standard size of the pattern. The dark area is the area coated with Cr, and the light area is the transparent quartz substrate, with no Cr covered.	29
Figure 5.2 The interdigitated capacitor's schematic figure from Top view (top) and the side view (down). The golden color indicates that the interdigitated electrodes are positively charged, and the gray color indicates the electrodes are negatively charged.	30
Figure 5.3 (a) A microscope image of the gold interdigitated structure on the silica substrate and (b) the photo of an assembled β -FeSi ₂ micro capacitor.	31
Figure 5.4 Parallel-plate quartz electrode coated with 50 nm Au layer, and then 60 μ g β -FeSi ₂ spin-coated on top (left). The microscope photo of β -FeSi ₂ ink, magnified 10 times (right).	32
Figure 5.5 The double-plate capacitor configuration, with two double plates coated with gold as electrodes and a sheet of porous glass fiber as a separator.	32
Figure 5.6 The experimental setup configuration, with a sealed chamber where capacitors locate, a source measure unit that provides the voltage (current) and measures the output, and a computer that controls the whole setup with LabView software.	33
Figure 5.7 Relative humidity is measured in the sealed container, which varies along with the time and gets stable after a particular time. The real-time temperature is measured and recorded together with the relative humidity.	33
Figure 6.1 Scanning electron spectroscopy of as-synthesized β -FeSi ₂ nanoparticles, the scale bar is 500 nm. The figure shows that the β -FeSi ₂ nanoparticles have a sponge-like shape. The rough size of the nanoparticles (in the scale of tens of nanometers) can be thus estimated.	36
Figure 6.2 Histogram with size distribution. The particle distribution analysis achieved from the SEM spectroscopy, showing that the particle size distribution of the β -FeSi ₂ nanoparticles conforms to the law of normal distribution, and the particle size distributes from 20 nm to 70 nm, with the most considerable portion of the β -FeSi ₂ NPs' size ranging between 25 nm and 50 nm.	37
Figure 6.3 The X-ray diffraction pattern of the as-synthesized NPs with the typical characteristic peaks of β -FeSi ₂ NPs noted as (202/220)(313)(422)(024)(224), proves that β -FeSi ₂ NPs can be successfully synthesized at a SiH ₄ : Fe(CO) ₅ ratio of 2.6:1.	37
Figure 6.4 The experimental (black) and fitted (red) X-ray photoelectron spectrum of Si. The peaks of the experimental spectrum of β -FeSi ₂ NPs can be divided and fitted into the peaks of SiO ₂ , FeSi ₂ , and elemental Si.	38
Figure 6.5 The experimental (black) and the fitted (blue and green) X-ray photoelectron spectrum of O.	39
Figure 6.6 The X-ray Photoelectron Spectroscopy of β -FeSi ₂ NPs, measured with Al K α X-rays and Mg K α X-rays, respectively, proving the core-shell structure of the β -FeSi ₂ NPs, with a thin layer of	

Si/SiO ₂ covering the β -FeSi ₂ sphere NPs.	39
Figure 6.7 The inelastic mean free path (IMFP) curve of electrons in elements as a function of excited electron energy [157].	40
Figure 6.8 The adsorption isotherm plot of β -FeSi ₂ NPs, showing that the β -FeSi ₂ nanoparticles are non-porous nanomaterials.	40
Figure 6.9 The schematic drawing of tested spots on the micro capacitor, A (center), B (half center), and C (near the edge).	41
Figure 6.10 The top view SEM graph of the micro capacitor (a) and the cross-section SEM graph (b) of β -FeSi ₂ nanoparticle thin film on the interdigitated structure. The darker part in (b) is the Si substrate.	42
Figure 6.11 The loading mass of β -FeSi ₂ dependent thin-film thickness at different positions A, B, and C follows a linear correlation.	42
Figure 6.12 The arithmetic mean value of the thickness (at the same position spot A/B of the thin-film) of different β -FeSi ₂ loading mass (40 μ g, 60 μ g and 80 μ g), indicating a positive linear correlation. The average thickness of multiple capacitors achieves the data, the error bar shows the variability of data.	43
Figure 6.13 The porosity of β -FeSi ₂ thin-film coated on the substrate, calculated with ImageJ. The red area represents the gaps between nanoparticles, and the gray areas are the nanoparticles.	43
Figure 6.14 The cyclic voltammetry plot of the β -FeSi ₂ capacitor, measured at a scanning rate of 1 mv/s, from 0 V to 4.5 V.	44
Figure 6.15 Typical I(t) curve of β -FeSi ₂ nanoparticle film in the charge and discharge process. The applied charging voltage ranges from 0.2 V to 3 V. The color scale on the right side indicates that different colors correspond to varying voltages in the figure.	45
Figure 6.16 Typical I(t) curve of β -FeSi ₂ nanoparticle film in the charging (3 V) and discharging process, under 100%RH of water vapor in the tested atmosphere. The area of the region filled with a dashed horizontal line is the stored charge.	46
Figure 6.17 Redline: Stored charge-applied charging voltage (Q-V) plot of β -FeSi ₂ micro capacitor at different charging voltage (0.1 V – 3 V). Blackline: Stored charge – applied charging voltage (Q-V) plot of the bare electrode without NPs under the same condition (100% RH of water vapor).	47
Figure 6.18 The stored charge of the capacitor measured in the air saturated with water vapor (black line) and in dry air (blue line), respectively, showing that the capacitance tested in the air saturated with water vapor is dramatically higher than in dry air.	47
Figure 6.19 The interdigitated capacitor's cyclic performance with β -FeSi ₂ , at a charging voltage of 3 V, for 140 cycles, showing high retention of the capacitance.	48
Figure 6.20 The Galvanostatic curve V (t), charge at a constant current of 0.1 μ A. The voltage is measured during the charging process, and the open-circuit voltage is measured as well.	49
Figure 6.21 Voltage - time plot of galvanostatic test of different charging current (0.04 μ A, 0.06 μ A, 0.08 μ A, 0.10 μ A, 0.12 μ A, 0.14 μ A, 0.16 μ A, 0.18 μ A, 0.2 μ A, and 0.22 μ A).	49
Figure 6.22 The plot of the charging current dependent V _{gc} of the galvanostatic measurement, showing a gradual growth of the voltage value.	50
Figure 6.23 The V _{dg} versus the charging current plot of galvanostatic measurement, showing a stable trend of the current.	50
Figure 6.24 The plot of the current transient charged at 3 V. The starting charging point I _{c1} ,	

the ending charging point I_{c2} , and starting discharging point I_{d1} and ending discharging point of the transient I_{d2} is marked with red dots in this figure, separately.	51
Figure 6.25 Plot of the voltage-dependent steady-state current I_{c2} of the interdigitated capacitor coated with β -FeSi ₂ thin film, which is measured in the dry air.	51
Figure 6.26 Dependence of the steady-state current I_{c2} on the applied voltage (up to 3 V), measured on the interdigitated capacitor at the ambient atmosphere. Red lines represent numerical fits of the experimental data.	52
Figure 6.27 The plot of steady-state current I_{c2} versus the applied voltage (0.1 V to 3 V) in the air saturated with water vapor (100% RH)	52
Figure 6.28 Double logarithmic plot of charging ending point I_{c2} versus charging voltage. The Red line (below 1 V) represents the Ohmic regime, the green line (1.1 V to 1.9 V) describes the SCLC regime, and the yellow line (2 V to 3 V) represents the SCLC regime with traps.	53
Figure 6.29 The Schematic graph of air with saturated water vapor (100% RH)/ β -FeSi ₂ interface, more than 3 nm of the water thin film [173] is formed (around ten layers of water molecules). Red spots represent oxygen atoms, and blue spots represent hydrogen atoms.	54
Figure 6.30 The Schematic graph of the charge distribution on nanoparticles while charging in the air saturated water vapor.	55
Figure 6.31 Bi-exponential fit with charge and discharge current transient, in which the charging voltage is 3 V. The charging process has two time constants τ_1 (0.7 s) and τ_2 (14.7 s), and the discharging process τ_1' (1.1 s) and τ_2' (14.3 s).	56
Figure 6.32 The Schematic graph of the charge distribution on nanoparticles while charging in the air saturated water vapor. The electrostatic capacitance exists between two nanoparticles with opposite charges (Red dashed line). The electric double-layer capacitance exists on the interface of β -FeSi ₂ /H ₂ O (Green dashed line).	56
Figure 6.33 The equivalent circuit model of the multi pairs of the adjacent-nanoparticle micro capacitor.	57
Figure 6.34 The configuration of a real parallel-plate capacitor (above) and the schematic structure of a parallel plate capacitor (down).	58
Figure 6.35 The in-situ oxygen sensing system (Left). The oxygen-sensing system's schematic components (right) consist of an oxygen sensor, a sample chamber where the interdigitated capacitor locates and a water chamber that the nitrogen gas can go through.	59
Figure 6.36 The plot of oxygen concentration versus time. The whole testing process includes three steps: I, no voltage is applied for the first ten minutes. II, 3 V is applied for the next 10 minutes. III, Stop applying voltage and wait another 10 minutes.	59
Figure 6.37 The oxygen concentration measured at a different applied voltage (2 V to 3.75 V) of the β -FeSi ₂ interdigitated capacitor.	60
Figure 6.38 The steady-state charged current I_{c2} -Voltage plot of β -FeSi ₂ capacitor. The applied voltage ranges from 2 V to 3.75 V.	60
Figure 6.39 The charge-voltage plot of a parallel plate capacitor with β -FeSi ₂	62
Figure 6.40 Specific charge of a parallel-plate capacitor, compared with an interdigitated capacitor.	63
Figure 6.41 Cyclic Voltammetry of double plate capacitor with β -FeSi ₂ nanoparticles	63
Figure 6.42 The series resistance of β -FeSi ₂ parallel-plate capacitor.	64
Figure 6.43 The stored charge of the parallel-plate capacitor with SiO ₂ nanoparticles.	64

Figure 6.44	Stored charge comparison between β -FeSi ₂ and SiO ₂ (both in parallel plate capacitor configuration).	65
Figure 6.45	The series resistance of the SiO ₂ parallel-plate capacitor.....	65
Figure 6.46	The stored charge-applied voltage plot of a parallel plate capacitor with B-doped Si.	66
Figure 6.47	The series resistance (V/I_{c2}) of the B-doped silicon capacitor, with a sharp decreasing trend before 1 V and a gentle decrease afterward.	66
Figure 6.48	Stored charge dependence on the loading mass of β -FeSi ₂ nanoparticles coated interdigitated capacitor.....	67
Figure 6.49	Stored charge dependence on the parallel plate capacitor's loading mass coated with β -FeSi ₂ nanoparticles.	67
Figure 6.50	The molecular structure of polyacrylic acid.	68
Figure 6.51	The microscope graph of the micro capacitor coated with 60 μ g β -FeSi ₂ and 20 wt.% PAA.	69
Figure 6.52	Charge storage of capacitor with different PAA concentrations in the air saturated water vapor (100% RH).....	69
Figure 6.53	Different PAA concentration-dependent series resistance R_{c2} of the interdigitated capacitor coated with β -FeSi ₂ nanoparticles.	70
Figure 6.54	Different PAA concentration-dependent series resistance R_{c1} of the interdigitated capacitor coated with β -FeSi ₂ nanoparticles.	70
Figure 8.1	Charge storage in saturated acetone vapor (Left). Charge storage in saturated water-acetone mixture vapor (Right).....	73
Figure 8.2	Parallel capacitor with KOH additive (Left). The exfoliation condition of gold-coated plate electrode with KOH additive (right).....	74
Figure 11.1	The oxygen evolution reaction plot in 1 M KOH solution.....	91
Figure 11.2	The hydrogen evolution reaction plot in 1 M KOH solution	92
Figure 11.3	Repeat of OER(left) and HER(right) test	92
Figure 11.4	The surface electronic state of C. (a) As-prepared β -FeSi ₂ nanoparticle. (b) β -FeSi ₂ nanoparticle after 7 h electric test of β -FeSi ₂ nanoparticle. (c) β -FeSi ₂ nanoparticle after 168 h electric test of β -FeSi ₂ nanoparticle.	93
Figure 11.5	The surface electronic state of Fe (left) and O (right). (a) As-prepared β -FeSi ₂ nanoparticle. (b) β -FeSi ₂ nanoparticle after 7 h electric test of β -FeSi ₂ nanoparticle. (c) β -FeSi ₂ nanoparticle after 168 h electric test of β -FeSi ₂ nanoparticle.....	94
Figure 11.6	The surface electronic state of Si. (a) As-prepared β -FeSi ₂ nanoparticle. (b) β -FeSi ₂ nanoparticle after 7 h electric test of β -FeSi ₂ nanoparticle. (c) β -FeSi ₂ nanoparticle after 168 h electric test of β -FeSi ₂ nanoparticle.	94
Figure 11.7	Oxygen concentration at a different applied voltage of B-Si capacitor	95



11 Appendix

11.1 Oxygen evolution and hydrogen evolution test

Based on the fact that water can split at 1.23 V (versus RHE), theoretically, there is a hypothesis that water splitting might happen in the applied voltage range (0.1 V to 3 V). Water splitting (water electrolysis) is composed of two half-reactions, i.e., oxygen evolution reaction (OER) and hydrogen evolution reaction (HER). Oxygen evolution reaction is the electrochemical process of producing oxygen (O_2) out of water. The half-reaction of OER in the neutral electrolyte is shown in Equation 11.1.



To prove the hypothesis and further test the water splitting property of β -FeSi₂, linear sweep voltammetry is employed, and the measuring method is introduced in Section 3.4.4. In the linear sweep voltammetry experiment of β -FeSi₂ powder, a typical oxygen evolution reaction plot, as literature[182] shows, is achieved and plotted in Figure 11.1. As the applied voltage increases, a large number of oxygen bubbles can be observed during the measurement. This shows that β -FeSi₂ is an oxygen evolution electrochemical catalyst, which can split water at a specific voltage (verse RHE, Reversible Hydrogen Electrode). The measurement is carried out in a 1 M KOH solution and the scanning rate is at 0.5 mV/s. Usually, the corresponding voltage of the current density of 10 mA/cm² represents the potential as an electrocatalyst. The lower the corresponding voltage, the better performance of materials as an electrocatalyst. Figure 11.1 shows that the applied voltage at ten mA/cm² is 2.29 V (versus RHE).

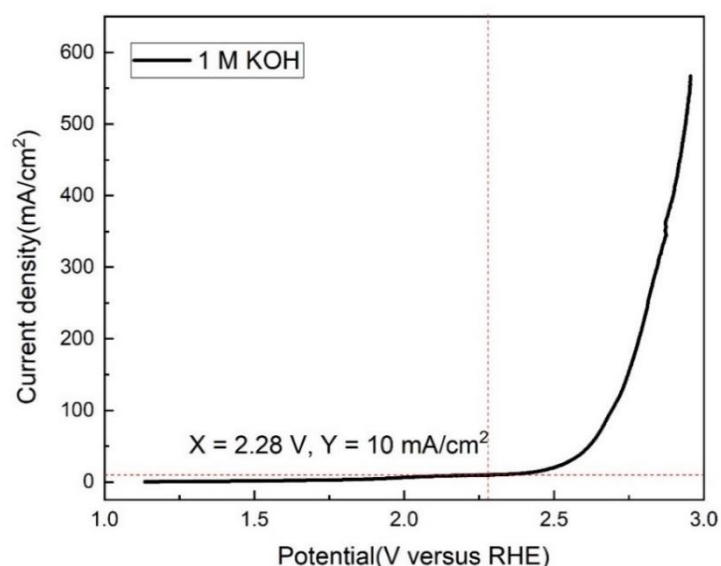


Figure 11.1 The oxygen evolution reaction plot in 1 M KOH solution

While the other half-reaction of water electrolysis is the oxygen evolution reaction, which is the electrochemical process of generating hydrogen (H_2) out of water splitting. A typical hydrogen

evolution reaction plot as literature[183] is achieved at the voltage range of hydrogen evolution reaction (HER), with hydrogen bubbles observed. It shows β -FeSi₂'s ability as a hydrogen evolution catalyst, the corresponding voltage at a current density of 10 mA/cm² is -0.95 V (versus RHE) (Figure 11.2).

The half-reaction of HER is listed below.

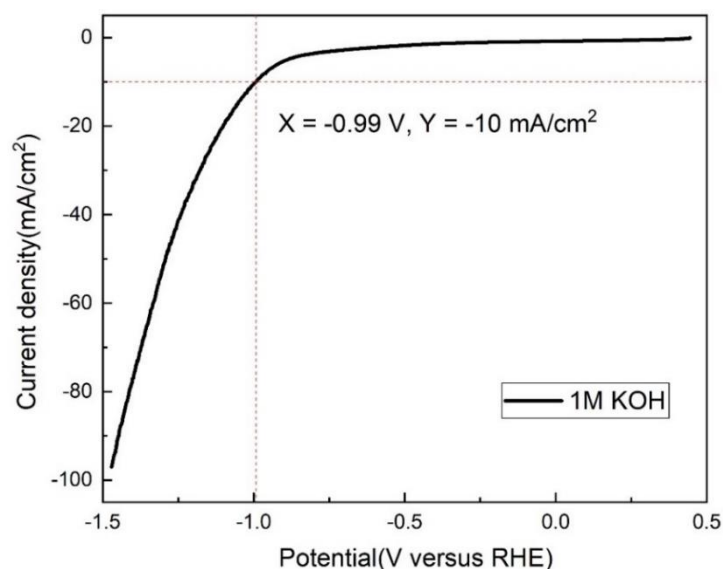


Figure 11.2 The hydrogen evolution reaction plot in 1 M KOH solution

The OER and HER test are repeated ten times each. The high level of overlapping shows the stability of β -FeSi₂ as an electrocatalyst in Figure 11.3.

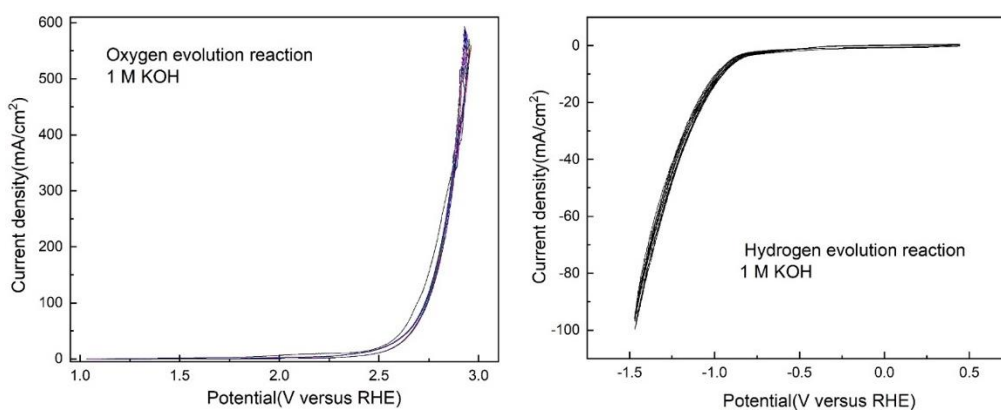


Figure 11.3 Repeat of OER(left) and HER(right) test

It is noticed that no oxygen evolution reaction (OER) or hydrogen evolution reaction (HER) is observed in the LSV plot, which agrees well with the CV plot. Oxygen evolution reaction and hydrogen evolution reaction are the reverse reactions of oxygen evolution reaction and hydrogen evolution reaction. During such a process, hydrogen and oxygen react and form water molecules. The above measurement shows that β -FeSi₂ only works as OER and HER catalyst, and the charging and discharging process is an irreversible reaction.

11.2 X-ray photoelectron spectroscopy (XPS)

To figure out whether there is any chemical reaction taking place, X-ray photoelectric spectrometry (XPS) is conducted before and after the electric measurement is shown below. The capacitor is charged and discharged for multiple cycles. Each cycle includes charging at 3 V for 2 min and discharging for 5 min. After 7 hours and 168 hours of cycles, XPS measurements are taken simultaneously on the thin β -FeSi₂ film of the micro capacitor.

Carbon on specimen surface is almost unavoidable due to the exposure to air. Thus, the C 1s line of adventitious hydrocarbon on the specimen surface at a binding energy of 284.8 eV is frequently used as a calibration standard[184]. The C 1s line of different XPS measurements (Figure 11.4) is adjusted, and then the rest of the peaks of Fe, O, and Si (Figure 11.5 and Figure 11.6) should be moved simultaneously with the C 1s line. The as-prepared capacitor is first measured with XPS, and the XPS spectra are noted as “Before measurement” sample. C 1s line spectra under different conditions are smoothed and compared in Figure 11.4.

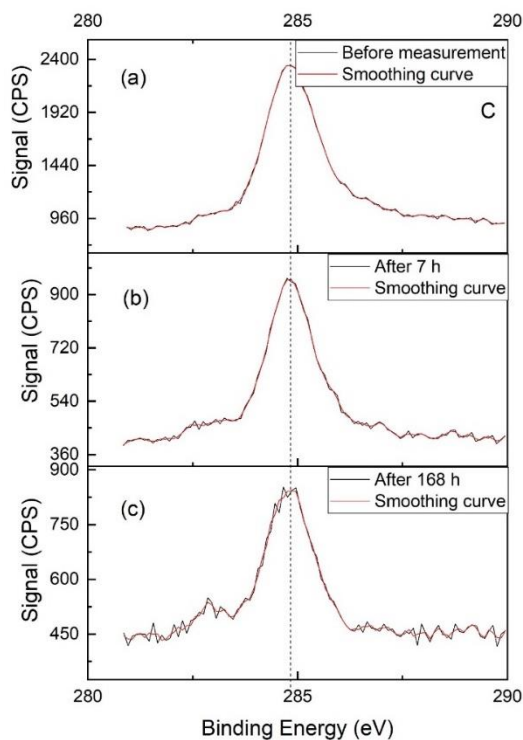


Figure 11.4 The surface electronic state of C. (a) As-prepared β -FeSi₂ nanoparticle. (b) β -FeSi₂ nanoparticle after 7 h electric test of β -FeSi₂ nanoparticle. (c) β -FeSi₂ nanoparticle after 168 h electric test of β -FeSi₂ nanoparticle.

After C 1s calibration, the X-ray photoelectron spectra of Fe (Fe-Si bond) and O (Si-O bond) (before electric measurement, after 7 hours and 168 hours measurement) shows no peak shift in Figure 11.5, indicating no chemical adsorption takes place during charge and discharge process.

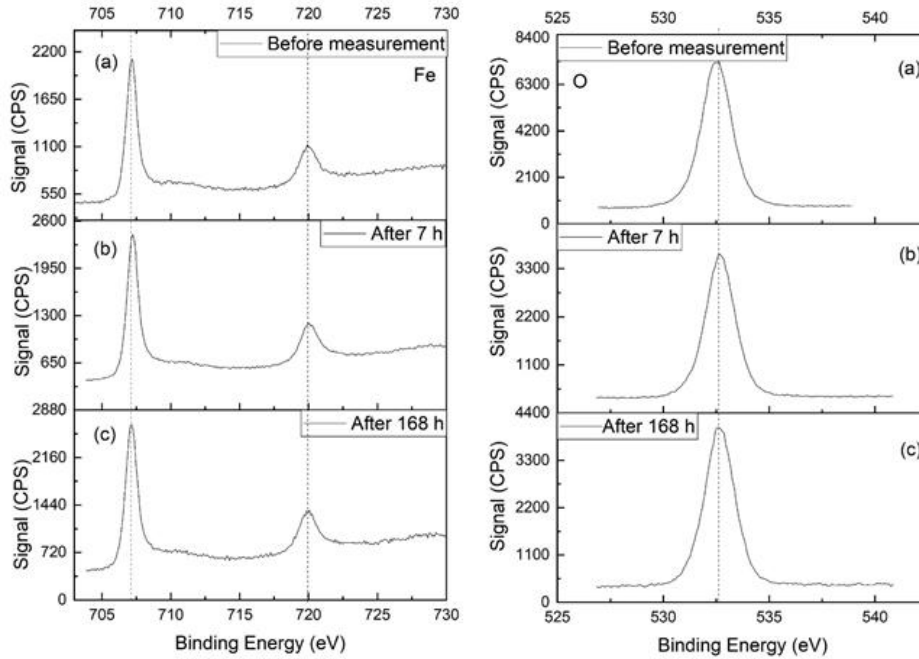


Figure 11.5 The surface electronic state of Fe (left) and O (right). (a) As-prepared β -FeSi₂ nanoparticle. (b) β -FeSi₂ nanoparticle after 7 h electric test of β -FeSi₂ nanoparticle. (c) β -FeSi₂ nanoparticle after 168 h electric test of β -FeSi₂ nanoparticle.

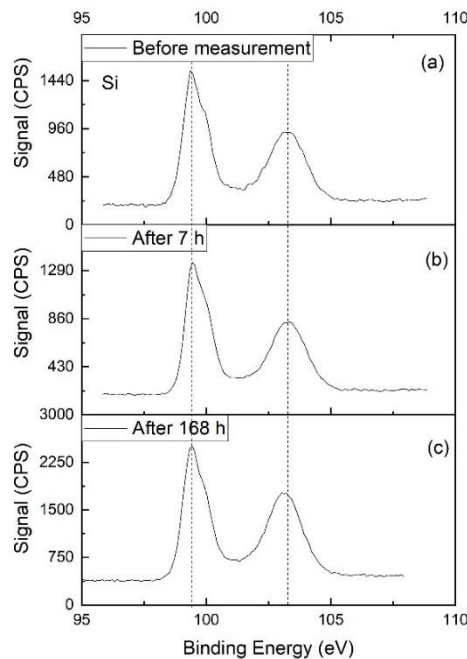


Figure 11.6 The surface electronic state of Si. (a) As-prepared β -FeSi₂ nanoparticle. (b) β -FeSi₂ nanoparticle after 7 h electric test of β -FeSi₂ nanoparticle. (c) β -FeSi₂ nanoparticle after 168 h electric test of β -FeSi₂ nanoparticle.

The result of the X-ray photoelectron spectra of Si in Figure 11.6 (Fe-Si bond/Si-O bond) element is slightly different. The peak at around 103.2 eV affiliates to SiO₂[185], the peak shifts from 103.28 eV to 103.13 eV, Peak shift above 0.2 eV is considered as chemical shift, while peak shift below 0.2 eV is regarded as physical shift or due to other reasons.

No obvious change is observed before and after charge and discharge reaction, showing that β -FeSi₂ nanoparticles are quite chemically stable, maintaining the micro capacitor's robust running in the longer term.

11.3 Oxygen sensing measurement of B-Si nanoparticles

With the same oxygen sensing set up in Section 0, different materials' produced oxygen concentration depended on applied voltage (Figure 11.7) are measured. Results show that β -FeSi₂ NPs have superior water-splitting ability than the B-Si NPs has. To achieve a produced oxygen flow of 100 ppm, a voltage of 3.5 V is needed to apply on the B-Si capacitor, higher than a voltage of 3.1 V of the β -FeSi₂ capacitor. This means at the same voltage, less current is consumed to split water with a B-Si capacitor.

In any case, there is a contract between the water molecule and gold layer since the particle layer is porous. To figure out Au's influence (Au can also split water) in the oxygen sensing experiment, further oxygen detection measurement on Au-covered quartz electrode is carried. The tested parallel plate capacitor is consists of two Au-coated quartz plate electrodes and a sheet of glass fiber. The voltage-dependent produced oxygen concentration is plotted in Figure 11.7. Figure 11.7 shows that the oxygen concentration at 3 V is only 1/11 of a β -FeSi₂ parallel-plate capacitor.

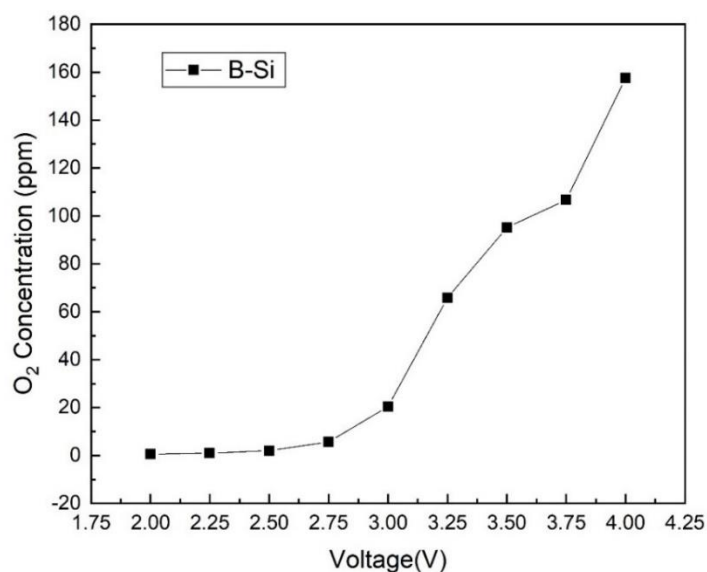


Figure 11.7 Oxygen concentration at a different applied voltage of B-Si capacitor

The resistance of the fully charged capacitor is calculated and plotted in Figure 6.47. It shows that the circuit resistance decreases sharply with voltage increasing. After 2 V, the resistance plot is much lower, which can be explained by water electrolysis that creates mobile ions. At low applied voltage, there is only self-ionization of water, and the conductivity of the whole capacitor is relatively low. As the applied voltage increases, water electrolysis starts and produces more mobile ions and electrons, increasing the overall capacitor's conductivity, which increases the rate performance of the capacitor.



12 Acknowledgment

I would like to acknowledge my supervisor Prof. Dr. Hartmut Wiggers, co-supervisor Prof. Dr. Axel Lorke for their kind and enthusiastic help, dedicated guidance on my Ph.D thesis. Sincere and many thanks for their tolerance of my immaturity. They put a lot of effort and attention into my work. I can't finish the work without their plentiful and substantive tutoring. Thanks to Dr. Hans Orthner, who trains me on nanoparticle synthesis and helps me a lot on detailed research problems, no matter how big or trivial. Thanks to Dr. Jens Theis for initiating the idea of applying the semi-conducting materials in the energy storage field, my work can't be carried out without his pioneer work. Sincere thanks to PD Dr. Martin Paul Geller, Dr. Günther Prinz, Dr. Nicolas Wöhrl, Mathias Bartsch, for their kind help and beneficial advice on my work, and my colleagues Dennis Oing who helps me a lot on LabView, Jens Kerski, who helps me on MATLAB, Pia Lochner, and Sebastian Tigges who helps me on other aspects, wish you all have a promising future in the field of science or industry.

Special thanks are given to Dr. Aswin Vijai Asaithambi, my dear colleague and friend, for his accompany during the whole Ph.D. period, for his heart-warming help on science and on my life. And my beloved friend Dr. Jin Wang, thanks for her support, love, and care for me, she helps me going through the most challenging time, also my dear friend Dr. Xiaoxiang Wu who encourages me to continue the work. Many thanks to my caring friend Ratana Chuenchom who takes care of me while she was in Germany.

I'm eternally grateful for the IMPRS-SurMat program (International Max Planck Research School for Interface Controlled Materials for Energy Conversion) for my Ph.D. funding. It is a great program that provides a broad vision of science. Thanks to Mrs. Elke Gattermann from SurMat, our secretary Mrs. Jennifer Stein and Mrs. Marion Hannemann, who help me a lot since the first day I arrived in Germany.

Final thanks and love are given to my parents, uncles, and whole family who support me financially and mentally. Thanks for their support and understanding. I love them forever.

DuEPublico

Duisburg-Essen Publications online

UNIVERSITÄT
DUISBURG
ESSEN

Offen im Denken

ub | universitäts
bibliothek

Diese Dissertation wird via DuEPublico, dem Dokumenten- und Publikationsserver der Universität Duisburg-Essen, zur Verfügung gestellt und liegt auch als Print-Version vor.

DOI: 10.17185/duepublico/74606

URN: urn:nbn:de:hbz:464-20210805-143141-7

Alle Rechte vorbehalten.